Simulation Study for the IceCube-Gen2 Surface Array

Simulationsstudie für den IceCube-Gen2 Oberflächen-Detektor

Master's Thesis in Physics
by

Mark Weyrauch

August 2021

KARLSRUHE INSTITUTE OF TECHNOLOGY (KIT)
INSTITUTE OF EXPERIMENTAL PARTICLE PHYSICS (ETP)

Reviewer:	Prof. Dr. Frank Schröder (Assist. Prof., University of Delaware, USA)
Second Reviewer:	Prof. Dr. Ralph Engel
Advisor:	Dr. Agnieszka Leszczyńska

I declare that I have developed and written the enclosed thesis completely by myself, and have not used sources or means without declaration in the text.

Karlsruhe, den 17.08.2021, _____

Mark Weyrauch

Als Ansichtsexemplar genehmigt von

Karlsruhe, den 17.08.2021, _____

Prof. Dr. Frank Schröder

Abstract

Simulation Study for the IceCube-Gen2 Surface Array

Due to their low flux, high-energy cosmic rays are measured indirectly via detection of the particle cascades (air showers) induced by the interaction of primary cosmic rays with the atmosphere. Information about the nature of the cosmic-ray particle is therefore convoluted in the characteristics of the footprint measured with ground based air-shower detector arrays. The development of the particle cascade is accompanied by emission of electromagnetic radiation, offering different channels for air-shower detection. In order to improve the accuracy in reconstruction of the physical parameters of the primary cosmic ray, the combination of multiple detection channels is highly beneficial.

IceCube is a cubic-kilometer neutrino observatory at the South Pole, comprised of a deep in-ice array and a surface array, IceTop. IceTop contains 162 ice-Cherenkov tanks distributed along the footprint of the in-ice array and is currently undergoing an enhancement by additional hybrid detector stations with scintillation detectors and radio antennas. The scintillation detectors will provide a low detection threshold, while the radio antennas enable the measurement of the atmospheric depth of the air-shower maximum, X_{max}, and therefore provide an improved sensitivity to the cosmic-ray mass.

IceCube-Gen2 is the planned extension of the IceCube Neutrino Observatory. Since IceTop has proven a valuable component of IceCube, providing measurements of the cosmic-ray energy spectrum and mass composition as well as a veto for the in-ice array, IceCube-Gen2 will feature a surface array, too. In the baseline design, the IceCube-Gen2 surface array is comprised of surface stations with scintillation detectors and radio antennas, similar to the ones foreseen for the IceTop enhancement, distributed over an area of ca. $\sim 8\,\mathrm{km}^2$. This hybrid air-shower array will extend the range of cosmic-ray measurements towards higher energies, while improving veto and multi-messenger capabilities. In order to quantify the science capabilities in more detail, a first simulation study of the IceCube-Gen2 scintillator array is performed within the scope of this thesis. It is shown, that the performance of the baseline design of the Gen2 surface array for air-shower detection and reconstruction is sufficient to match various science goals. In particular, the low detection threshold of below 500 TeV for both proton and iron primaries for zenith angles up to 27° is highly beneficial for the veto capabilities of the array. The geometrical air-shower parameters, i.e., the location of the shower core and the incident direction, can be reconstructed with accuracies of below 10 m and on a sub-degree level, respectively, for energies above ∼10 PeV. In the context of hybrid reconstructions with radio measurements, such an accurate geometrical reconstruction constitutes a valuable input. A preliminary study of the reconstruction of the cosmic ray energy results in a statistical precision of below 10% for vertical proton and iron primaries for energies approaching 100 PeV. The energy resolution in this energy region will be further enhanced by radio measurements. Overall, the IceCube-Gen2 surface array therefore enables high-quality measurements of the cosmic-ray energy spectrum in the range of the expected transition from Galactic to extra-galactic cosmic-rays. Using coincident

measurements of high energy muons with the in-ice array and the air showers producing these muons with the surface array, IceCube-Gen2 has great potential regarding determination of the cosmic-ray mass. This also enables unique studies of hadronic interactions. Due to the large surface area in combination with a large angular acceptance for such coincident events, the IceCube-Gen2 surface array further provides a significant increase in statistics compared to IceCube.

Zusammenfassung

Simulationsstudie für den IceCube-Gen2 Oberflächen-Detektor

Aufgrund der geringen Flussdichte hochenergetischer kosmischer Strahlung wird diese indirekt durch die Teilchenkaskade (Luftschauer), die durch Interaktion der primären kosmischen Strahlung mit der Atmosphäre induziert wird, detektiert. Informationen über die Eigenschaften der kosmischen Strahlung sind deshalb in den Charakteristiken des Fußabdrucks enthalten, der von bodengebundenen Luftschauer-Detektor-Arrays gemessen wird. Die Entwicklung der Teilchenkaskade wird durch Emission elektromagnetischer Strahlung begleitet, wodurch verschiedene Kanäle für Luftschauerdetektion zur Verfügung stehen. Um die Genauigkeit der Rekonstruktion der physikalischen Parameter der kosmischen Strahlung zu erhöhen, ist eine Kombination mehrerer Detektionskanäle von großem Vorteil.

IceCube ist ein Neutrino-Observatorium am Südpol, welches aus einem tiefen, kubikkilometer großen In-Eis-Detektor und einem Oberflächen-Detektor (IceTop) besteht. IceTop beinhaltet 162 ice-Cherenkov-Detektoren, die entlang des Fußabdrucks des In-Eis-Arrays positioniert sind und wird aktuell mit zusätzlichen Hybrid-Stationen aus Szintillations-Detektoren und Radioantennen erweitert. Die Szintillations-Detektoren bieten eine niedrige Detektions-Schwelle, während die Radioantennen eine Messung der atmosphärischen Tiefe des Luftschauermaximums X_{max} ermöglichen und damit eine erhöhte Sensitivität für die Masse der Primärteilchen der kosmischen Strahlung bereitstellen.

IceCube-Gen2 ist die geplante Erweiterung des IceCube-Neutrino-Observatoriums. Da sich IceTop sowohl als Veto für den In-Eis-Detektor als auch durch Messungen des Energiespektrums der kosmischen Strahlung und deren Massenzusammensetzung als wertvolle Komponente von IceCube erwiesen hat, wird IceCube-Gen2 ebenfalls einen Oberflächen-Detektor enthalten. Im Baseline-Design ist der IceCube-Gen2 Oberflächen-Detektor aus Oberflächenstationen mit Szintillations-Detektoren und Radioantennen aufgebaut, die identisch zur Erweiterung von IceTop und über eine Fläche von ungefähr $8\,\mathrm{km}^2$ verteilt sind. Dieser hybride Luftschauer-Detektor wird den Messbereich für kosmische Strahlung auf höhere Energien erweitern und Veto- sowie Multi-Messenger-Fähigkeiten verbessern. Um das wissenschaftliche Potential genauer zu quantifizieren, wird innerhalb dieser Arbeit eine erste Simulationsstudie für das IceCube-Gen2 Szintillator-Messfeld durchgeführt. Es wird gezeigt, dass die Leistung des Baseline-Designs des Gen2 Oberflächen-Detektors im Bezug auf Luftschauerdetektion und -Rekonstruktion ausreichend ist, um diversen wissenschaftlichen Zielen gerecht zu werden. Insbesondere die niedrige Detektionsschwelle von unter 500 TeV für Protonen und Eisenkerne als primäre Teilchen mit Zenithwinkeln bis zu 27° ist von großer Bedeutung für die Veto-Fähigkeiten des Arrays. Die geometrischen Luftschauer-Parameter, d.h. die Position des Auftreffpunkts des Schauers am Boden und die Einfallsrichtung, können für Energien oberhalb von $\sim$10 PeV mit einer Genauigkeit von weniger als 10 m bzw. von weniger als 1° rekonstruiert werden. Eine solch gute geometrische Rekonstruktion stellt einen wertvollen Beitrag für Hybrid-Rekonstruktionen mit Radiomessungen dar. Eine einleitende Studie zur Rekonstruktion der Energie der kosmischen Strahlung

für Energien nahe 100 PeV resultiert in einer statistischen Präzision von unter 10% für vertikale Protonen und Eisenkerne als primäre Teilchen. In diesem Energiebereich wird die Auflösung der Energierekonstruktion durch Radiomessungen weiter verbessert. Insgesamt ermöglicht der IceCube-Gen2 Oberflächen-Detektor somit eine qualitativ hochwertige Messung des Energiespektrums der kosmischen Strahlung im Bereich des erwarteten Übergangs von galaktischer zu extragalaktischer kosmischer Strahlung. Durch eine Kombination mit koinzidenten Messungen der in Luftschauern produzierten hochenergetischen Myonen mit dem In-Eis-Detektor, besitzt IceCube-Gen2 ein großes Potential bezüglich der Bestimmung der Masse der kosmischen Strahlung und ermöglicht Studien hadronischer Wechselwirkungen. Aufgrund der großen Fläche in Kombination mit der großen Winkel-Akzeptanz für koinzidente Messungen, bietet der IceCube-Gen2 Oberfächen-Detektor zusätzlich eine signifikante Erhöhung der Messstatistik im Vergleich zu IceCube.

Contents

Chapter 1.

Introduction

More than one hundred years ago Victor Hess discovered the phenomenon of cosmic rays penetrating the atmosphere by observation of a significant increase in radiation intensity high in the atmosphere [1]. Since this increase could not be explained by nuclear radiation, Hess concluded these charged particles to be of extraterrestrial origin. Since then, cosmic rays have been studied over 11 orders of magnitude in energy by direct and indirect measurements. However, until today many open questions about origin, propagation, and nature of the acceleration of cosmic rays remain.
The measurement of cosmic rays in the high energy region generally is a difficult task, as the particle flux rapidly decreases with increasing energy. Thus, direct detection methods via balloon or satellite measurements become unfeasible. Instead, cosmic rays above a few 100 TeV are measured with ground based experiments by observation of the particle cascades resulting from the interaction of the cosmic ray with the atmosphere. However, in order to achieve a sufficient statistical precision in air-shower measurements as well as to account for the large air shower footprint, the size of such detector arrays has to be scaled accordingly.

In general, cosmic-ray air showers are accessible via detection of the cascade particles or by measurement of the radiation produced during the cascade development through the atmosphere. Each channel has unique advantages with regard to the reconstruction of underlying physical properties. Hence, in order to derive physical parameters with improved accuracy, cosmic-ray air shower detectors can utilize hybrid measurements with complementary detection channels.

The surface array of the next generation extension of the IceCube neutrino observatory, IceCube-Gen2, foresees a hybrid array comprised of stations with scintillation detectors for particle detection and radio antennas for the measurement of radio emission produced by the propagation of charged air-shower particles within the atmosphere. While scintillators provide a low detection threshold, the radio array allows for an improved determination of the cosmic-ray mass [2].
The choice of scintillation detectors in combination with radio antennas is based on the experience gained during the development of the enhancement of IceTop with similar detector stations [3]. IceTop is an array of ice-Cherenkov tanks and constitutes the surface array of IceCube. The IceTop enhancement will be the first step towards the eight times larger surface array of IceCube-Gen2, and will allow for studies for the planned next generation surface array [4].
A unique advantage of IceCube and IceCube-Gen2 is the combination of a surface and deep in-ice array, which enables coincident measurements of high energy muons produced in air shower events. This information, combined with a high-quality air shower measurement via scintillators and radio antennas as well as, for a part of the events, ice-Cherenkov detectors, is highly valuable for the determination of the cosmic ray mass and for studies of hadronic interaction models [2]. Due to the large acceptance for such coincident events, the detector arrangement of

IceCube-Gen2 will allow for improved precision in measurements of cosmic rays of Galactic and extra-galactic origin.

Within the scope of this thesis the science capabilities of the baseline design of the IceCube-Gen2 surface array are quantified in more detail. For this purpose, a first simulation study of the scintillator array of IceCube-Gen2 was performed.
For a better understanding of air-shower measurements, an overview of the underlying physics is presented in chapter 2. Further, IceCube and IceCube-Gen2 along with the according surface components are introduced in chapter 3. In chapter 4, the simulation chain used for the scintillator array simulations is discussed. A simulation framework was already developed for the scintillator array of the IceTop enhancement and is utilized for the studies of the IceCube-Gen2 scintillator array.

Different layouts of the scintillator detector array for IceCube-Gen2 were considered and according simulation sets were generated analyzed. Moreover, parametrizations of the spatial and temporal distributions of the array response were derived. These parametrizations are further utilized in chapter 5. In this chapter, the performance of the IceCube-Gen2 scintillator array regarding reconstruction of cosmic ray characteristics is investigated. The scintillator array reconstruction developed for the IceTop-enhancement array [5] was optimized for IceCube-Gen2 and the overall performance in the context of science requirements is discussed. In chapter 6, a preliminary study on the potential of cosmic-ray mass discrimination with the IceCube-Gen2 scintillator array was performed, including studies on coincident measurement capabilities. Lastly, the analyses are summarized in chapter 7 and an outlook to possible future studies is given.

Chapter 2.

Cosmic rays

2.1. Sources and propagation

Cosmic-ray particles have been measured with energies up to $\mathcal{O}(100\,\mathrm{EeV})$. Although different source candidates possibly providing such an extreme acceleration have been proposed, the exact nature of the sources remains uncertain. In general, different sources are separated into local sources within our Galaxy, hence, Galactic sources, and extragalactic sources. In 1949, Fermi suggested a model of cosmic-ray acceleration due to elastic reflection by a moving interstellar magnetic field structure [6]. This process, however, was found to be a second order effect as the average energy gain is proportional to $(v/c)^2$, with the speed of light c and the velocity of the moving structure v [7], and is therefore referred to as second order Fermi acceleration. A more efficient acceleration is provided by the, later found, first order Fermi process, which is based on the Fermi acceleration in the vicinity of shock fronts. As a particle crossing a shock front in either direction can be reflected by the moving magnetic field structure and thus gain energy, the average energy gain is directly proportional to v/c. Particles can therefore be accelerated to high energies via multiple back-and-forth reflection at the shock front. It is important to mention, however, that this method relies on the in-homogeneity of the magnetic field in the vicinity of the shock front, since particles could escape the acceleration region more easily along homogeneous field lines [7]. The escape probability in fact limits the maximum acceleration energy via the *Hillas criterion* $E_{\mathrm{max}} = qBL$ [8], where q denotes the charge of a particle and B, L the magnetic field and the size of the shock front, respectively. From this geometrical requirement therefore a particle-mass dependent maximum energy for a particular source arises naturally.

A popular source candidate for Galactic cosmic rays is the shock front acceleration in supernova remnants (SNRs) [9]. The shock front produced in a supernova explosion can expand at velocities of one tenth of the speed of light for $\mathcal{O}(100\,\mathrm{y})$ [10], providing acceleration up to PeV energies for protons [11]. Also gamma ray bursts (GRBs), can accelerate cosmic ray particles. Among others, GRBs can be created in the core-collapse of an extremely massive star, a so-called hypernovae, and in neutron star mergers [12]. GRBs manifest two relativistic jets, one for each magnetic pole, emitting high-energy gamma rays which are believed to be primarily produced by synchroton radiation of electrons [13]. The shock fronts in such jets could also provide powerful acceleration for hadronic particles up to $\sim 100\,\mathrm{EeV}$ [14]. At such energies cosmic ray particles can escape the Galactic magnetic field and are therefore likely of extragalactic origin. Another possible source of cosmic rays of the highest energies are active galactic nuclei (AGNs). The center of an AGN contains a supermassive black hole, featuring two jets induced by mass accretion of surrounding matter [15]. Similar to GRBs these jets could accelerate cosmic rays to the highest observed

energies.

In addition to processes in the source environment, also propagation effects shape the cosmic-ray energy spectrum observed at Earth. Charged particles on their way through the Galaxy are deflected by the Galactic magnetic field and can undergo a variety of different processes. The latter includes interactions like scattering and ionization processes, causing an energy loss of the primary cosmic ray particle. In addition, particle decays and spallation can cause a change in the cosmic-ray mass composition [16]. The deflection of cosmic ray particles by the Galactic magnetic field leads to a diffusive propagation washing out any initial direction information. However, this process depends on the particle energy and charge. Hence, the Galactic magnetic field constitutes a mass dependent confinement for cosmic rays. Cosmic ray particles with sufficient energy to escape the magnetic confinement are further influenced by extragalactic magnetic fields. Overall, the propagation effects lead to an additional mass dependent steepening of the cosmic-ray spectrum. Thus, in order to correctly account for these effects in the interpretation of the cosmic-ray energy spectrum detailed models of the Galactic and extragalactic magnetic fields are crucial [9].
An important tool for the identification and study of cosmic ray sources are multi-messenger observations. In contrast to charged cosmic ray particles, gamma rays and neutrinos[1] emitted by the sources can be used to trace back the source locations as their propagation is not influenced by magnetic fields. In the case of gamma rays, however, the observation horizon is limited by interactions with the intergalactic medium [5]. Due to their extremely small cross section, neutrinos, in principle, constitute ideal messenger particles. However, this characteristic also leads to a challenge for neutrino measurements. This challenge can be addressed with a neutrino detector of sufficient dimension, such as the IceCube Neutrino Observatory. Thus, multi-messenger astronomy in combination with mass dependent measurements of the cosmic-ray energy spectrum represent an important tool to answer the open questions regarding the origin of cosmic rays.

2.2. Energy spectrum

Charged primary cosmic ray particles (cosmic ray primaries) arriving at earth primarily consist of nuclei (98%) and a small fraction of electrons (2%) [17]. The main fraction of the nuclei is constituted by protons with around 90%, the remaining part is build up by helium (9%) and heavier nuclei [18]. These fractions apply to a certain magnetic rigidity $R = pc/|e|z$ with the momentum p and particle charge $|e|z$, describing the resistance of a particle to be deflected by a magnetic field and thus the probability to penetrate through Earth's geomagnetic field [17, 19]. In fact, the fractions of cosmic ray primaries depend on the considered energy range. Generally, cosmic ray energies are distributed over 11 orders of magnitude, starting at around $10^9\,\mathrm{eV}$ ($\mathcal{O}(\mathrm{GeV})$) with particles originating mainly from solar eruptions and reaching energies up to multiple $10^{20}\,\mathrm{eV}$ ($\mathcal{O}(100\,\mathrm{EeV})$) emerging from extragalactic acceleration processes [20]. The according spectrum has been measured by many experiments over different energy ranges [22], showing a steeply falling behavior above a few GeV which can be described by a power-law function:

$$\frac{dI}{dE} \approx I_0 \left(\frac{E}{E_0}\right)^{-\gamma}, \tag{2.1}$$

[1] Both particles can accompany hadronic processes in cosmic ray sources

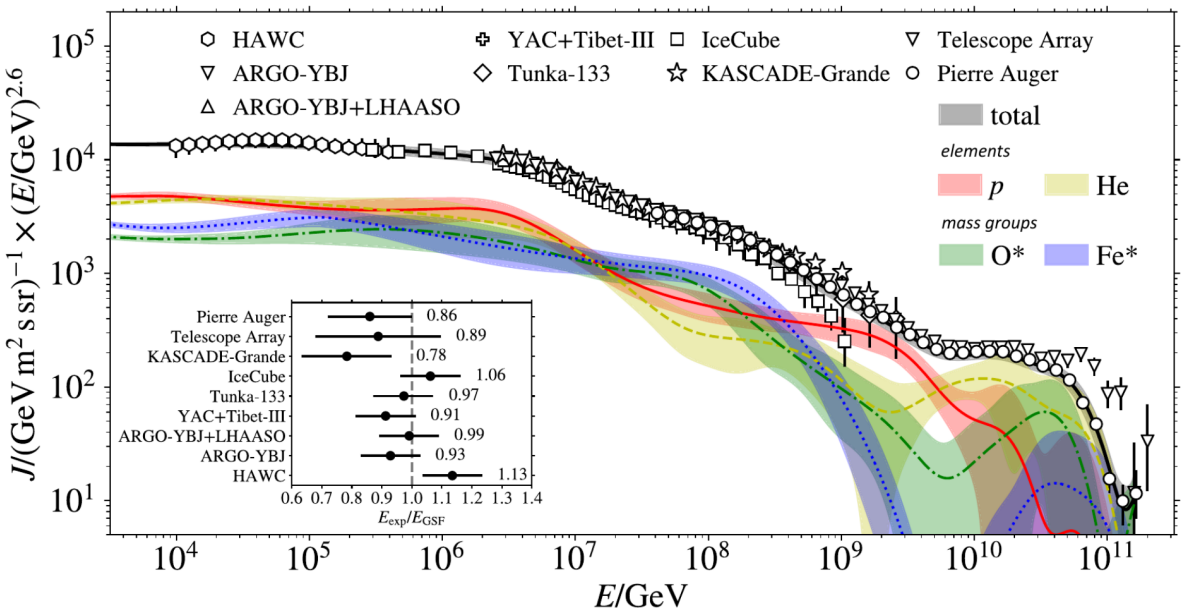

Figure 2.1.: All-particle cosmic-ray energy spectrum measured by different experiments. The combined fit of energy spectrum and mass composition obtained via Global Spline Fit method (more details can be found in [21]) is shown with the solid black line. The mass dependent contributions to the flux are shown with colored lines. The according bands illustrate the one-sigma interval. A constant energy shift applied for the different experiments (shown in the bottom left corner) approximately accounts for the different energy scales. Plot taken from [9].

where I_0 is the differential flux[2] at energy E_0. The spectrum for low, high and ultra-high energy cosmic rays (LECR, HECR and UHECR, respectively) is shown in Fig. 2.1. By multiplication with an energy dependent factor (in this case $(E/\mathrm{GeV})^{2.6}$) the 3 main features can be visualized more clearly. Each of these distinctive features is accompanied by a change of the spectral index (see Fig. 2.1).

Above several GeV up to a few 100 TeV[3] the spectral index γ is 2.7 [24]. At around 3 PeV the knee describes an increase of the spectral index.The spectrum is further steepening at $\sim$ 100 PeV, known as the second knee [21]. Measurements from the Pierre Auger Observatory indicate that this change extends to at least $\sim$ 200 PeV [25]. For even higher energies of around 8 EeV a flattening back to $\gamma \sim 2.7$ characterizes the third main feature of the energy spectrum, the ankle [21]. At slightly higher energies, the Pierre Auger Observatory recently discovered an additional feature, a spectral break just above 10 EeV, which can be explained by an energy dependent mass injection at cosmic ray sources in combination with propagation effects [26, 27].

The knee as well as the second knee can be explained by Galactic sources reaching their acceleration limits. In combination with the finite confinement[4] elicited by the Galactic magnetic field, this leads to a rigidity dependent drop[5] and therefore a softening of the spectrum [29]. This effect is also referred to as Peters cycle [30].

Consequently, in this scenario the knee and second knee represent the drop in the light and heavy component of the primary cosmic rays, respectively. Indeed, these light and heavy knees

[2] $I_0 = 1.8 \cdot 10^4\,(\mathrm{m^2\,s\,sr\,GeV})^{-1}$ for $E_0 = 1\,\mathrm{GeV}$ [23]

[3] For even higher energies direct detection methods are not feasible anymore, as the cosmic ray flux becomes too small

[4] At sufficient energies the gyro-radius of primary cosmic rays becomes larger than the size of the galaxy, allowing for particles escaping the galactic magnetic field

[5] Spectral break for a given rigidity but different energy for different elements [28]

have been observed by the KASCADE-Grande experiment [31]. Measurements of the Pierre Auger Observatory are also consistent with the Peters cycle [21].
However, there are alternative explanations for the softening, e.g., by assuming a transition between two different source populations [32]. In this context, Hillas proposed an additional higher energy component ('component B') of the Galactic cosmic rays [33], resulting in a three component model of the transition between Galactic to extragalactic cosmic rays (transition region) [34]. In this model the ankle marks the transition energy. However, many scenarios propose the existence of further components for both Galactic and extragalactic cosmic rays [35, 36, 37, 38].
Different models describing the transition region differ in transition energy and mass composition. Shifting the transition towards lower energies eventually leads to problems due to the smaller magnetic horizon of cosmic ray particles of lower energy [39]. Generally, a transition energy below the ankle relies on an alternative explanation of the ankle feature. The dip model, based on the energy loss of extragalactic protons through pair-production by interaction with the cosmic microwave background (CMB), was already excluded [40] by measurements of a mixed composition in the ankle region[6]. However, this model neglects the contribution of heavier nuclei, which also suffer energy loss during the propagation [41]. An alternative explanation could be based on interaction processes of cosmic rays at their sources [42].
A recent analysis of the Pierre Auger data results in a good description of the ankle region with a mixed composition with dominant contribution of intermediate mass groups [43]. Such behavior could be connected to photo-disintegration processes in the source region [41]. Thus, since propagation effects additionally influence the relative abundances of different cosmic ray particles [5], a more detailed measurement of the mass dependent energy spectrum is crucial in order to draw conclusions about the origin of the spectral features.

For energies beyond the ankle, the Galactic magnetic field is unable to trap cosmic ray particles. Hence, the origin of cosmic ray particles in the highest observed energy region is believed to be extragalactic [44]. At energies of around 50 EeV a suppression of the cosmic ray flux is observed [45]. At these energies, the GZK cut-off is discussed. This effect predicts the energy loss of protons by interaction with CMB photons when exceeding sufficient energies [46, 47]. The interaction takes place via excitation of the Δ-resonance

$$\gamma + p \rightarrow \Delta^{+} \rightarrow p/n + \pi^{0}/\pi^{+}, \tag{2.2}$$

which then produces pions (photo-pion production). This theoretically restricts the maximum distance from a source of cosmic protons to Earth to < 150 Mpc [46]. For heavier nuclei, the interaction with a CMB photon mainly leads to photo-disintegration [48], causing similar energy loss [49]. Current experimental data in the energy region of the GZK suppression can be modeled most accurately with mixed composition assumptions [9]. In particular, measurements from the Pierre Auger Observatory [50, 26] favor a mixed composition model with heavier elements than He [9] at around the ankle and a charge dependent maximum energy [49]. Due to statistical uncertainties, data from the Telescope Array (TA) can not yet exclude pure light mixes [9].
However, an energetic exhaustion of cosmic accelerators could cause a similar drop in the cosmic ray spectrum. In this case, a similar behavior as in the knee region is expected, namely a successive cut-off of the different components [49]. Hence, again, more detailed information about the mass composition is crucial in order to draw conclusions about the origin of the spectral features.

[6] The assumption of a pure proton composition in this model would result in a proton dominated composition in the ankle region [32]

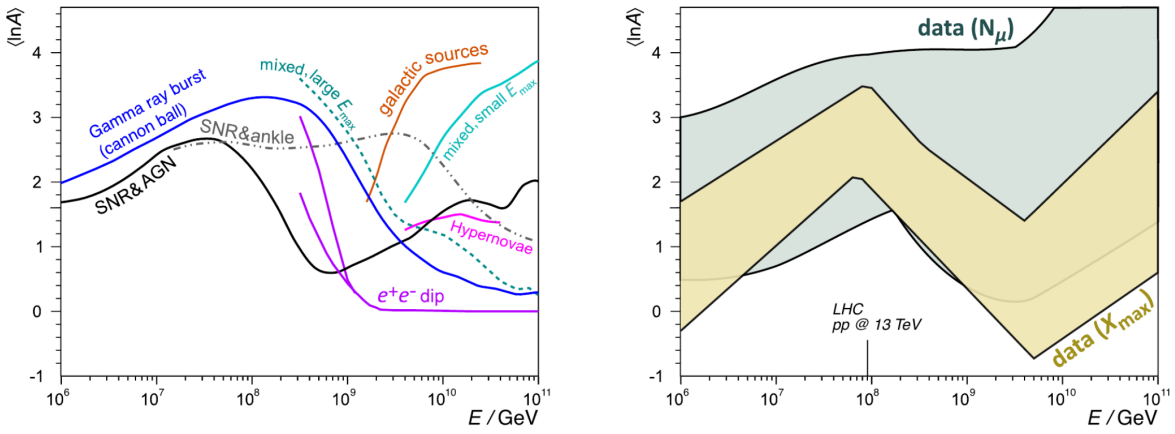

Figure 2.2.: Left: Comparison of cosmic-ray mean-logarithmic mass predicted from different models. Right: The two bands indicate the ranges covered by various experiments along with the respective parameter used for the mass-separation. The main contribution to the uncertainty indicated as width of the bands is caused by the theoretical uncertainties in hadronic interaction models used in air shower simulations. Plot taken from [51].

Mass composition

Due to the applicability of direct measurements below 100 TeV primary energy the mass composition in this region can be determined with smaller systematic uncertainties. For higher energies, the indirect nature of cosmic ray measurements constitutes a challenge, as the primary characteristics have to be de-convoluted from the air shower observations. The two main channels of primary mass determination with cosmic-ray air shower measurements are the depth of the shower maximum, $X_{\max}$, and the relative contributions of muon number[7] N_μ and electromagnetic shower-component [9] (see section 2.3 for more details). The general evolution of the mass composition for primary energies in and beyond the transition region is presented in Fig. 2.2. At the second knee the composition becomes heavier and is lightest around the ankle. A more accurate measurement of the mean-logarithmic mass could be used to discriminate between different cosmic-ray source classes (the according model predictions are shown in Fig. 2.2 (left)) [51]. Currently, however, mainly the simulation models, used in combination with air shower measurements in order infer the primary mass, constitute a large uncertainty. In this context the main contribution to the uncertainty comes from the models describing hadronic interactions in the shower development. Since the observed energies are much larger than the maximum energies reached at colliders (the maximum center-of-mass (COM) energy for proton-proton collisions accessible at the LHC is shown with a vertical line in Fig. 2.2 (right)) the description of hadronic interactions in air showers has to be extrapolated, resulting in larger uncertainties with increasing energy. Hence, a reduction of systematic uncertainties introduced by such hadronic interaction models as well as more precise measurements are crucial in order to draw conclusions about the sources of cosmic rays. The latter can be achieved via hybrid air shower measurements, i.e. by utilizing different detection channels. Additionally, measurements of collisions in the forward direction with heavier nuclei via particle accelerator experiments could improve the hadronic interaction models [9].

In fact, throughout different hadronic interaction models a consistent mismatch in the predicted

[7] Derived by integration of the measured lateral muon density [51]

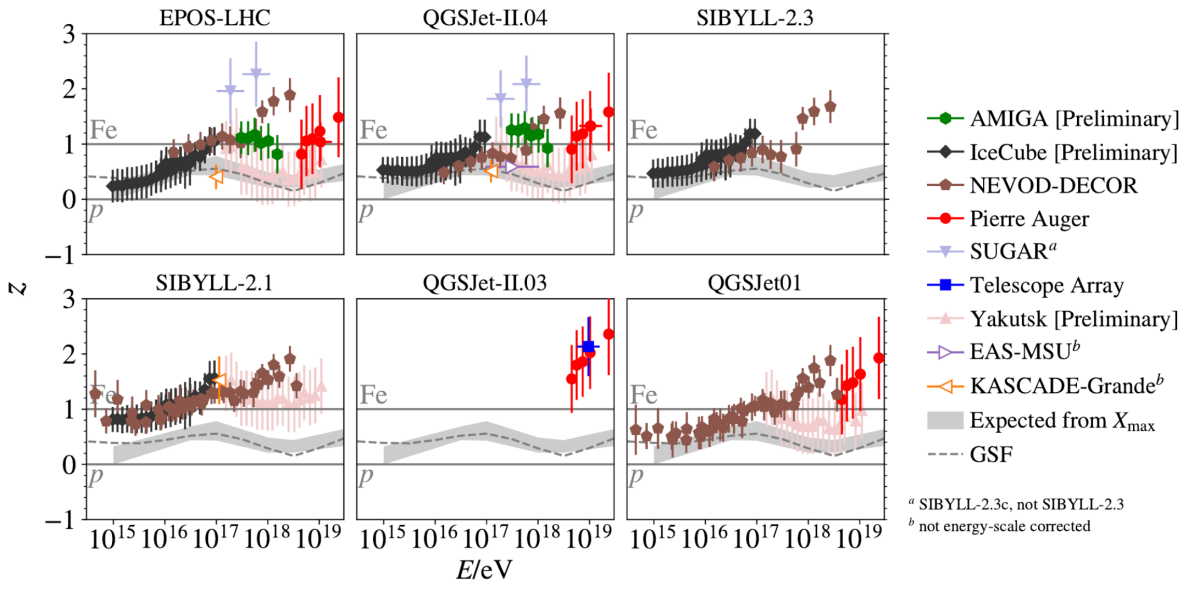

Figure 2.3.: Comparison of muon density measurements from different experiments based on various hadronic interaction models. Upper and lower plots show the data before and after energy cross calibration via GSF fit, respectively. Plot taken from [52].

number of muons produced in air showers can be observed when comparing to the measurements [51] (see Fig. 2.3). This instance is called the *muon puzzle*, since the origin of this discrepancy is still unknown. The mismatch in the muon number becomes significant at energies around the second knee [9], however, already starts growing above the knee [51]. Hence, the discrepancy is already observed for showers with COM energies (at the nucleon level) of the first interaction comparable to collider energies [51], accelerator experiments could be used to investigate possible sources for the muon mismatch. However, such experiments are mostly focused on a different phase-space for the discovery of heavy new particles. More precise investigations of hadronic collisions for large pseudorapidities via dedicated accelerator experiments, such as LHCf [53], is important for further progress. Additionally, cosmic-ray air shower measurements can be utilized to study hadronic interaction models. In particular, a complementary measurement of N_μ and $X_{\max}$ is an important tool for model tests as both parameters are sensitive to the primary mass and should therefore yield a similar mass composition [51].
The IceCube Neutrino Observatory offers the unique opportunity of a simultaneous measurement of the air shower with a surface array and the corresponding high-energy muon bundle with a deep in-ice array [51]. In combination with information about the low-energy muon content at the surface, this allows for insights into the first hadronic interaction [51] of the shower as well as the development of the corresponding hadronic cascade. Overall, more detailed knowledge about the hadronic interactions in air showers is crucial for a better understanding of the features of the cosmic-ray energy spectrum.

Anisotropy

An important complementary study to mass composition measurements are anisotropy searches [51], as they can provide a better understanding of Galactic and extragalactic cosmic-ray sources as well as propagation effects. In general, the arrival directions of Galactic cosmic rays are dis-

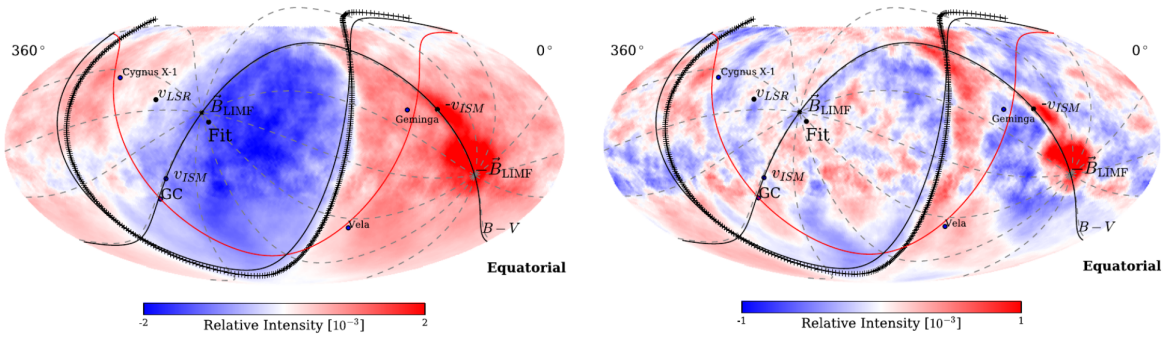

Figure 2.4.: Anisotropy of cosmic rays at 10 TeV before (left) and after (right) subtraction of the large-scale multipole fit. The red line marks the Galactic plane. Both magnetic equator and B-V plane (local interstellar magnetic field (LIMF) and velocity) are shown as black lines [54]. Plot taken from [9].

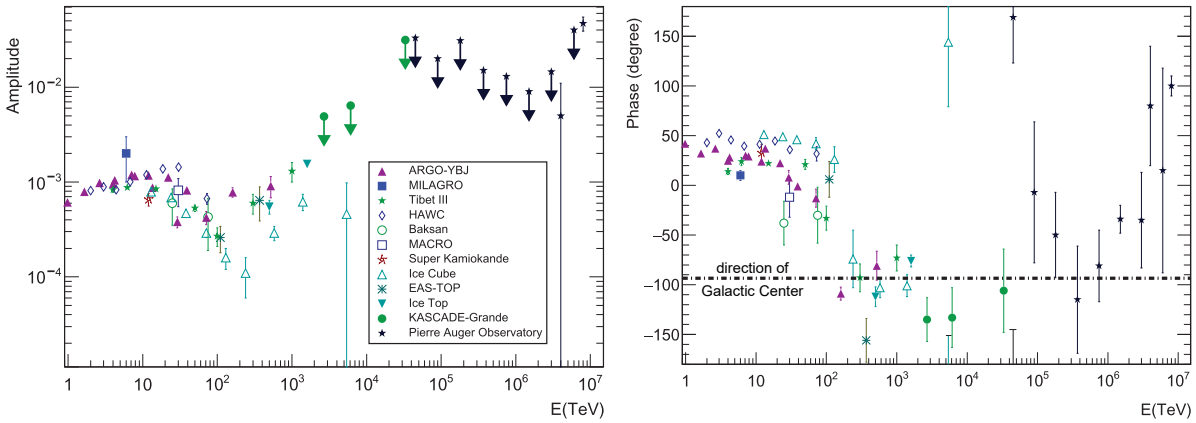

Figure 2.5.: First harmonic amplitude (left) and phase (right) of the large-scale anisotropy measured by different experiments. Plot taken from [55].

tributed isotropically, as the Galactic magnetic field washes out any initial direction information [5]. Nonetheless, weak cosmic ray anisotropies ($< 10^{-3}$ [9]) can be observed. The anisotropies for median primary energies of 10 TeV [54] are shown in Fig. 2.4. This nearly full-sky analysis was derived by collaboration of the IceCube Neutrino Observatory and the High-Altitude Water Cherenkov (HAWC) Observatory, providing a partial coverage of the southern and northern hemispheres, respectively [54]. On large scales a significant dipole anisotropy is observed, which can be related to the rotation of the solar system within our Galaxy. Conclusions based on the weak small scale anisotropies can not yet be drawn as both, more accurate measurements and a better understanding of the propagation effects, are required [9, 5].
Experimental evidence for the origin of the spectral features can be provided by the evolution of the amplitude and phase of the anisotropy with primary energy (see Fig. 2.5). In particular, the phase flips at energies of ~ 100 TeV and a few EeV could be related to contributions of different source types and the transition of Galactic to extragalactic sources, respectively [55]. The latter can additionally be connected to an according feature in the dipole amplitude at around EeV energies [56]. However, more accurate measurements are required in order to distinguish between different models for the transition region [55]. Below the EeV region the dipole phase seems to be consistent with the Galactic center [57]. This could be a hint for a transition energy around $\sim$1 EeV. However, again, more accurate measurements are required for further conclu-

sions. Since also the mass composition constitutes a main observable for the interpretation of the spectral features, mass dependent anisotropy studies would bring more detailed insights into cosmic ray sources. Additionally, complementary measurements of gamma rays and neutrinos as messenger particles can provide valuable information about cosmic ray accelerators, as these particles can accompany hadronic processes and are therefore most likely emitted by the same sources. In fact, LHAASO recently measured the first PeV gamma rays from Galactic sources [58]. This is an important step towards identifying the origin of Galactic cosmic rays. However, the exact nature of the sources remains unknown.
In addition to revealing sources via gamma ray and neutrino detection the according diffuse flux holds valuable information about the cosmic ray propagation [55]. However, in order to understand the background for the measurement of such messenger particles it is important to gain more detailed knowledge about the cosmic ray spectrum [55]. Hence, an increased accuracy of cosmic ray measurements, e.g. via hybrid detection, should go hand in hand with improvements in multi-messenger astronomy.

2.3. Extensive air showers

A high energy cosmic ray primary produces a large particle cascade in successive collisions with nuclei of earth's atmosphere. In this context, earth's atmosphere acts as a calorimeter, fragmenting the primary energy into secondary particles [59].
The first interaction primarily results in a large amount of pions as well as kaons, neutron, protons and other hadrons [60]. These secondary hadrons already carry transverse momenta due to the initial collision [61]. The neutral pions predominantly decay into two photons, initiating the electromagnetic air shower component. This component further grows via bremsstrahlung and pair production, leading to a large photon-electron cascade [61]. Once the electromagnetic shower reaches a critical energy[8], below which the energy loss due to ionization dominates, the electromagnetic shower dies out. Whether an air shower reaches the ground before or after the shower maximum is reached depends on the height of the first interaction and the energy of the primary cosmic ray. For low energy primaries the air shower can die out completely before it reaches ground level. Hence, an air shower detector benefits from a high altitude, as the energy threshold is reduced. Since, during the development of the electromagnetic shower, the particles are subject to scattering processes, the cascade further spreads out laterally.
On the other hand, high energy charged pions can further interact, leading mostly to additional production of charged and neutral pions [60]. Combined with interactions of the remaining hadrons from the first interaction this hadronic air shower component starts to grow. Once the energy of the individual hadrons is low enough, decays become more probable then further interactions. The charged pions mostly decay into muons, which can further decay into electrons[9]. The accompanying neutrinos of these decays build the neutrino component of an air shower, which can practically be treated as missing energy for the air shower detection. However, for the IceCube/IceCube-Gen2 detector, such neutrinos constitute a major background source for the search of astrophysical neutrinos, as further discussed in chapter 3.
The hadronic decays feed the electromagnetic and muonic shower components. The latter can be split into two fractions, namely conventional and prompt muons. The conventional muon production channel takes place mostly via decay of charged pions and kaons. For high energies,

[8] The critical energy E_c can be used to infer the height of the shower maximum via $X_{max} = \lambda \log_2(E_0/E_c)$, with the interaction length λ and the primary energy E_0 [62]

[9] Muons above roughly GeV energies do not decay before reaching the ground as the decay time becomes too large [17]

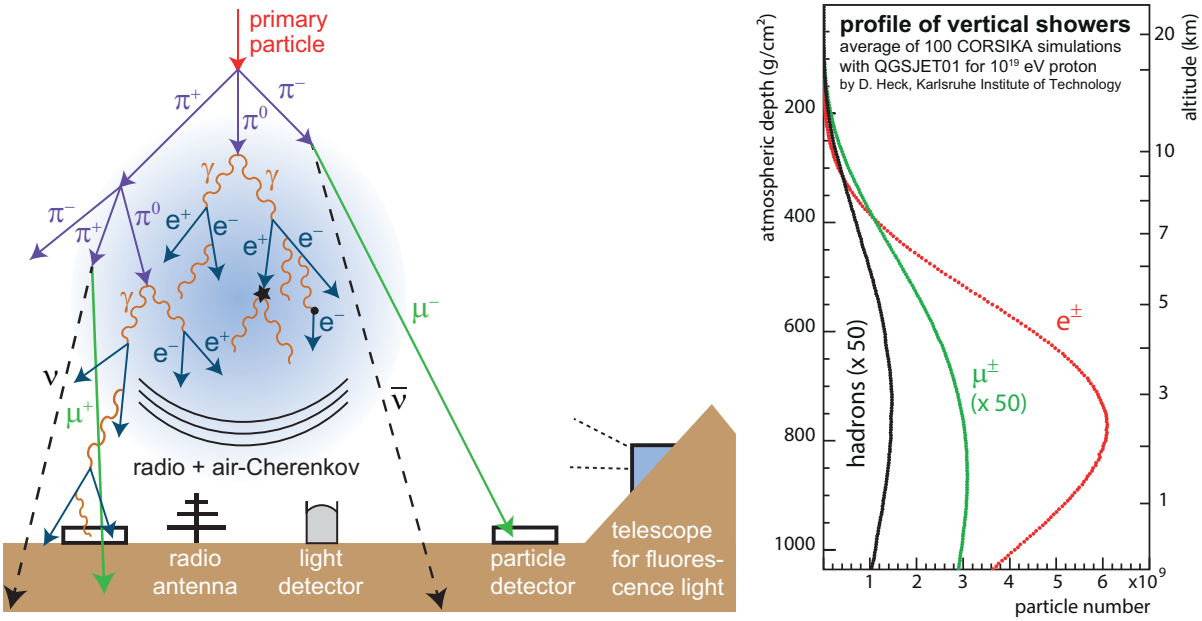

Figure 2.6.: Left: Schematic plot of an air shower and the different detection channels. Right: Longitudinal development of different shower components. Plot taken from [64]

small contributions due to decays of hadrons with heavier quarks, predominantly charmed particles, become more important [63]. Due to the small lifetimes of the according hadrons, muons from such decays are called *prompt muons*.

Overall, the air shower, comprised of electromagnetic, hadronic and muonic component, develops longitudinally along the direction of the incoming primary cosmic ray particle (see Fig. 2.6). Additionally, mainly due to Coulomb scattering, the shower features a lateral particle spread. Due to the much larger scattering cross section for electromagnetic particles, the average lateral spread is largest for the electromagnetic component. However, also low energy muons are subject to Coulomb scattering processes, resulting in a significant lateral spread [61]. The shower core is mostly build up by the hadronic part.

The interaction cross section for cosmic ray primaries of different mass is roughly proportional to the nucleon number. Hence, heavier nuclei will in average interact earlier in the atmosphere. Taking into account air shower universality [65], this translates to a mass dependency of the height of the shower maximum, X_{max}, measured in g/cm^2. Due to the fact that the shower maximum is additionally related to the primary energy, X_{max} constitutes one of the key parameters to infer the primary characteristics.
Air showers induced by primaries of different mass can be understood via superposition model, approximating air showers as superposition of A sub-showers with E/A energy, where A denotes the primary mass [60, 66]. Hence, for given primary energy, heavy nuclei produce more pions with lower energy than light nuclei, resulting in a high muon multiplicity. Both X_{max} and electron/muon ratio can therefore be used to infer the primary mass. The hybrid instrumentation of the IceCube-Gen2 surface array, with its scintillation detectors and radio antennas in combination with the ice-Cherenkov tanks of IceTop, allows for a sensitivity to both X_{max} and the electron/muon ratio. In particular, the additional possibility to measure the accompanying high-energy air shower muons with an optical in-ice detector below the surface instrumentation enables high-quality mass discrimination as well as studies of hadronic interactions

2.4. Detection techniques

In the context of earth's atmosphere as a calorimeter the shower development can be seen as energy deposit of the primary particle manifesting in cascades of different particles. Part of the energy deposit is the emission of electromagnetic radiation through accompanying effects caused by propagation of the electromagnetic component. This results in several possible detection channels for cosmic ray air-shower experiments.

Particle detection

A common method of air-shower detection is the measurement of the secondary particle distribution at ground level. Hence, the particle distribution is observed as a projection of the shower into the 2D plane given by a detector array [61]. The temporal and spatial characteristics of the distribution contain valuable information about the primary characteristics, such as direction and energy, as discussed in more detail in section 4.3.
The detection itself can be realized with typical particle detectors. Most commonly used are scintillation and water (or ice) Cherenkov detectors [61]. Both are based on the indirect detection of traversing shower particles by production of scintillation light or Cherenkov emission, respectively. Such detectors can be converted into dedicated muon detectors by additional shielding from the electromagnetic component, e.g. by high density materials or simply by a few meters of soil, i.e. by burying the detectors. In combination with unshielded detectors, air-shower arrays can measure the electron/muon ratio and, thus, are sensitive to the primary mass. A similar sensitivity can be achieved via combination of different detector types with differing response to electrons and muons.

Air fluorescence detection

Air fluorescence emission is based mainly on inelastic collisions of electrons/positrons of the air-shower with air molecules [67]. The radiative de-excitation, predominantly of nitrogen molecules, can be observed roughly in the $300 - 400\,\mathrm{nm}$ range [61]. The fluorescence emission is isotropic and can therefore be detected from any direction via fluorescence telescopes. The fluorescence technique allows for a calorimetric energy measurement [64] as well as a direct observation of the longitudinal shower profile [68], leading to direct sensitivity to X_{max}. A major source of uncertainty for this technique is introduced by the limited knowledge of the atmospheric conditions.

Air Cherenkov detection

Since many of the air-shower electrons and positrons are faster than the speed of light in Earth's atmosphere, Cherenkov light is produced [64]. Air Cherenkov emission can for example be detected via photomultipliers distributed over a large area, such as Tunka-133 [69]. With such detector arrays the information about the full shower development can be obtained, since, due to comparably small absorption effects, photons from all development stages are measured [61], enabling access to X_{max}. Moreover, at the observed wavelengths the Cherenkov light is emitted incoherently, leading to a proportionality of light intensity and shower energy [64]. However, a disadvantage of the air Cherenkov method is the limited duty cycle, as the Cherenkov emission

can only be observed in clear, moonless nights [61]. Additionally, in contrast to the fluorescence technique, the air-shower has to point towards the detector array [61], since the Cherenkov light is emitted in forward direction.

Radio detection

The radio signal emitted by air-showers is produced by two effects, the geomagnetic and the Askaryan effect. However, for less dense media such as air, the geomagnetic effect usually dominates [64].
The geomagnetic effect is based on the deflection of electrons and positrons produced during the shower development in opposite direction to the geomagnetic field. On macroscopic level this charge movement results in a transverse electric current [64]. Since the number of electrons and positrons depends on the stage of shower development [70], this current varies with time. Analog to a Hertz dipole, this leads to linearly polarized radio emission, orthogonal to the geomagnetic field [64].
The Askaryan effect is based on the ionization of atoms in the atmosphere during the shower development due to photons. The electrons from such ionization processes are either carried on as part of the electromagnetic shower, in contrast to the massive ions, or annihilate with positrons of the shower. Both effects lead to a time dependent negative net-charge carried by the shower front and a positive ion plasma behind the shower. Taking into account the large electron density in the shower core this net-charge can be approximated by a time dependent point-like charge [64]. Hence, the resulting radio emission is polarized radially with respect to the shower axis [71].

Similar to the air Cherenkov emission, the radio signal is beamed in forward direction [72]. Since, however, due to the large wavelength, the radio signal is emitted mostly coherently, the shower energy is quadratically proportional to the signal intensity and, thus, proportional to the signal amplitude [64]. A great advantage for radio detection compared to the fluorescence and Cherenkov methods is the unlimited duty cycle [64]. Moreover, radio detection constitutes an alternative access to $X_{\max}$ with comparable systematic uncertainties with respect to the air Cherenkov and air fluorescence techniques [9]. However, due to the interplay of two production mechanisms in the radio technique the error estimation is more complicated [9].
Currently, for very high energies in the EeV region the fluorescence technique achieves the most accurate energy determination via $X_{\max}$ measurement [73]. In the 100 PeV region air Cherenkov emission is often used [74]. The radio technique could be used starting from even lower energies while providing an unlimited duty cycle [75].

Chapter 3.

IceCube and IceCube-Gen2

The antarctic continent constitutes the largest ice mass on Earth [76] with a mean thickness of around 2 km [77]. This offers a unique opportunity for a three dimensional detector arrangement for neutrino measurements in combination with cosmic ray measurements. Due to the good optical properties of the deep antarctic ice [78] the measurement of highly energetic particles with optical detectors inserted into the ice becomes feasible. Such an in-ice detector arrangement in combination with a surface detector for the measurement of air showers provides a variety of new possibilities for cosmic ray science.

3.1. IceCube

The IceCube detector is a $1\,\mathrm{km}^3$ Neutrino Observatory located near the geographic South Pole [80]. An array of 86 in-ice strings with a spacing of 125 m and a total amount of 5160 digital optical modules (DOMs) [79] is designed to measure Cherenkov light emission of charged particles from interactions of astrophysical neutrinos in the ice (see Fig. 3.1). Eight out of 86 strings are spaced in smaller distances, constituting the DeepCore upgrade, which aims to measure low energy neutrinos.
The DOMs are located at depths between 1450 m and 2450 m. The almost 1.5 km thick ice layer on top of the detector volume acts as a filter for atmospheric muons, which constitute a major part of the background for astrophysical neutrino searches. Additionally, the deep ice has significantly better optical properties [78] which in turn improve the detection efficiency.
Each DOM contains one photo-multiplier tube (PMT) as well as the necessary electronics for a local digitization of the measured signals. For coincident hits in multiple DOMs the signals as well as their timestamps are recorded [79]. Via the spatial and temporal distributions of a particular event the characteristics of an incident neutrino can be reconstructed. The main parameters of interest are neutrino direction and energy. The latter can be inferred with the correlation between energy of a charged particle and the amount of produced Cherenkov photons, reflected in the measured signal intensity. In fact, the number of Cherenkov photons per path length produced by a particular charged particle are well understood [81], allowing for accuracies in reconstruction of the direction of incidence of $< 0.4^\circ$ for high energy muons [79]. For particles with less clear signal tracks like electrons and taus, however, the angular resolution is reduced [82].
In general, the IceCube detector is sensitive to all neutrino flavors. In particular, however, the possibility of a precise direction reconstruction for a high energy muon track from a charged current interaction of a muon neutrino (see Fig. 3.2) in the ice, allows for neutrino point source searches. Charged current interactions of electron as well as tau neutrinos manifest in a particle

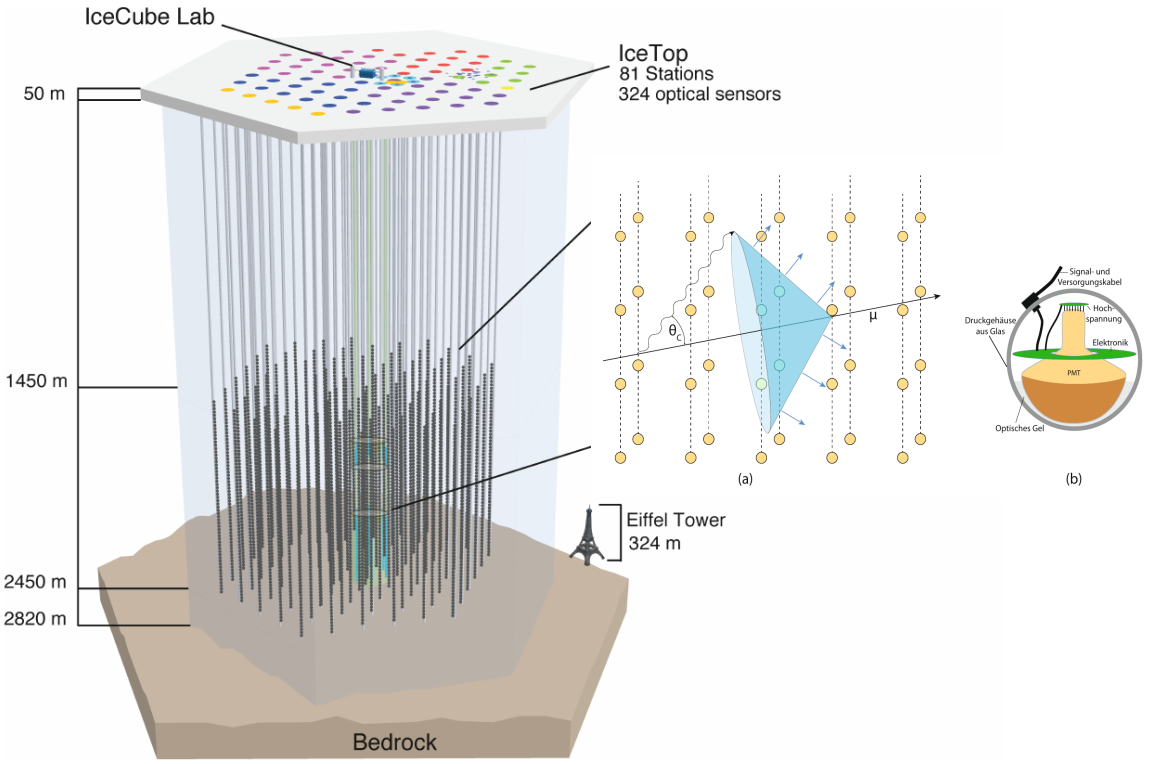

Figure 3.1.: Left: Schematic plot of the IceCube Neutrino Observatory. The surface array, IceTop, and the IceCube laboratory are located on top of the in-ice array. The DeepCore upgrade constitutes 8 additional photo-multiplier strings with denser spacing. Right: (a): Close-up of the strings illustrating the measurement principle. A high energy lepton from a neutrino interaction in the ice produces a Cherenkov cone (shown in blue), which can be measured by the digital optical modules (yellow spheres). The distribution of the measured signals as well as the signal properties are used to infer the characteristics of an incident neutrino. (b): Illustration of a single DOM, containing PMT and read-out electronics. The instrumentation is encapsulated in a glass sphere to withstand the pressure in the ice. Plot combined from [79, 1]

cascade [83] produced by the charged lepton. Although the direction information for a cascade is generally blurred, the neutrino energy can be reconstructed fairly accurately compared to muon neutrinos as the energy deposited by the cascade, is likely contained within the array [84]. Hence, these flavors are most suitable for diffuse neutrino searches.
It is important to mention that hadron cascades due to a nuclear recoil can be produced flavor independently in neutral current and charged current interactions for neutrino-nucleon scattering [79] (as illustrated in Fig. 3.2).

Science goals

Since neutrinos are not deflected by magnetic fields or absorbed during their propagation in our universe, they constitute unique messenger particles for the study of cosmic ray accelerators throughout the universe. Since neutrino production is associated with cosmic-ray acceleration, different model assumptions of the nature of the according acceleration processes can be tested by precise measurements of the astrophysical neutrino flux [10]. Additionally, point-source searches

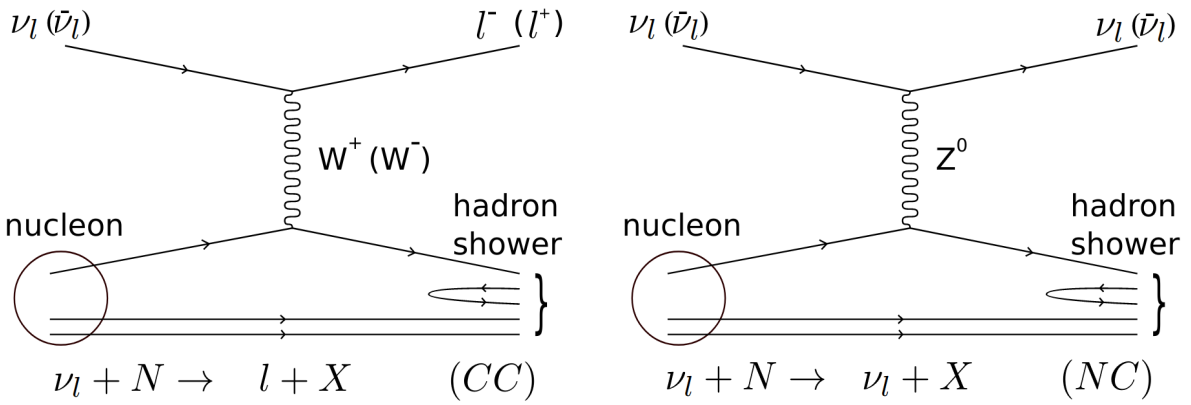

Figure 3.2.: NC and CC channel for deep inelastic neutrino-nucleon scattering. Adapted from [85].

can lead to the discovery of new cosmic accelerators. Hence, the nature as well as the location of such high-energy cosmic ray accelerators can be investigated.
On the one hand, however, since the measured neutrino flux is dominated by atmospheric neutrinos, a major challenge is the purification of the astrophysical contribution [79]. On the other hand, the large flux of atmospheric neutrinos is a unique opportunity for neutrino physics such as studies of seasonal variations in the neutrino flux [86] and neutrino oscillations, specifically with the DeepCore strings [87].

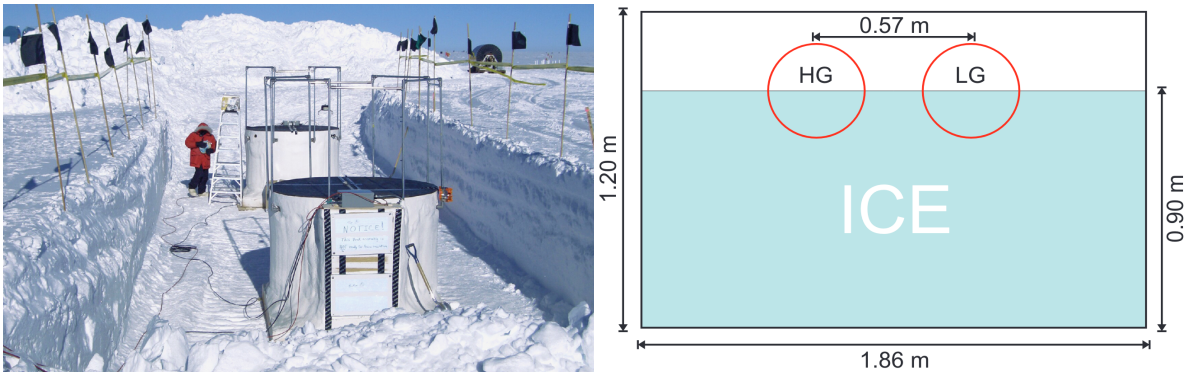

Figure 3.3.: Left: Picture of one IceTop station. The two ice-Cherenkov tanks are roughly 10 m apart. Photo taken from IceCube Collaboration during the deployment. Right: Sketch of one IceTop tank equipped with 2 DOMs (operating in high gain (HG) and low gain (LG), respectively). The DOMs are pointing downwards and are inserted in the ice volume. Plot taken from [88].

IceTop

In addition to the neutrino science, the IceCube detector is able to detect cosmic-ray air showers with PeV to EeV primary energies [5] with its 1 km^2 surface array, IceTop. The IceTop array is located above the in-ice array, featuring 2 ice-Cherenkov tanks close to each in-ice string [89]. The array of 162 tanks in total [90] is designed to measure the Cherenkov light produced by shower particles propagating through the tank volume. In order to efficiently detect the light emission each tank features two optical modules similar to the in-ice DOMs as well as a reflective

layer at the inner surface [89] (see Fig. 3.3). For a maximum dynamic range, one DOM in each tank is operating at high gain, the other at low gain [88]. A local coincidence condition, i.e., a coincident trigger of both tanks is used in order to reduce random coincidence trigger.

The IceTop array is located at an altitude of 2835 m [90], which is highly beneficial for the detection efficiency for cosmic-ray air showers as the shower development starts closer to the observation level. Hence, the shower maximum is reached closer to the detector array. Although the tank signal is dominated by the electromagnetic shower part [90], it is to some extent possible to disentangle muonic from electromagnetic contributions by a careful study of the signal distributions at large distances from the shower axis [91]. Hence, the IceTop array enables the study of low energy muons produced in air showers. This is a great advantage, in particular, in combination with coincident in-ice detection of corresponding high energy muons as the relative abundances and energies of the muonic component are sensitive to the primary mass and hadronic interactions [2]. In this context the harsh South Pole conditions are indeed beneficial as, due to snow accumulation, the IceTop tanks will be further buried over the years, effectively increasing the relative contribution of muons to the detected signal (however, at the expense of overall detection efficiency as the electromagnetic part is attenuated by the snow layer). Since the main background contribution for the in-ice array arises from cosmic-ray air showers, IceTop additionally constitutes a veto array for the neutrino detection for down-going events. In addition, IceTop is used as calibration tool for the in-ice array [80].

3.2. IceTop enhancement

Complementing to the IceTop array, a surface enhancement is currently under development. As mentioned, the snow coverage of the IceTop tanks is further increasing, leading to an increased detection threshold [92]. Thus, additional elevated scintillation detectors will be distributed within the IceTop array. Due to the elevation snow accumulation on top of the scintillation panels can be avoided. Therefore, the scintillators are planned to be utilized in calibration of the snow effects in the IceTop signals [5], which will reduce the systematic uncertainties introduced by the snow coverage [93]. The scintillation detectors will be arranged in 32 stations with uniform spacing [93], each featuring 8 scintillator panels (ordered as 4 pairs) oriented in a triangular shape (see Fig. 3.4).
In order to reduce deployment efforts and costs, plastic scintillator panels are used [94]. In fact, scintillator panels constitute a complementary detector type to the ice-Cherenkov tanks. This is caused by the fact that the IceTop tanks are more sensitive to the muonic shower component compared to scintillator panels. Hence, signal differences at certain distances from the shower axis can be utilized for mass discrimination [5]. A combined analysis of scintillator, IceTop and in-ice information will therefore allow for an improvement in primary mass determination [95]. In general, the scintillator enhancement will provide an increased sensitive area and therefore a reduced detection threshold [94]. This enables measurements of cosmic ray air-showers below the knee as well as increases the veto capabilities [5].

Moreover, each IceTop enhancement station includes 3 radio antennas, leading to a unique combination of a hybrid air-shower detector array with a deep in-ice array. A measurement of the radio emission is particularly sensitive to the electromagnetic shower component and therefore to the primary energy. Additionally, radio detection enables an X_{max} determination. Hence, radio antennas constitute a valuable complementary detection channel leading to a further enhancement in energy and mass reconstruction [96].

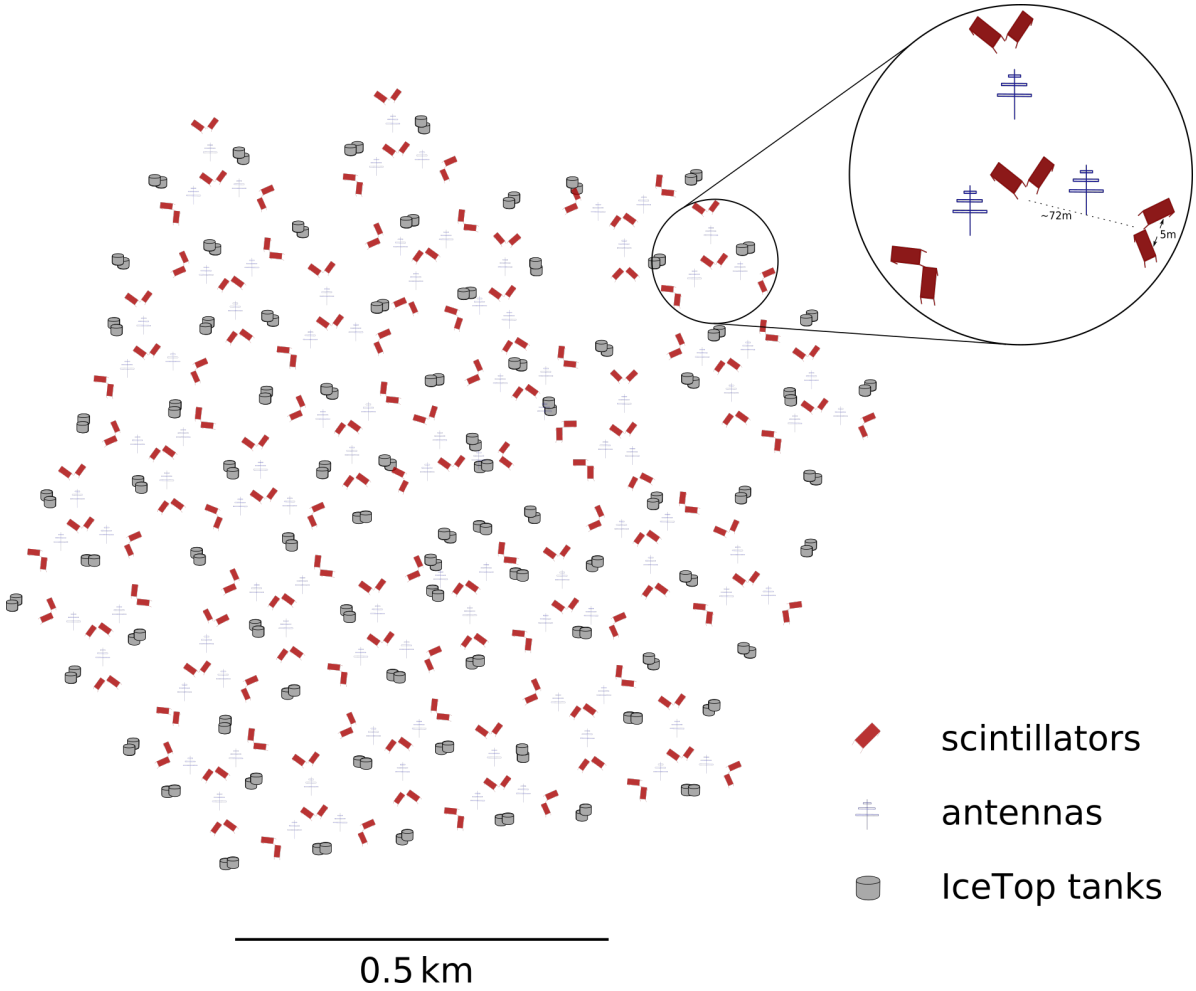

Figure 3.4.: Layout of the IceTop enhancement array with its 32 stations, each equipped with 8 scintillation detectors and 3 radio antennas. Plot inspired by [5].

While the scintillator array features a low detection threshold for rather vertical showers, the radio array is most sensitive for high inclinations [95], however, with a generally higher threshold. Thus, the composition in the transition region between Galactic- and extra-galactic cosmic rays can be studied for a large range of primary zenith angles. The sensitivity to inclined air-showers could additionally be of great use for the veto capabilities of the surface array. Furthermore, with in-ice and surface information, more precise tests of hadronic interaction models can be performed [95]. Additionally, since photon induced air showers feature slightly stronger radio emission and a smaller muon content, the combination of radio antennas and muon measurements will allow for searches of PeV photons [96]. In 2018 two prototype stations have been deployed at the South Pole, each equipped with 7 scintillator panels [5]. For studies regarding detector response and data acquisition, the two stations were placed at the same location [95], featuring slight differences in mechanical design [5] and data acquisition system (DAQ) [95].
The prototype stations were able to detect coincident signals from air-showers, which could then be reconstructed, yielding azimuth and zenith resolutions in agreement with the reconstruction of the IceTop array [5]. In the following year, the first prototype radio antennas were deployed [98].

In January 2020, the two stations have been replaced by one full IceTop enhancement station featuring 8 scintillator detectors and 3 radio antennas, which has been taken data over the past

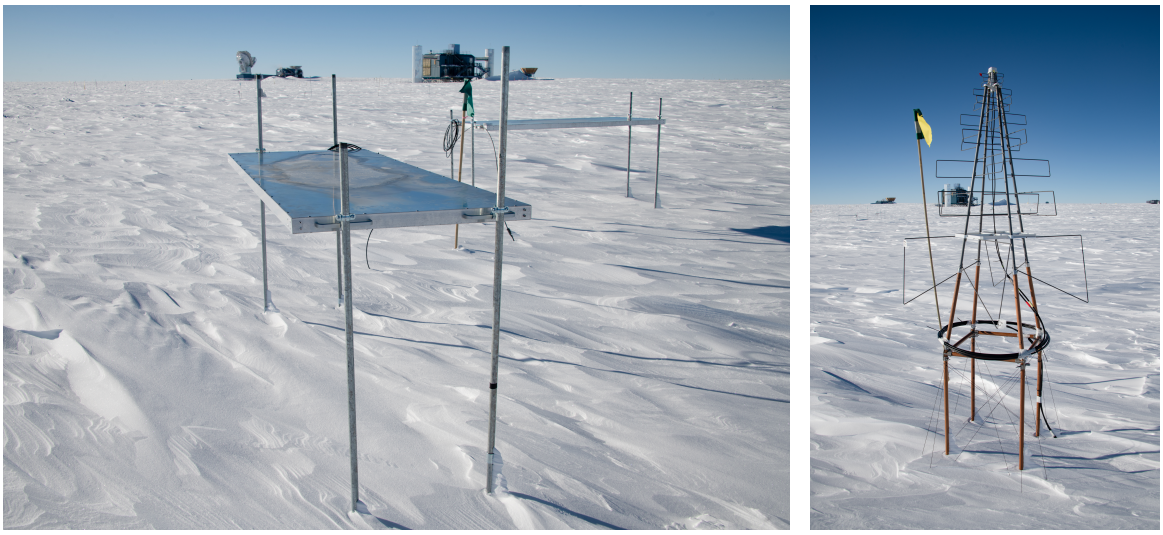

Figure 3.5.: Picture of two elevated scintillator panels (left) and a radio antenna (right) deployed at the South Pole. Taken from the IceCube Collaboration.

year [97]. For the hybrid detection the scintillator panels provide the trigger for the radio antennas.
In fact, first hybrid measurements as well as reconstructions were carried out (see Fig. 3.6). The rather basic event reconstruction used for the hybrid measurement with one station yields matching primary directions compared to the IceTop reconstruction [97]. More elaborate reconstruction procedures will allow for further improvements.

Scintillator characteristics and readout

In general, plastic scintillators feature fairly fast response times which is very beneficial for trigger applications [1]. Charged particles traversing the scintillator material deposit energy, which in turn leads to the excitation of molecules of the scintillator material. The light emission then takes place via de-excitation. However, depending on the electron spin coupling, the de-excitation can occur from excited singlet or triplet states. The important channel for the detection of scintillation emission is the de-excitation of singlet states, since these states are less stable leading to prompt ($\mathcal{O}$(ns)) light emission. Triplet states are only occupied via radiation-less transition from singlet states [1]. The emission from these meta-stable states takes place within the order of ms. However, a transition back to a singlet state due to further energy absorption in combination with a subsequent de-excitation can lead to slightly delayed light emission ($\mathcal{O}$(μs-ms)) [1] and can therefore contribute to the overall signal measured in a scintillation detector [5].

In order to improve the light yield as well as the light absorption, the basic scintillator material is usually doped with further scintillation materials. The dopants are further used for wavelength shifting [5] as the quantum efficiency of photomultipliers differs for different wavelengths.

The plastic scintillator panels foreseen for the IceTop enhancement array contain 16 single polystyrene[1] scintillator bars, which in total produce a sensitive area of 1.5 km^2 [93]. The 32 wave-

[1]Doped with 1% PPO and 0.03% POPOP and coated with a TiO_2 reflective layer [5]

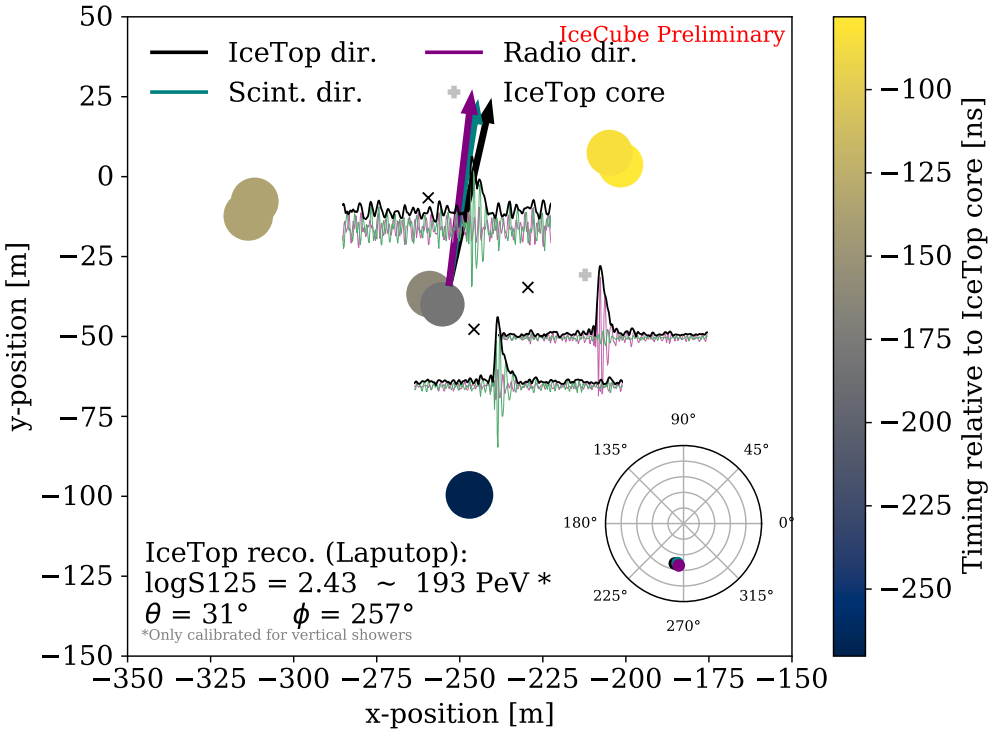

Figure 3.6.: Example reconstruction of an air-shower event observed with the prototype station. Size and color of the circles indicate the charge and timing information, respectively, for all hit scintillation panels. The three black crosses indicate the position of the radio antennas. The position of the shower impact point is shown with a light gray +. The colored arrows illustrate the direction reconstruction from IceTop, the scintillation detectors and the radio antennas. S_{125} (signal strength at a distance of 125 m from the shower axis) constitutes the primary energy proxy. Plot taken from [97].

Figure 3.7.: Picture of the inside of one scintillator panel comprised of 16 scintillator bars. The wavelength shifting fibers are of same length in order to guarantee similar light propagation in each part of the scintillator panel. The fiber bundle is then connected to the SiPM. Picture taken from [99].

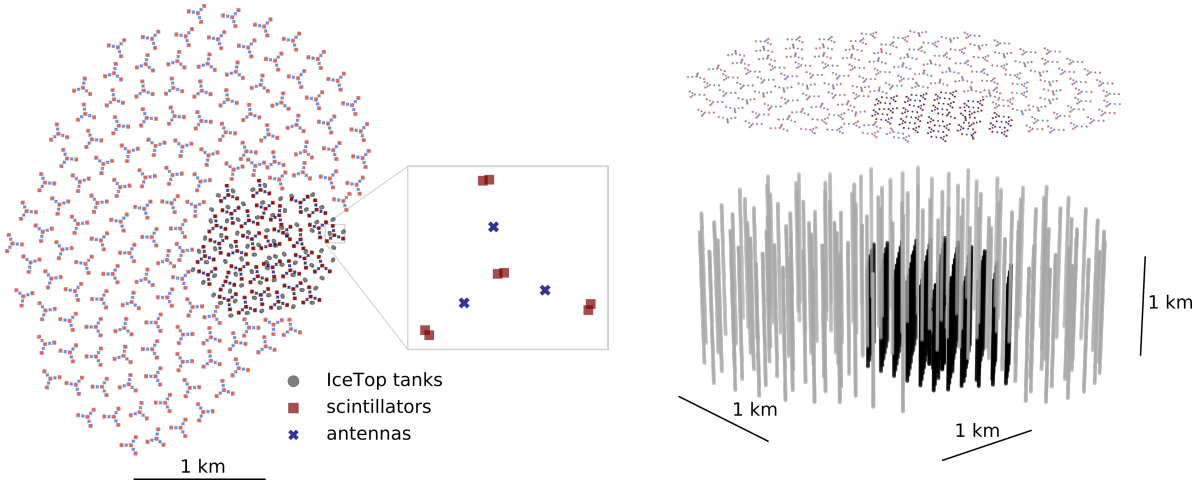

Figure 3.8.: Left: Top view of the baseline design of the IceCube-Gen2 surface array. One surface station is planned to be installed on top of each in-ice string. Right: IceCube-Gen2 detector with its in-ice (gray strings) and surface component. The IceCube in-ice array is shown in black. Plot taken from [3].

length shifting fibers used for the light collection are routed through holes in the scintillator bars. The resulting fiber bundle is then read out via Silicon Photomultiplier (SiPM) [100] (see Fig. 3.7).
Styrofoam pieces as well as wooden support structures between scintillator bars and casing provide mechanical stability [5]. The scintillator panels are further wrapped in polyethylene foil in order to achieve light-tightness [5]. Finally, an aluminum case encloses all parts and protects them against environmental conditions.

The data read-out is performed via a microprocessor-based DAQ board (MicroDAQ), featuring ~ 1 ns time resolution [100]. The digitized data is forwarded to the FieldHub in the center of the station, where the 'Transportable Array for eXtremely large area Instrumentation' (TAXI) for the data acquisition is located. The TAXI board allows for a connection of additional sensors with analog waveform readout [101], such as radio antennas. For the full IceTop enhancement array, the FieldHub of each station then acts as a communication network connected to the IceCube Laboratory (ICL) with a sub-nanosecond synchronization achieved via a special Ethernet-based network (White Rabbit [102]) [100].

3.3. IceCube-Gen2

The successful science of IceCube led to the proposal of a possible next generation Neutrino Observatory, IceCube-Gen2 (see Fig. 3.8), which extends IceCube by 4 new components. Namely, ordered by size of the according extension, an in-ice radio array, an in-ice optical array, encompassing the IceCube in-ice array, a surface array, following the footprint of the optical array, and a low-energy core, complementary to the in-ice strings (IceCube upgrade) [103]. The latter includes the extension of the DeepCore array by 7 additional strings, leading to improved sensitivity for the measurement of GeV neutrinos [104]. The denser spacing due to the additional strings and the denser instrumentation per string[2] will provide the increased light collection

[2]Vertical spacing between two PMTs decreased from 7 m for the DeepCore strings to roughly 3 m for the upgrade strings [105]

potential [106] necessary for an energy threshold in the few GeV region. Of particular interest in the context of the low-energy extension are precision measurements of the disappearance as well as the appearance channel[3] of ν_μ and ν_τ, respectively [108]. These measurements will be complementary to future measurements of long-baseline experiments [104]. Another science capability related to such oscillation measurements is the study of the neutrino mass ordering [106]. This is possible with a combined analysis of measurements with the IceCube low-energy upgrade and JUNO[4], resulting in a possible $> 5\sigma$ discrimination between normal and inverted mass hierarchy within a few years [106].
In addition, the position and denser instrumentation of the Upgrade strings enable a more efficient discrimination of through-going atmospheric muons, mimicking neutrino events in the upgrade detector, via time and spatial distribution of the pulses measured for a given event [105]. Thus, the background of atmospheric muons can be reduced significantly, allowing for more precise neutrino flux measurement. In particular, a precise knowledge of the neutrino flux in the GeV region is necessary to search for dark matter annihilation in the Galactic Center and in the Sun [105], which would result in an excess of low energy neutrinos in the according direction.
The IceCube low-energy upgrade denotes the first step towards the complete IceCube-Gen2 detector.

Focused on high energy neutrino events between roughly 10 TeV and 10 EeV, the IceCube-Gen2 optical array will increase the current detector volume by a factor of ~ 8, overcoming the challenge of the low flux at high energies [104]. In total, this optical array will contain 120 additional strings[5] with distances of around 240 m, roughly doubling the string spacing compared to IceCube. Thus, while covering a much larger area, the instrumentation will increase by only a factor of 2. The choice of an increased string spacing is based on multiple factors. On the one hand, new calibration methods for the optical modules will be available for IceCube-Gen2 [103]. Techniques like calibration via cosmic ray muons [79], acoustic positioning systems [111] and camera systems [112] for geometry as well as orientation calibration will allow for a less tight restriction of the string spacing. On the other hand, the optical modules planned to be used for IceCube-Gen2 are expected to increase the light yield by a factor of 3 compared to the IceCube DOMs [103]. Similarly, the more detailed knowledge about the ice properties gained by previous studies for IceCube [113, 78] along with the possibility to investigate ice properties with camera systems installed with the DOMs [112] are further advantages. Further, the focus on higher energy, hence, brighter events, relaxes the string spacing requirements. Moreover, the larger distance between strings intrinsically leads to a higher suppression of the atmospheric muon background by lifting the energy threshold for through-going muons to above 10 TeV [103].
However, these advantages are, at a certain point, overshadowed by the reduced direction resolution and increased energy threshold accompanying a larger string spacing [103]. In order to balance the decisive effects while being able to experimentally examine the expected performance of the IceCube-Gen2 optical array by including signals from only one out of four strings in the IceCube analysis, a string-to-string distance of 240 m was chosen [103]. The IceCube-Gen2 strings are positioned in a 'sunflower' geometry around the IceCube detector, prohibiting non-instrumented corridors within the array (see Fig. 3.8).

Since in-ice showers additionally produce radio emission (predominantly via Askaryan effect), the

[3] Since the oscillation probability varies with L/E [107], where E denotes the neutrino energy and L the path length (hence, Earth's diameter), lowering E results in a higher oscillation frequency

[4] JUNO is a reactor anti-neutrino experiment currently under construction, which primarily aims to determine the neutrino mass hierarchy by measurement of 3 oscillation parameters, namely $\sin^2\theta_{12}$, Δm^2_{12} and $|\Delta m^2_{ee}|$, with $< 1\%$ precision [109, 110]

[5] Each IceCube-Gen2 string will contain 80 optical modules, leading to a total of 9600 additional modules [103]

radio extension of IceCube-Gen2 will further improve the neutrino detection for high energies. In the baseline design the 200 stations, each equipped with shallow and sub-surface antennas, are distributed over 500 km^2 [103]. With attenuation lengths of the order of 1 km in the antarctic ice, neutrinos with $\gtrsim 30$ PeV can be detected via radio measurements [114]. The combination of shallow antennas near the surface with antennas in depths of roughly 100 m will provide increased veto capabilities as well as a large effective volume, respectively [103]. In order to allow for reconstruction of direction, energy and vertex position, each station contains three strings hosting the deep antennas.

Similar to IceCube, IceCube-Gen2 is planned as a 3-dimensional neutrino observatory. In this concept, the Earth acts as an intrinsic filter for cosmic ray induced up-going background events [115]. An effective suppression of down-going background events can be achieved by utilizing cosmic-ray air shower detectors as a surface veto, as proven with IceCube and it's surface component, IceTop [90]. With IceTop, the astrophysical neutrino flux measured by IceCube exceeds the background for energies roughly above $200 - 300$ TeV [103]. With the combination of scintillation detectors and radio antennas from the IceTop enhancement and the IceTop tanks, these veto capabilities will be further enhanced. Such enhanced veto capabilities are in particular important in the context of real time alerts.

3.4. IceCube-Gen2 surface array

Similar to IceCube, an cosmic-ray air shower array at the surface of IceCube-Gen2 can constitute a veto for the atmospheric background for astrophysical neutrino detection in the ice. Among other reasons, this is why the planned IceCube-Gen2 Neutrino Observatory features a surface array, which, in the baseline design, is comprised of IceTop enhancement[6] stations following the footprint of the optical array. Additionally, 8 stations within the gap between the IceTop array and the IceCube-Gen2 surface array will provide a smooth coverage (see Fig. 4.1). Moreover, for cross-calibration purposes a small overlap of the surface array and in-ice radio array is planned [103]. In fact, due to the combination of a larger area and angular range for coincidence detection, the aperture of IceCube-Gen2 for coincident events increases by more than a factor of 30 compared to IceCube [116], which can significantly enhance the veto capabilities.
Similar to the IceTop enhancement, the low threshold of the scintillation detectors can provide an efficient veto for rather vertical down-going neutrino events. Since radio antennas become more efficient for inclined air showers [3] they might be used as veto detectors for inclined down-going events [2]. However, first and foremost, the IceCube-Gen2 surface array is designed to be a powerful hybrid cosmic-ray air shower detector.
In total, the IceCube-Gen2 surface array will contain a roughly 8 times larger area, increasing the range of air shower measurements to a few EeV primary energy. Due to the increased aperture, at around 1 EeV roughly a few hundred events per year with coincident surface and in-ice measurements are expected [103, 3]. Overall, the unique combination of hybrid surface and in-ice information allows for measurements of the mass-dependent cosmic-ray energy spectrum in the transition region [2]. The measurement of the relative signal contributions at the surface and deep in the ice is crucial for gamma-hadron discrimination [103] and therefore enables PeV gamma ray searches. Due to the larger aperture, such searches can be carried out with significantly increased statistical sensitivity compared to IceCube [2].
For both, the IceTop enhancement and the IceCube-Gen2 surface array, SKALA-2 [117] radio

[6] Depending on the further experience with the performance of the IceTop enhancement stations improvements can still be applied.

antennas are planned to be used [97, 2]. With this antenna type two polarizations can be measured independently. Over the entire frequency band of $70 - 350\,\mathrm{MHz}$ the noise is limited to the Galactic contribution as each polarization channel features a low-noise amplifier [2].
Similar to the enhancement array, the scintillation detectors will be used as trigger for the radio antennas. The DAQ system is currently planned to be similar as for the enhancement stations, however, with a new version of the TAXI system [2, 118].
The design of the IceCube-Gen2 surface array will be discussed in more detail in section 4.2. The variety of the science cases for the IceCube-Gen2 surface array in the context of the performance of the IceCube-Gen2 scintillator array will be discussed in section 5.4. An overview of the general science case can be found in [2].

Chapter 4.

IceCube-Gen2 scintillator array simulations

A comprehensive simulation study on the performance of the IceTop enhancement array promises a significant improvement in detection efficiency in comparison to IceTop, due to denser arrangement of the detectors [5]. The enhancement will be used to better understand the influence of snow accumulation on the IceTop tanks. Moreover, such extension towards the low energies is in particular important for studies of the cosmic-ray energy spectrum in the region of the 'knee'. For detailed studies it is crucial to enhance the mass discrimination and energy determination capabilities of the air-shower array. This can be achieved by utilizing hybrid detections, i.e., in the case of the IceTop enhancement, with ice-Cherenkov tanks and scintillation panels as well as radio antennas and an in-ice optical array. Further, the IceTop enhancement will help vetoing atmospheric background for down-going astrophysical neutrino searches.
On the other hand, towards higher energies a larger array of surface detectors is planned as part of IceCube-Gen2 and is based on the experience of the development of the enhancement array [3], including the operation of a prototype station already deployed at the South Pole [2]. In the baseline design, the IceCube-Gen2 surface array will comprise detector stations similar to the ones proposed for the IceTop enhacement. Thus, each station features 8 scintillator panels and 3 radio antennas, oriented in a triangular shape.
In contrast to the IceTop enhancement, the detector stations will be distributed more sparsely over a roughly 8 times larger area. Nevertheless, the Gen2 surface array is planned to provide a lower detection threshold than IceTop while extending the energy range to several EeV. Similar to IceTop, it will act as a veto array for the astrophysical neutrino detection, significantly reducing the atmospheric background as already proven for IceTop/IceCube [119]. Due to the considerably larger aperture, such veto capabilities will be further extended to larger zenith angles [2].
In principal, especially to reject atmospheric background for astrophysical neutrino searches, the threshold is desired to be as low as possible. More specifically, however, in particular for tests of hadronic interaction models based on prompt muon studies (as discussed in more detail in section 5.4), a detection threshold of roughly 500 TeV is required.
With such a large hybrid air-shower array precision measurements of the cosmic-ray energy spectrum in the transition region of Galactic to extragalactic sources [3] as well as more detailed studies of cosmic-ray anisotropies become feasible. Furthermore, combined detections of surface and in-ice array provide a unique possibility to enhance the mass separation potential for cosmic-ray spectrum analysis as well as to validate different hadronic interaction models [2]. Both aspects will be elaborated in more detail in section 5.4.

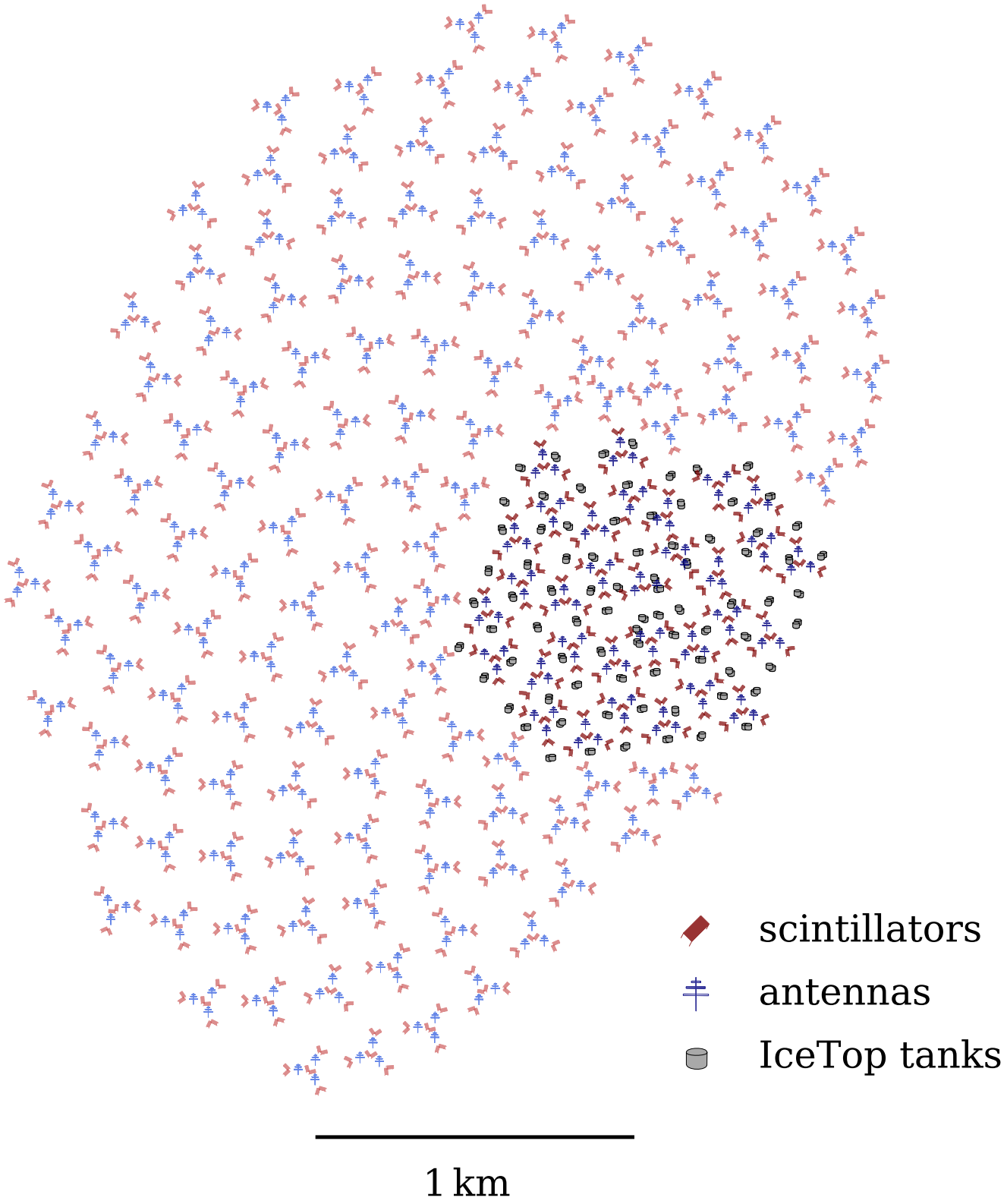

Figure 4.1.: Layout of the IceCube-Gen2 surface array. Each Gen2 and IceTop enhancement station (darker colors) contains 8 scintillation detectors and 3 radio antennas. The IceCube-Gen2 surface stations are distributed in a 'sunflower' geometry around the IceTop/IceTop enhancement array.

In order to quantify the contribution of the scintillator detectors of the IceCube-Gen2 surface array to the different science capabilities in more detail, an according simulation study of the scintillator array was performed within the frameword of this thesis. The simulation chain as well as the according results for the scintillator simulations for different station layouts and studies of the lateral distributions are discussed in this chapter.

4.1. Simulation chain

The simulation chain is comprised of two steps. First of all, the development of cosmic-ray air showers is simulated. These air showers are further injected onto the Gen2 scintillator array by specification of the shower impact point on the ground. Secondly, the detector response is simulated by propagation of the particle content of a particular air shower at the detector level through the single scintillator panels. The details of both steps are discussed in this section.

4.1.1. Air shower simulation

The simulations of cosmic ray air showers are performed via CORSIKA (COsmic Ray SImulations for KAscade) [120]. This Monte Carlo tool was originally developed for the KASCADE experiment [121] and is currently the world leading tool for air shower simulations.
Within CORSIKA the cascade formation and propagation through the atmosphere is simulated. For this purpose the first interaction is determined randomly by taking into account the specific cross section for a particular primary type. The propagation includes electromagnetic and hadronic interactions, particle decays as well as deflection in Earth's magnetic field [120]. Each secondary particle is tracked explicitly to then store the particle momentum and properties at a particular observation level.
In order to be fully applicable for any experimental site, CORSIKA allows for individual configuration via steering card (see [122] for more details). An overview of the CORSIKA settings used for the simulation study presented in this thesis is shown in Tab. A.1.

For the simulation of interactions and decays CORSIKA relies on specific theoretical models for both electromagnetic and hadronic processes. CORSIKA allows for air shower simulations with primary energies beyond EeV. Hence, the choice of a particular hadronic interaction model is highly relevant as it introduces large systematic uncertainties for high energy showers, as the models are only extrapolated from collider energies. The CORSIKA[1] simulations used in this thesis are compiled with FLUKA (2011.2x.7) [123] and SIBYLL[2] 2.3d [124] for hadronic interactions in the low and high energy region, respectively [3].
In addition, for high energy showers the computing time is significantly larger. Therefore CORSIKA offers the application of a thinning algorithm which drops secondary particles below a certain energy threshold and instead applies a weighting to the remaining particles. However, within this thesis it was not necessary to apply this algorithm.

In order to limit the amount of stored particles at the observation level, CORSIKA introduces cuts on low energy particles which would not be detected [5]. Proper lower energy cuts for

[1] Version number 7.7401

[2] SIBYLL is specifically designed for MC simulations of extensive air showers. It takes into account the soft and energy-dependent hard cross section in hadronic collisions [122]. Since for the modeling of hadronic interactions at high energies the nuclear binding energy can be neglected, the interaction of a primary nucleus with mass A is approximated as A separate interactions [124]

different particles were derived within the scope of IceTop enhancement simulations [5]. For hadrons and muons the lowest cuts provided by CORSIKA are used, i.e. 20 MeV and 10 MeV, respectively.

4.1.2. Array response simulation

The particles at the observation level obtained from the CORSIKA simulation are further propagated through the scintillation detectors. The response simulations are carried out via Geant4 (version 10.4.0 [125]) by calculation of the overall energy deposit of a particle traversing the sensitive detector volume. For the determination of deposited energy, electromagnetic as well as hadronic interaction models are utilized. For the former all predominating interaction processes, such as bremsstrahlung, ionization, pair production, Coulomb scattering and annihilation, are considered [5]. Since hadronic interactions are not yet well understood in some energy regimes, additional phenomenological models are used [126].
The proper implementation of the according detector geometry has been performed within the scope of a comprehensive simulation study for the IceTop enhancement array [5]. The physical parameters and interaction models necessary to describe the propagation of air shower particles in direct vicinity of and within the detector volume are adjusted via *G4ModularPhysicsList* [125].
Since the cross sections of many processes like bremsstrahlung and ionization become very large for low particle energies, production cuts below which no further particles are produced are introduced [126]. However, the according energy of the particle is accounted for as energy deposit. These so called 'range cuts' are set to 0.5 mm for photons and 0.1 mm for electrons, positrons and protons for all materials [5]. If a particular particle has an expected range of less than the value specified as range cut, no further particle is produced.

For the response simulations the projects *topsimulator* and *g4-tankresponse* of the IceCube software, originally developed for the IceTop simulations, have been extended with according modules for scintillation panels as well as radio antennas and are now part of the *SurfaceArray* meta-project within the IceCube software [5]. Within these two projects, particle injection into the array and the response simulation are incorporated.
In order to simulate the response for a particular array design, a *GeometryCalibrationDetector* (GCD) file has to be created, which then also contains the position[3] and orientation of the specific detectors. Only particles in direct vicinity of the detectors are passed to Geant4.
The signal in each detector is then given by the sum over the signals of all particles (including the noise within the signal) within a time interval of roughly 200 ns. For the summation the measured PEs (photo electrons[4]) are grouped into 5.55 ns bins. The bins are then summed up starting at the first bin with $\geq$4 PEs. This procedure approximates the PE integration performed with the real microDAQ system [5]. The start time of the first bin is taken as signal time.

In general, the light yield of a scintillator depends on the energy deposit and therefore on the particle type. For this purpose a detailed study of the scintillator response for single muons, electrons and photons was carried out within the scope of IceTop enhancement simulations [5]. Generally, up to a few MeV, electrons are detected efficiently, as their full energy is deposited. For increasing energy, however, the ionization reaches a plateau [5]. Relativistic muons as minimum ionizing particles (MIPs) deposit only a minimum amount of energy when traversing the detector volume. This leads to a constant ionization rate above roughly GeV energies. For

[3]For the moment all scintillator panels are chosen to be at the same altitude.
[4]The number of scintillation photons is calculated via non-linear Birks' equation [127]

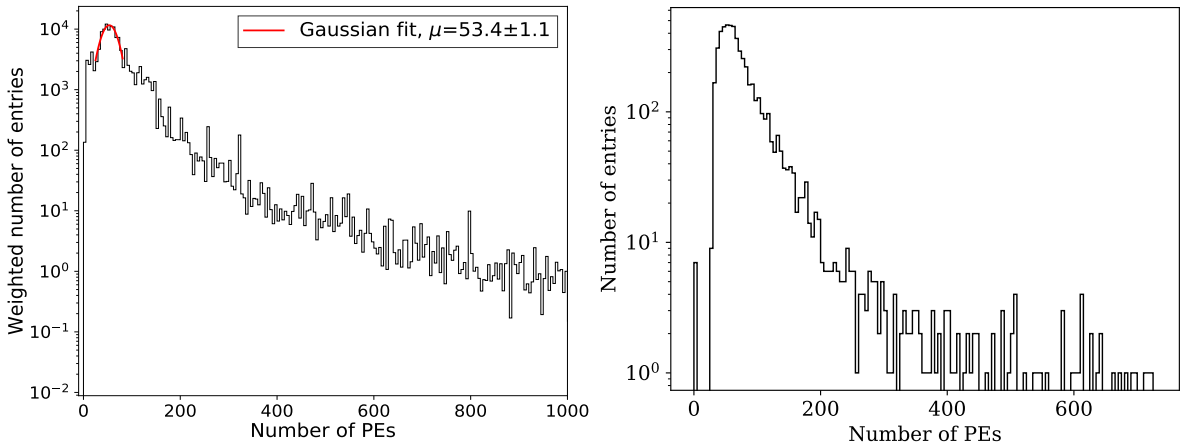

Figure 4.2.: Left: Simulated charge distribution as function of PEs. The Gaussian fit to the MIP peak is shown in red and corresponds to a mean value of ≈ 53 PEs/MIP. Plot taken from [128]. Right: Example charge distribution with real data from one scintillator panel, measured with medium amplification. The time between the first and last hit corresponds to ∼ 6 s. The two peaks at the beginning and the end of the histogram correspond to the baseline and saturation of the electronics, respectively. Plot taken from [129].

low energies, photons deposit only a small amount of energy, primarily via Compton scattering.

Since a detailed simulation of the light propagation through the fibers is very CPU intensive, instead a parametrization of the propagation efficiency is applied. For this purpose, vertical muons were injected uniformly into a single detector The parametrization obtained from the response of a single panel is then used to account for attenuation effects and time delays during the light propagation.

An additional influencing factor is the noise caused by the electronics. Currently, however, only the SiPM noise is simulated, accounting for thermal noise, delayed triggers from after-pulses[5] as well as correlated noise, such as optical cross-talks[6] [132]. Overall, this constitutes less than roughly 10% to the total signal [5].

In order to process the scintillator signal, it is converted into units of MIP. For this purpose, the simulated spectrum of charges observed with the scintillation detectors, with a threshold of 4 PEs in a single detector, was used. The simulations include H primaries with energies of 1 TeV − 1 PeV and zenith angles up to 90°, weighted with the total flux given by the *Global Spline Fit* (GSF) model[7] [128]. The peak in the charge spectrum produced by minimum ionizing particles can be modeled with a Gaussian and the peak value is further used as calibration factor (see Fig. 4.2 (left)). The Gaussian mean corresponds to 53 PEs/MIP and is used as calibration factor for the scintillator simulations. It should be noted, however, that, since this factor is derived based on simulations, it does not account for all influences of the electronics. Additionally, in real measurements the conversion factor itself is strongly temperature dependent [97]. However, this can be accounted for by temperature monitoring and according adjustment of the SiPM bias voltage [93].
In Fig. 4.2 (right) an example charge histogram for a real measurement with one panel is illustrated. The number of PEs is converted from ADC (Analog-to-digital converter) counts

[5]Caused by the release of trapped electrons [130]
[6]Secondary photons which are produced in coincidence to the primary photon [131]
[7]The GSF model is a data driven cosmic ray flux parametrization for primary energies of 10 GeV to 100 EeV [21]

measured with a MicroDAQ based system. The data corresponds to a run with approximately 6 s between first and last hit. Due to the limited time only a few large signals are observed. Differences in the distribution compared to the simulated spectrum likely correspond to the characteristics of the DAQ (more details about the DAQ can be found in [133]). To increase the dynamic range, each MicroDAQ has three (high, medium and low) amplification channels. The illustrated data is measured with medium amplification and a threshold of ~ 0.5 MIP.

4.2. Considered station layouts

In general, the specific design of an air shower array is driven by the science goals requirements. For the scintillator array of IceCube-Gen2, this mainly requires a low energy threshold for the veto capabilities and a well working reconstruction for cosmic-ray studies. Both requirements greatly benefit from a dense detector arrangement and a smooth surface coverage. From a feasibility perspective, however, the detector spacing is basically limited to what is necessary for the science case. It is therefore important to quantify the performance of the baseline design of the IceCube-Gen2 scintillator array and possibly adjust the array design to reach the mentioned requirements.
However, the surface array design is imposed by the arrangement of the IceCube-Gen2 in-ice strings as the field hubs will be placed in their vicinity. For the veto capabilities as well as the reduction of the overall deployment costs, one station above each in-ice string is desirable.
Thus, while the positioning of the single stations is practically fixed (translating to $\sim$240 m station spacing), the exact station design as well as the station orientation can be adjusted for an optimized array layout.

Within the scope of the IceTop enhancement, the detection efficiency for many different station considerations was simulated [5]. An optimal station design was chosen to feature 8 scintillation panels oriented in pairs on a triangular shape with radio antennas positioned between two pairs of scintillators. In addition to the low detection threshold around a few 100 TeV provided by the IceTop enhancement, the according array design accounts for infrastructural limitations, including trenching and other challenges regarding deployment. The station design is illustrated in Fig. 3.4.
Based on the simulation studies for the IceTop enhancement as well as prototype measurements, the baseline design of the IceCube-Gen2 surface array was chosen to feature a similar surface station on top of each in-ice string. Hence, the station spacing will be roughly doubled, with an active area of 1.5 m^2 [5] per scintillator panel.
In principal, the positioning of the strings in a 'sunflower' geometry already aims to prohibit non-instrumented passages in which high energy particles in the ice might remain undetected. For the surface array, apart from the general positioning of the single stations also their orientation among one another influences the detection. For this reason, the baseline design was optimized by tuning the station orientation to mitigate larger gaps between single stations that might compromise the uniformity of the surface coverage. All stations along one curve of the 'sunflower' geometry share a common rotation angle with respect to an initial orientation. A separate rotation angle is applied for every curve[8]. The resulting array layout along with the orientation of every single panel is illustrated in Fig. 4.1. It should be noted that the exact positioning and rotation of detector stations will most likely be further adjusted with respect to

[8] A further optimization by applying different rotation angles for every single station is possible. In this context, however, the deployment strategy should be taken into account.

the exact deployment strategy and the minimization of cable lengths.
Moreover, since a restriction of one surface station per in-ice string still leaves an un-instrumented gap between the IceTop/IceTop enhancement array and the IceCube-Gen2 surface array, 8 additional stations are foreseen to provide an according infill array. Despite the fairly small size of this gap it can lead to a higher detection threshold for air showers falling into this region. For this purpose a dedicated study on the maximum influence of such additional stations was performed (see App. B). Since, for showers falling into the gap, the threshold requirement of 500 TeV for vertical proton primaries can only be fulfilled with such infill stations, they are part of the baseline design and are included in the simulation studies presented in this thesis.
In total, the full IceCube-Gen2 surface array will contain 162 stations. 32 stations are part of the IceTop enhancement, the remaining ones are composed of 122 stations, one for each Gen2 in-ice string, plus additional 8 infill stations.

For the quantification of the detection efficiency for different station designs, the scintillator array response for proton initiated air showers is simulated. The simulations include primary energies between $\log_{10}(E/\mathrm{eV}) = 13 - 16.5$ with zenith angles up to 45°. In order to provide enough statistics, the simulations include 100 individual showers per energy and zenith bin. Each bin has a width of 0.1 in $\log_{10} E$ and $\sin^2\theta$, with E and θ denoting the primary energy and zenith angle, respectively. An overview over the according simulation set is shown in Tab. A.2. The showers are sampled over the full IceCube-Gen2 surface array. However, for the analysis, only showers with true core position up to 100 m to the array border are taken into account, roughly leaving out the outermost stations. This core selection is used as approximation of the fiducial area of the surface array, and is illustrated in Fig. 4.3 (left). This specific selection area is used to estimate the performance of the full IceCube-Gen2 surface array, including the IceTop enhancement stations.
In order to minimize computation time as well as to achieve an even sampling, only showers distributed uniformly around the array border are simulated (indicated by green points in Fig. 4.3 (right)). For this purpose random points are sampled evenly around the array and are then used to specify the shower core position for the scintillator response simulations. For a minimal bias introduced by re-sampling the same shower with different core position, each shower was only re-used 3 times to, in average, distribute each individual shower only once within the Gen2 surface area.

In order to compare different station designs, the trigger efficiency is derived. The trigger efficiency is defined as the fraction of detected events within a certain area to the total amount of generated events within this area. For the detection, in a single panel a trigger threshold of 0.5 MIP is assumed. For a simple air shower trigger at least 3 hits within the array are required in order to roughly reconstruct the shower geometry. A more realistic requirement in the context of air shower reconstruction are 5 triggered scintillator detectors (as discussed in more detail in chapter 5). It has to be noted that, for real measurements, the chance of random coincidence triggers might not be negligible. An according study, however, was not performed within the scope of this thesis as random hits are not included in the simulations. Nevertheless, in order to reduce a possible influence of such random coincidences, a detection requirement of 5 triggered scintillators is applied also for solely trigger studies.
Hence, in the following, 5-hit-coincidences are required to obtain the detection efficiency of the IceCube-Gen2 scintillator array. To estimate the according uncertainties, the 95 % Wilson confidence-intervals[9] [134, 135] are calculated. The resulting efficiency curves are modeled via error function fit to the data points (without inclusion of the Wilson interval) in order to obtain

[9]The Wilson score-interval approximates the uncertainty of a binomial distributed observable resulting in an asymmetric confidence interval.

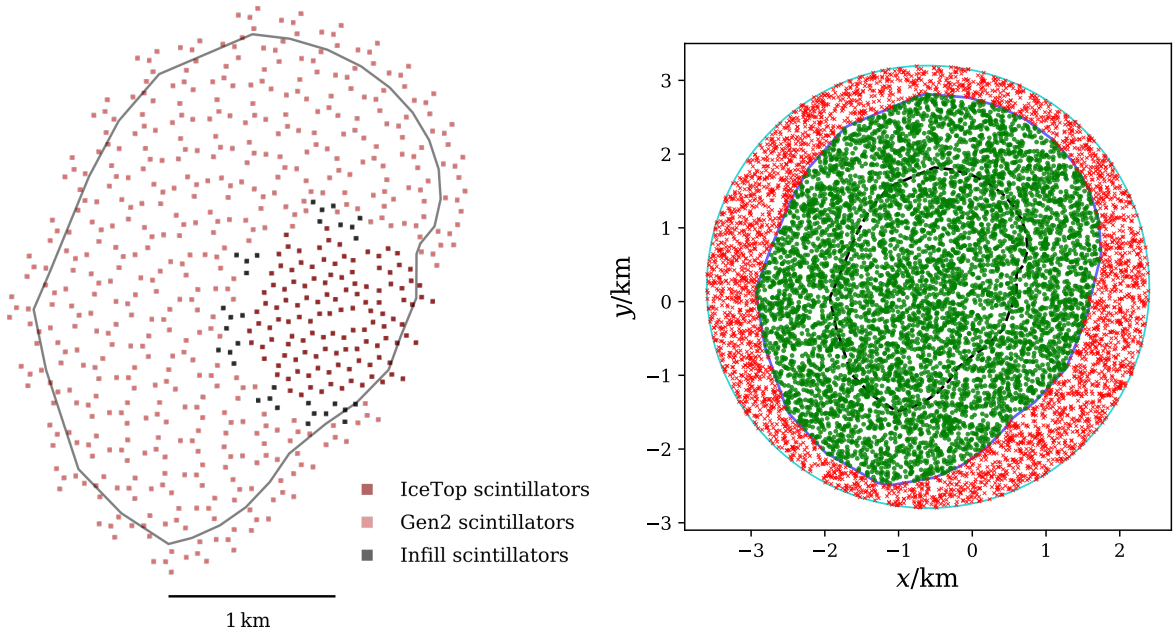

Figure 4.3.: Left: Layout of the IceCube-Gen2 scintillator array with all 162 stations. The gray contour line indicates the approximate fiducial area used for the analysis. Right: Random points are sampled within a circle with 3 km radius (cyan contour line) imbedding the IceCube-Gen2 surface array (dashed black contour line). Only points distributed uniformly up to 1 km outside of the surface array (blue contour line) are selected and taken as core position for the scintillator array response simulations (indicated as green points). Red crosses are not simulated in order to minimize the computation time.

the 98 % threshold, which is taken as full efficiency threshold for a given trigger condition.

Baseline design

Firstly, the detection efficiency of the current baseline design is investigated. The previous tuning of the station orientations provides a fairly uniform distribution of scintillation detectors across the array. The according efficiency curves are shown in Fig. 4.4. In fact, this layout design provides a rather low trigger threshold of below 500 TeV for proton initiated showers up to 45° zenith angle and a trigger condition of 5-coincidence requirement. As rather vertical proton showers are most crucial for the hadronic interaction science case (as discussed in more detail in section 5.4) the baseline design already provides an adequate detection threshold.

Number of panels per station

In order to determine, how many scintillation panels per station are required in order to obtain a threshold of ∼500 TeV, a benchmark was performed by reducing the amount of scintillation detectors to 4 per station by considering only one panel from each pair.
The resulting trigger efficiency compared to the baseline design is shown in Fig. 4.4. Due to the loss of active detection area, the threshold for rather vertical proton showers already shifts to 1 PeV. Such a high detection threshold, however, is insufficient particularly for the study of the transition of conventional to prompt muons (as further discussed in section 5.4). Moreover, in

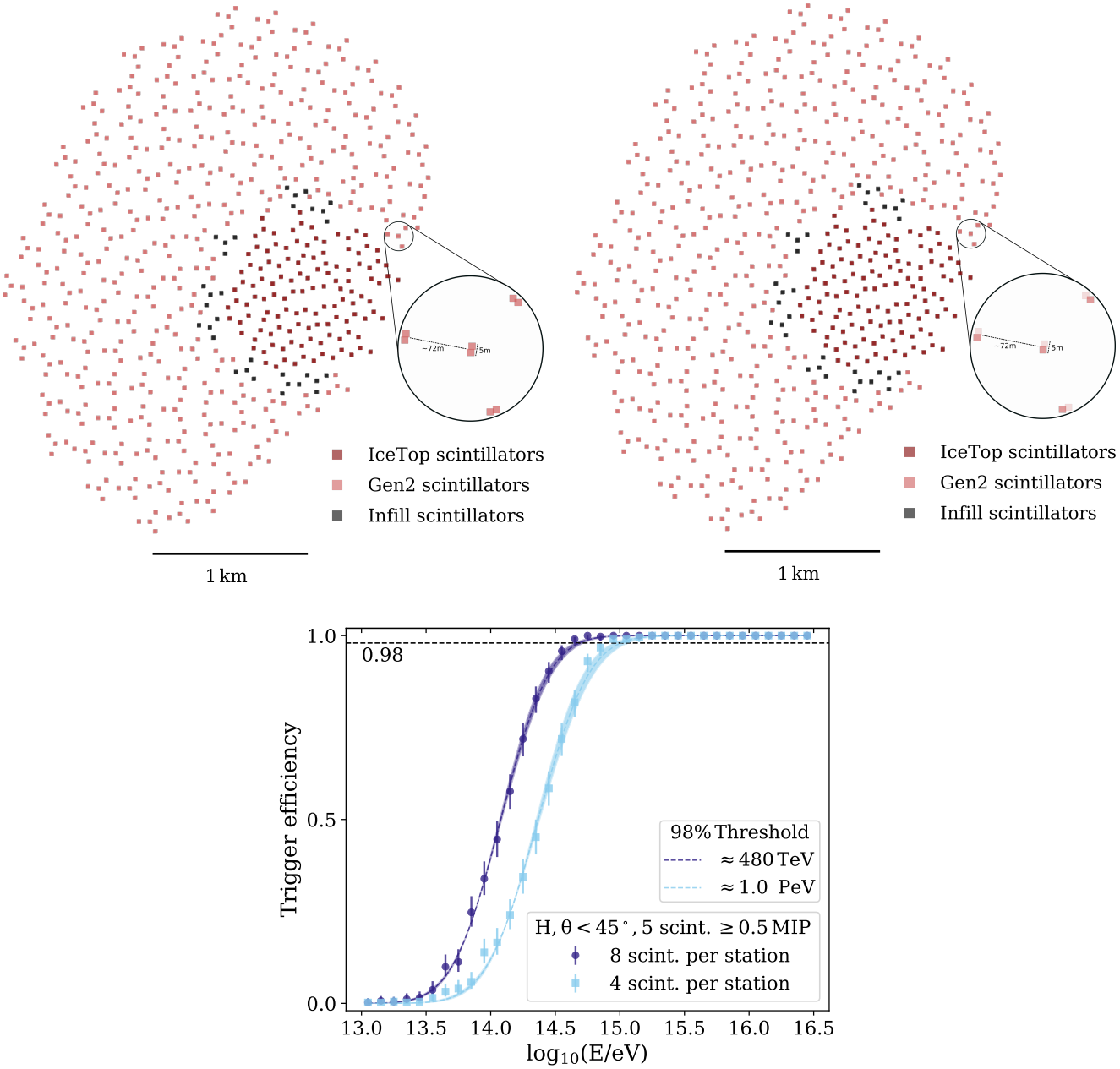

Figure 4.4.: Upper part: Layout of the baseline design of the IceCube-Gen2 scintillator array (left) and the descoping option with only four scintillators per station (right). Lower part: Comparison of the trigger efficiency of the baseline design and the descoping scenario for a 5-hit-coincidence. The errorband illustrates the 3σ confidence level of the error function fit. Included are proton primaries with up to 45° zenith angle.

the context of veto capabilities a lower threshold is generally preferable.
It has to be noted, however, that a less radical descoping option might still lead to sufficient performance and may be investigated in more detail in future studies. A more realistic possibility might be the reduction of the number of infill stations.

Possible station adjustments

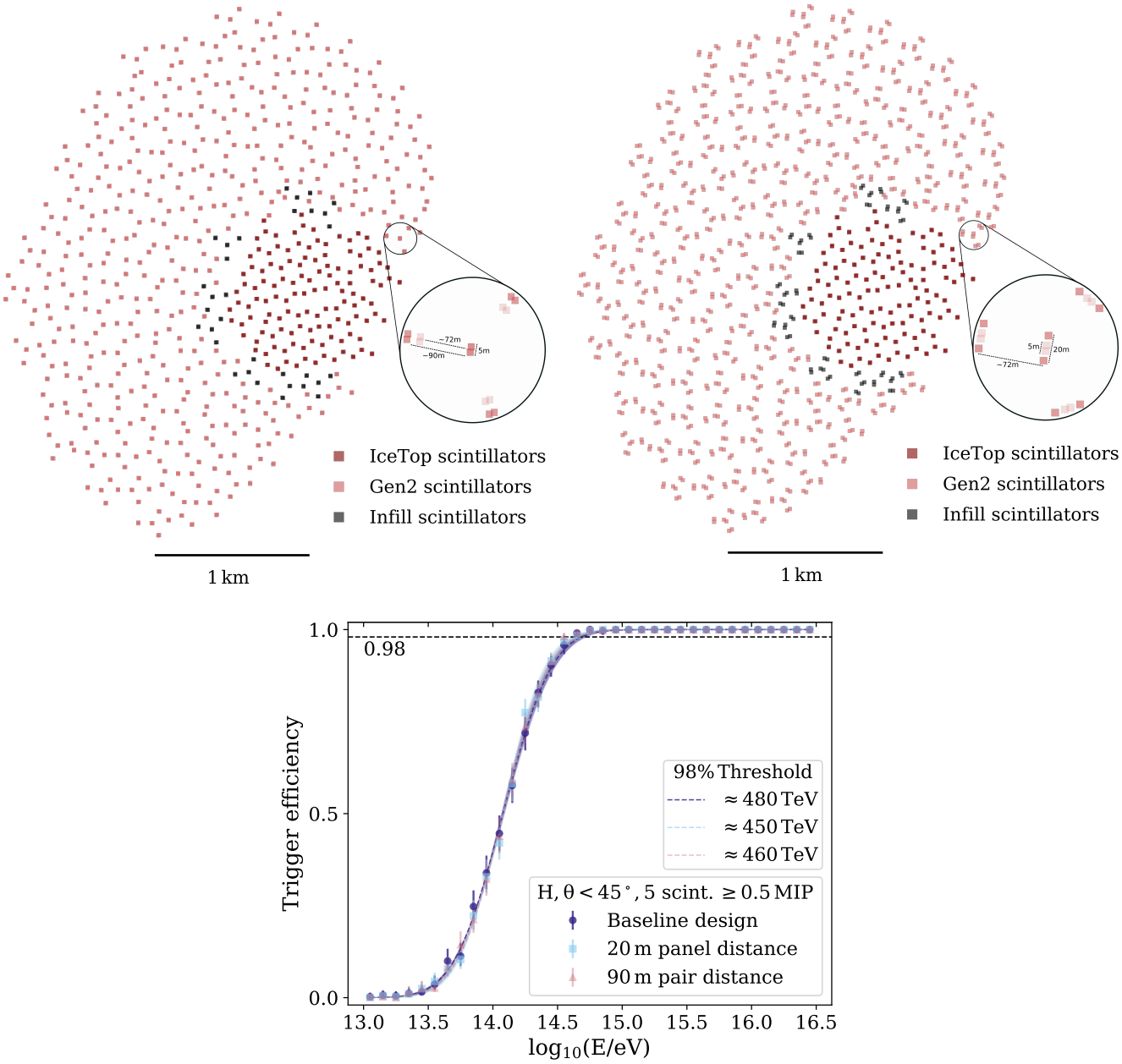

Figure 4.5.: Upper part: Layout of the IceCube-Gen2 scintillator array with increased distance between scintillator pairs in each station (left) and scintillators in each pair (right). Lower part: Trigger efficiency for increased distances between scintillator pairs in each station and scintillators in each pair compared to the baseline design for a 5-hit-coincidence. Included are proton primaries with up to 45° zenith angle.

Since the stations for the baseline design are the same as for the enhancement array, it is not clear if adjustments to this station design might deliver improved performance. In order to examine possible improvements of the initial design for the larger IceCube-Gen2 surface array two adjustments are tested. Firstly, the distance of the scintillator pairs in each station is increased from the initial $\approx 72\,\mathrm{m}$ to $\approx 90\,\mathrm{m}$. Secondly, the distance between the scintillators of each pair (5 m in the baseline design) is increased to 20 m. The layouts for both adjustments

are illustrated in Fig. 4.5. In fact, both options[10] do not provide significant differences in detection efficiency for all considered air showers (see Fig. 4.5). Hence, taking into account deployment efforts connected to increased distances within the stations, the baseline design remains unchanged.

Zenith dependence of the detection efficiency

The array response library used for the previous analysis does not contain more inclined showers above 50°. Therefore a second simulation set is produced to investigate the evolution of the trigger efficiency with increasing primary zenith angle. The array response for both proton and iron initiated air showers was simulated for energies between $\log_{10}(E/\mathrm{eV}) = 13 - 16.5$ and zenith angles up to 63° (for zenith angles up to 51° the array response is simulated up to $\log_{10}(E/\mathrm{eV}) = 17.0$). The full simulation set is shown in Tab. A.3. Each shower is injected 5 times onto the array within a radius of 1.5 km from the center of the IceCube-Gen2 surface array. The shower core selection area used for the analysis is similar to the previous efficiency studies.
The resulting efficiency curves for a requirement of 5 triggered scintillation detectors are shown in Fig. 4.6. For vertical showers with zenith angles below 27° a low threshold of $\leq 500\,\mathrm{TeV}$ is provided for both proton and iron primaries. However, with increasing inclination, the effective area of the scintillator panels decreases, resulting in a significant increase in detection threshold up to a few PeV. Since the slant depth is proportional to $\sec\theta$ (with θ denoting the primary zenith angle), the detection efficiency drops rapidly for inclined showers. Moreover, for rather vertical showers the detection efficiency for proton induced air showers is clearly higher compared to iron. The behavior of the detection efficiency can in principle be explained by two predominant effects. On the one hand, proton initiated air showers on average interact later in the atmosphere which causes the shower maximum to be closer to the ground, and therefore lead to a larger number of secondary particles at the observation level. On the other hand, the scintillation detectors are primarily sensitive to the electromagnetic shower component, which is strongly attenuated for increasing inclination. The latter is likely responsible for the slightly lower detection threshold for iron primaries for the most inclined bin, since the muonic component, which is larger for iron showers, is only subject to comparably small attenuation with increasing slant depth.

The simulation library used for the investigation of the zenith dependence is compiled with significantly larger statistics and therefore represents the standard set of simulations for all further analysis performed within this thesis.

4.3. Spatial and temporal distributions

For further analysis and in particular in the context of air-shower reconstruction, a deeper understanding of the characteristics of the spatial and temporal distributions detected with the array is crucial. In general, the characteristics imprinted by the cosmic-ray primary lead to a different longitudinal and lateral shower development. The longitudinal development is dictated by the momentum of the primary particle. Thus, the shower propagates longitudinally along the according incident direction. During this propagation various scattering processes can occur,

[10] Within the scope of this thesis also intermediate distances of 10 m and 15 m between scintillators of each pair as well as ≈ 81 m between the scintillator pairs in each station have been tested. However, these options also did not provide a significant change in the detection threshold.

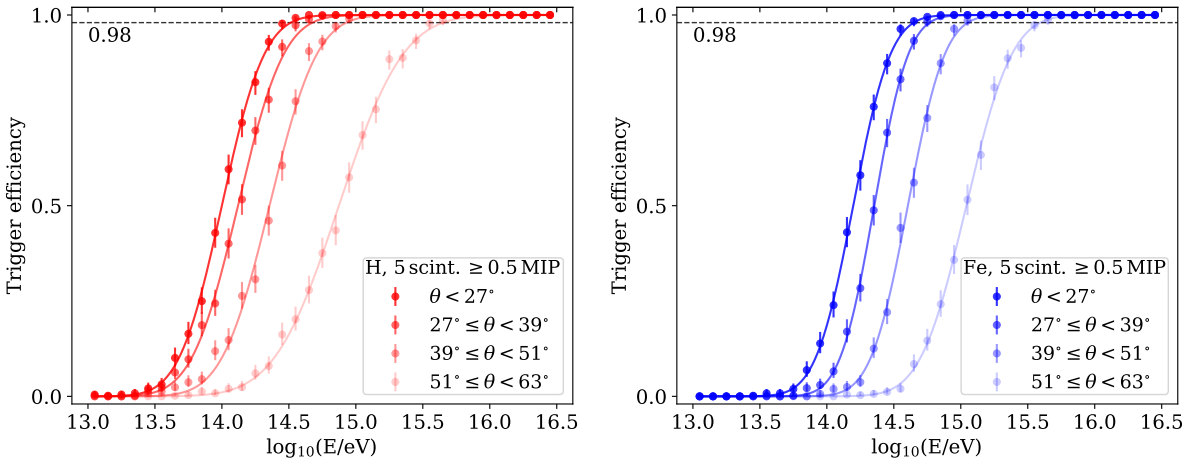

Figure 4.6.: Trigger efficiency for the baseline design (Fig. 4.4 (upper left)) of the IceCube-Gen2 scintillator array for proton- (left) and iron- (right) primaries shown for a 5-hit-coincidence and 4 different zenith bins.

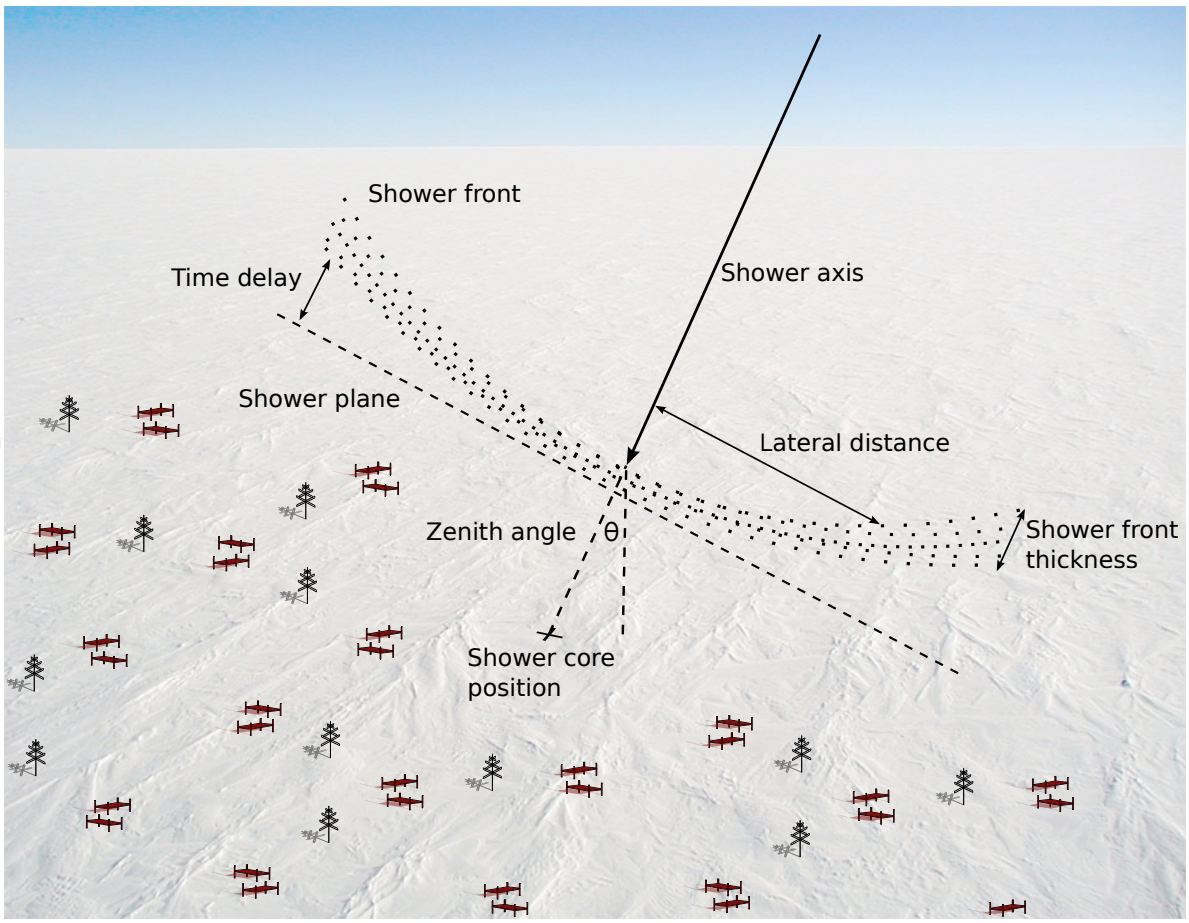

Figure 4.7.: Schematic plot of the shower geometry. The shower developes longitudinally along the shower axis. Various interaction processes lead to a lateral spread and a time dispersion manifesting in a curved shower front with finite thickness. Plot inspired by [136].

leading to additional transverse particle momenta. The lateral spread is mainly caused by the combination of the transverse momenta imprinted on the according secondary particles by the hadronic interactions as well as Coulomb scattering processes of the electromagnetic component [61]. Consequently, the particle trajectories feature different path lengths. In combination with the energy losses due to the numerous scattering processes, a time dispersion arises with respect to the distance from the shower axis, leading to a curved particle disc propagating along the shower axis [61] (as illustrated in Fig. 4.7). This particle disc is referred to as shower front. Hence, in measurements at the ground level, a lateral spread around the shower core[11] as well as an increasing time delay of signals with increasing distance from the shower axis can be observed. The distance from the shower axis will be further referred to as lateral distance.

Lateral distribution of particle content

A general feature with respect to the increasing lateral distance is the rapid decrease in particle density. This general behavior is similar for the electromagnetic, muonic and hadronic components. However, the relative contributions of different particle types differ fairly significantly [61].
By studies of CORSIKA simulations, it becomes visible that the overall lateral signal density is dominated by photons [3]. Towards larger lateral distances the muonic part becomes more relevant. Aside from the pure particle content of a particular air-shower, the array specific response has to be taken into account. Despite photons dominating the particle density, the actual footprint measured with the scintillator array is in fact mainly driven by the electron density, as the scintillator panels are most sensitive to electrons [3]. For large lateral distances and increasing inclinations the influence of the muonic component becomes larger. This instance can then be used for muon specific studies.

Since the overall shower development is based on the primary characteristics, important information about the nature of the cosmic-ray particle can be extracted from the spatial and temporal distributions observed at the ground. For this purpose, it is crucial to find the most suitable parametrizations of the according distributions.

4.3.1. Lateral distribution function

The model function for the signal distribution is generally referred to as LDF (Lateral Distribution Function) and describes the particle density as function of lateral distance. In principal, a proper choice of an LDF depends on the array characteristics and therefore varies throughout different experiments [61]. In fact, an analytical approach performed by Nishimura, Kamata and Greisen led to an approximate parametrization of the electron density distribution [137, 138] (NKG function). However, in some cases simpler parametrizations are already satisfactory [61]. Additionally, detector arrays which are more sensitive to a different shower component most likely require a different model function, e.g., in the case of a lateral distribution mainly driven by the muonic part, an LDF suited for the rather flat muon distribution.

Independent of the exact LDF form the parameters of interest are the shower size, usually correlated to a linear coefficient in the LDF, and the LDF slope. While the shower size is used to estimate the primary energy, the LDF slope is correlated to the shower age [139] since showers

[11] The shower core denotes the position of the impact point of a particular shower. It therefore is given by the intersection of the plane defined by the detector array and the shower axis.

in an earlier stage exhibit steeper lateral distributions [61]. It has to be noted, however, that the LDF shape, represented by the slope, is a function of primary zenith angle, energy and mass. The latter is caused by the connection of primary mass to the height of the first interaction and therefore the shower age [139]. Indeed, this dependence can be utilized to infer the primary mass (as discussed in chapter 6).

In order to derive a suitable model function for the signal distribution three different LDFs have been investigated regarding fit performance. Since the scintillation detectors are most sensitive to electrons, the chosen LDFs generally aim to properly describe the electron density (as further discussed in this chapter, this quantity is not measured directly but approximated due to inclusion of silent detectors in the fit procedure).

DLP function

The double logarithmic parabola (DLP function) is a phenomenological function which was found to be suitable for both the lateral distribution seen by the IceTop tanks [10] and the scintillators of the IceTop enhancement [3]. The function

$$S_{\mathrm{DLP}} = S_{\mathrm{ref}} \left(\frac{r}{R_{\mathrm{ref}}} \right)^{-\beta - \kappa \log_{10}\left(\frac{r}{R_{\mathrm{ref}}}\right)} \tag{4.1}$$

describes a parabola in logarithmic space ($\log_{10}(S/\,\mathrm{MIP})$). Since in particular the rather flat behavior of the IceTop tank signal distribution, likely caused by the rather large muonic contribution to the IceTop signals at large lateral distances [10], can be well described by this function, it is already used in the IceTop analysis. Therefore it might be a suitable choice for the Gen2 surface array which enables the measurement of the muonic tail by its sheer size. Additionally, the DLP function was found to be suitable for the scintillator array of the IceTop enhancement [5].
Compared to other LDFs this function has a rather simple form, which can result in increased fit stability. The S_{ref} parameter is connected to the shower size and denotes the signal strength at a certain reference lateral distance R_{ref}, and is therefore referred to as reference signal. The exponential parameters β and κ describe the slope of the function and the curvature of the parabola, respectively. As discussed, the LDF slope can be connected to the shower age.
When performing an LDF fit with the DLP function, one constraint on the parameter space of β and/or κ is given by the requirement of a monotonic decreasing behavior[12].

Linsley function

The Linsley function was introduced by John Linsley [140] and describes a modified form of the NKG function:

$$S_{\mathrm{Linsley}} = \frac{N}{2\pi R_{\mathrm{m}}^2 B(2-\alpha, \eta - 2)} \left(\frac{r}{R_{\mathrm{m}}} \right)^{-\alpha} \left(1 + \frac{r}{R_{\mathrm{m}}} \right)^{\alpha - \eta}. \tag{4.2}$$

This function features two slope related parameters α and η. As for the NKG function R_{m} denotes the Molière radius[13]. The parameter N is correlated to the shower size.

[12] Certain values of β for a given κ value can cause a kink at small lateral distances.

[13] The Molier radius describes the radius at which an electromagnetic shower is fully contained within a cylinder with the same axis as the shower axis [141]. In this context fully contained implies an energy containment of 90 %. In general the Molier radius is material specific and therefore for air showers depends on the observation location and altitude. For IceCube at the South Pole this translates to $R_{\mathrm{m}} = 128\,\mathrm{m}$ [3].

In contrast to the DLP function the Linsley LDF is normalized in terms of the Euler beta function B. Since the beta function is comprised of gamma functions this normalization introduces mathematical constraints on the slope parameters, namely $\alpha < 2$ and $\eta > 2$.

HG function

The hypergeometric Gaussian (HG) formalism was introduced in order to reduce difficulties of the NKG function and Euler beta functions in general with regard to the distributions observed at large air shower arrays [142]:

$$\begin{aligned} S_{\mathrm{HG}} &= \frac{N}{R^2} C(s)^{-1} \left(\frac{r}{R}\right)^{s-\alpha} \left(1+\frac{r}{R}\right)^{s-\beta} \left(1+d\frac{r}{R_{\mathrm{m}}}\right)^{-\delta}, \\ C(s) &= 2\pi F_{\mathrm{HG}}(\delta, s-\alpha+2, \delta+\beta-s, 1-d) B(s+2-\alpha, \delta+\beta-2s-2+\alpha), \\ F_{\mathrm{HG}}(a,b,c;z) &= \sum_{n=0}^{\infty} \frac{\Gamma(a+n)\Gamma(b+n)\Gamma(c)z^k}{\Gamma(a)\Gamma(b)\Gamma(c+n)n!}. \end{aligned} \tag{4.3}$$

The parameter R denotes a general scaling radius. Additionally, this function features 4 slope related parameters α, β, δ and s. It is important to note that the HG function is reduced to the NKG formalism for $\delta = d = 0$.
Due to the normalization in terms of the hypergeometric series F_{HG} the different slope parameters are mathematically constraint via

$$\begin{aligned} s - \alpha + 2 &> 0, \\ \delta - 2s + \beta - 2 + \alpha &> 0, \\ |1-d| &< 0. \end{aligned} \tag{4.4}$$

Based on the fairly complex form of this LDF, a higher flexibility can be provided [142]. However, the complex parameter space can reduce the fit stability.

Applicability

In order to test the general applicability of the different LDFs for the lateral distribution observed in simulations of the Gen2 scintillator array, average signal distributions as well as single events are studied (see Fig. 4.8).
Detectors without a signal (silent detectors) are included into the calculation of the average signal distribution to obtain a signal density. The resulting average distribution for proton and iron primaries with zenith angles below 30° is shown in Fig. 4.8 (left).

Regarding the average shape of the signal distribution no significant difference can be observed, leading to the conclusion of a general suitability of the 3 LDFs. An interesting feature visible in the average distribution is the intersection of the proton and iron distributions. In principle, such a feature can be useful for a mass independent determination of the primary energy. A difficulty, however, arises from the energy dependence of this crossing point, as already shown for the IceTop enhancement array [3].

Since shower fluctuations are effectively mitigated through the averaging, it is important to test the model function for single air showers. For this purpose, LDF fits of single events are performed with a similar signal log-likelihood minimization as in the reconstruction (see

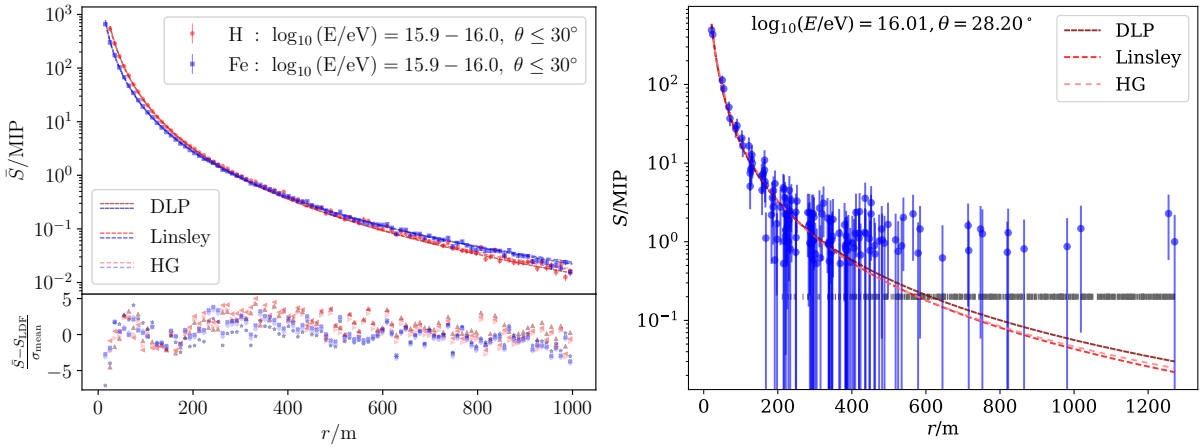

Figure 4.8.: Left: Average signal density for proton and iron primaries with energies between $10^{15.9} - 10^{16.0}$ eV and up to 30° zenith angle. The 3 different LDF fits are indicated with dashed lines. The lower panel illustrates the residuals for the according model functions. Right: Example of a single shower fit with the 3 LDFs (indicated as dashed lines). Blue points mark the MC data, with error bars given by the signal spread parametrization derived in section 4.3.3, calculated with the simulated signal. Gray bars indicate the positions of the silent detectors. The shower was initiated by a proton primary with ≈ 10 PeV energy and ≈ 28° zenith angle.

section 5.1). The influence of the silent detectors is directly incorporated into the likelihood function.
In fact, a study of the fit performance on a single-event basis reveals the predicted differences (see Fig. 4.8 (right)). On the one hand, by investigation of individual air shower events the DLP function was found to provide the highest fit stability, likely caused by its rather simple functional form. On the other hand, the HG function is generally more flexible and leads to a better description of the tail of the distribution, however, at the expense of fit stability.

Parameter optimization

In order to optimize the accuracy of an LDF fit, the according parameters have to be chosen carefully. For this reason a global parameter optimization via χ^2 minimization is performed.
Since the DLP function was found to provide a good overall performance with regard to the air shower reconstruction, likely due to the high fit stability, only the parameter optimization procedure for this particular LDF is shown. Since in general the lateral distribution varies as function of primary zenith angle and energy an according parametrization of a slope related parameter might enhance the performance of the other tested LDFs and can be part of future studies.

The optimization is performed with the full scintillator array response simulation set for proton and iron showers for primary zenith angles up to 45°. However, in order to guarantee a stable fit, only showers with at least 40 triggered detectors are included. Additionally, the core position is required to be within a 600 m radius from the center of the Gen2 surface array. The core position selection is used to maximize the containment of the showers within the array.
For every selected shower, an LDF fit with the DLP function is performed by variation of the parameters S_{ref} and β. The reference radius R_{ref} as well as κ are fixed. A proper choice of R_{ref}, however, is derived with a different approach in section 5.2. In order to determine an optimal choice of κ LDF fits for all selected showers are performed for different κ values. For each κ the

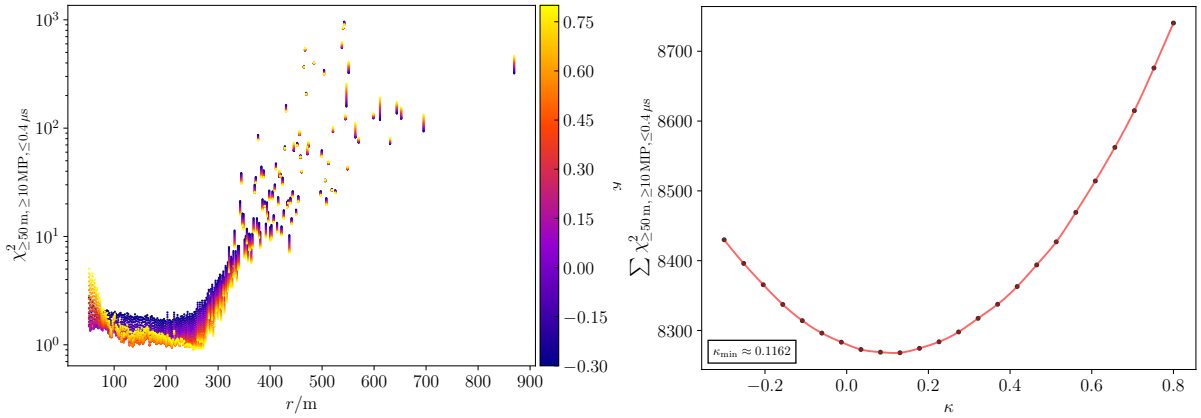

Figure 4.9.: Left: Average χ^2 distribution (obtained from LDF fits with the DLP function) as function of lateral distance, scanned for different κ values. Right: Sum over average χ^2 values for different values of κ. The minimum is determined via spline interpolation.

average χ^2 values are calculated as a function of lateral distance (see Fig. 4.9 (left)) via

$$\overline{\chi^2(r)} = \frac{1}{N} \sum_i^N \left(\frac{S(r_i) - S_{\mathrm{LDF}}(r_i)}{\sigma_i} \right)^2 . \tag{4.5}$$

with the signal spread σ_i (derived in the next section).
The χ^2 values, however, are only calculated for lateral distances above 50 m and only for signals with at least 10 MIP charge deposition. The latter is used in order to mitigate the influence of the tail of each distribution. Since the silent detectors are included into the likelihood function the LDF is undershooting the signal distribution for large lateral distances, hence, fluctuations are only observed in one direction. A value of 10 MIP is chosen to only take into account signals in the full trigger efficiency region (see Fig. 5.2). However, slightly delayed hits with high charge depositions above 10 MIP can occur also for larger lateral distances, likely due to neutrons, protons or muons which do not follow the general shape of the distribution. Thus, additionally, a maximum time delay of 0.4 µs is required. The cut on small lateral distances is used in order to neglect large χ^2 values introduced by the large signal values in the region close to the shower axis as well as saturated hits.

The χ^2 distribution for different κ values exhibits clear features for both small and large lateral distances (see Fig. 4.9 (left)). On the one hand, as mentioned, large χ^2 values close to the shower axis arise from the logarithmic behavior of the signal distribution. At around 70 m, however, a distinct narrowing of the χ^2 values occurs. This roughly corresponds to the distance between scintillator pairs within a surface station and is therefore likely due to the large probability to sample this distance.
On the other hand, because of the large influence of silent detectors on the LDF fit at large lateral distances a general increase in the χ^2 distribution above $\sim$ 300 m lateral distance is observed. A study on the energy dependence of the χ^2 distributions shows a shift of this behavior towards smaller and larger lateral distances for lower and higher energy showers, respectively. This is expected, since for smaller showers, i.e., lower primary energies, the silent detectors have a large impact on the LDF fit already for smaller lateral distances.

For the global optimization the sum over all χ^2 values is minimized (see Fig. 4.9 (right)). This procedure results in the best value for kappa of $\approx$0.12, which is used in further analysis.

4.3.2. Shower front function

Similar to the LDF optimization, a suitable model function for the time distribution is necessary in order to extract information about the primary cosmic ray, specifically its incident direction (primary direction). For this purpose, 3 different model functions have been tested on an event-by-event basis:

$$\Delta t(r) = n\left(e^{-r^2/s^2} - 1\right) + ar^2 \qquad \text{(Gaussian modified)}, \tag{4.6}$$

$$\Delta t(r) = ar^2 + b \qquad \text{(Parabola)}, \tag{4.7}$$

$$\Delta t(r) = a\left(1 + \frac{r}{b}\right)^c \qquad \text{(Linsley-like)}. \tag{4.8}$$

$\Delta t(r)$ describes the time delay with respect to a plane front assumption as function of lateral distance (as illustrated in Fig. 4.7).

For larger distances, the flatness of the time distribution is better described by the 'Linsley-like' function shown in Eq. (4.8). Both the pure and Gaussian modified parabolic functions provide a proper description of the arrival time distribution for small lateral distances. However, the Gaussian part features a distinct kink for small lateral distances which is not observed with the scintillator array. Moreover, a direct comparison of the overall reconstruction performance for the different model functions leads to a preference of the simple parabolic function Eq. (4.7). This is likely caused by the fact that the region close to the core with the highest particle density is most sensitive to the incident direction. Hence, a simple parabolic model function is used in the reconstruction procedure.

All functions were optimized via parameter scans based on a similar time log-likelihood minimization as used in the reconstruction. In Fig. 4.11 the results for Eq. (4.7) are shown. In general, all three functions exhibit similar features in the χ^2 distribution. At small lateral distances the χ^2 values increase due to the time spread parametrization. Thus, for the χ^2 calculation a lower lateral distance cut of 10 m is applied. Above around 240 m a narrowing in the distribution can be observed, which roughly corresponds to the spacing of the stations. At large lateral distances the χ^2 values decrease. However, since in this region fluctuations dominate and a proper fit close to the shower axis is most relevant for a precise direction reconstruction, only χ^2 values up to 600 m lateral distance are included. An optimal choice of the according parameter is obtained via minimization of the overall χ^2 sum, as shown in Fig. 4.11 (right). The simple parabola with $b = 10.1$ is therefore used as function for the shower front in the further analysis.

4.3.3. Fluctuations of array response

An important information in the context of signal and time distributions is the spread around the according expectation value. Parametrizations of these quantities were implicitly included in the parameter optimizations as they are incorporated into the signal and time likelihood functions. In this section the origin of the signal and time spread as well as their parametrization is discussed.

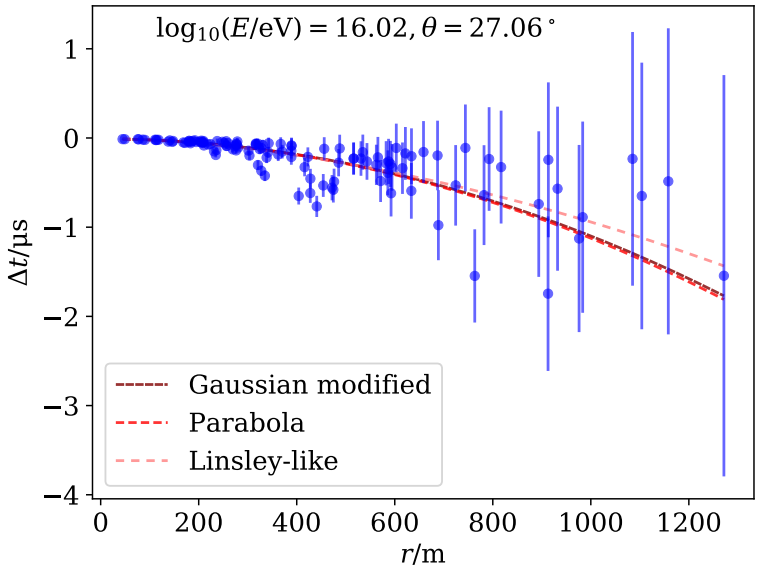

Figure 4.10.: Example of a shower front fit with all considered functions. The shower was initiated by a proton primary with energy of roughly 10.5 PeV. The error bars are given by the time spread parametrization derived in this chapter.

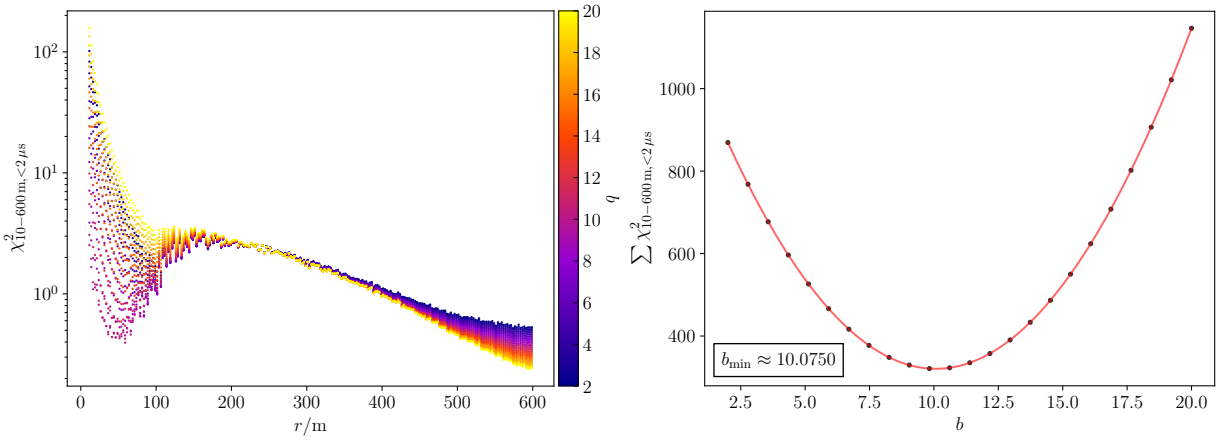

Figure 4.11.: Left: Average χ^2 distribution for the parabolic function over lateral distance scanned for different values of b. Right: Sum over average χ^2 values as function of b resulting in a minimum value of ≈ 10.1

Signal spread

Due to the stochastic nature of the shower development, an air shower is subject to intrinsic fluctuations, causing a finite accuracy in the measured signal strength of any CR detector. Additionally, instrinsic detector fluctuations contribute to the spread of the charge around the expectation value. This effect is connected to calibration uncertainties and the stability of the detector. Thus, in the case of scintillation panels, the electronics response and light propagation within the detector are the main sources of intrinsic detector fluctuations. While being a function of measured signal strength, the signal spread also depends on the properties of the primary CR particle as well as the array geometry. Therefore, for the description of the signal spread, a

parametrization in dependence of the primary zenith angle[14] and the lateral distance is intended. A suitable description of the signal fluctations is relevant in the context of the reconstruction of physical parameters [144], in particular for an accurate energy reconstruction, as discussed in more detail in chapter 5.

The signal spread can be characterized by using the special design of the discussed detector stations, namely the direct vicinity of two scintillation detectors. The distance of 5 m between neighbouring scintillator panels can be utilized as double measurement at a similar lateral distance and, thus, of the same signal expectation value. A similar study was performed already for the Pierre Auger Observatory [144], the ice-Cherenkov tanks of the IceTop array [145], as well as for the scintillation detectors of the IceTop-enhancement [5]. The basic idea is the comparison of signals measured in neighboring scintillator panels in order to find an approximation of the signal spread of a single detector. A strong motivation for this approach is already given by the clear correlation between signals measured in the according panels (see Fig. 4.12). For this analysis, a requirement of 20 hit detectors is part of the event selection. Such a cut intrinsically shifts the energy threshold roughly to the region of full efficiency for the Gen2 scintillator array. Additionally, since the approximation of a point-like double measurement only holds for a restricted lateral distance range, only signals within $50 - 500$ m from the shower axis are taken into account. Inclusion of small lateral distances would lead to an overestimation of the signal fluctuations because of the large signal differences between two neighboring panels due to the logarithmic behavior of the lateral distribution. On the other hand, at large distances from the shower axis intrinsic shower fluctuations become very large, resulting in significant differences in the signal expectation value for both panels.

For the analysis of the signal differences the distribution in Fig. 4.12 is binned into slices along the diagonal line of one-to-one correlation. For a large set of air showers the signals measured in a single scintillator panel are expected to follow a Gaussian distribution. Hence, the signal differences of two panels lead to a convolution of two Gaussians which in turn is represented by a Gaussian distribution [146] around the expectation value $\langle S \rangle$. Based on the signal differences, the relative fluctuations of signals between two neighboring panels a,b can be defined [143]:

$$\Delta S_{\mathrm{rel}} = \frac{S_a - S_b}{\sqrt{2}} \,. \tag{4.9}$$

In order to extract the relative fluctuations for a single scintillator panel the distribution in each $\langle S \rangle$ bin can be described by a Gaussian model, with width corresponding to the according signal spread. The signal spread as a function of the signal expectation value is shown in Fig. 4.13 (left).
As expected, for an increase in average signal strength a rise in the signal spread can be observed. However, over two orders of magnitude in average signal, this increase encompasses only roughly one order of magnitude. This is in particluar important in the context of air shower reconstruction which takes into account the signal spread. Due to the behaviour of the signal spread, a smaller weight is applied to the on average smaller signals at large lateral distances. The fit therefore is driven by the fairly large signals and multiplicity close to the shower axis, which mostly originate from the electromagnetic component of the shower. Since, additionally, the primary energy is highly correlated to the electron size[15] and therefore to the electromag-

[14] The stronger attenuation of the electromagentic component for more inclined showers leads to a larger muon/em ratio [143]. Additionally, higher inclination leads to larger track lengths for HE muons, which in turn results in larger signals, hence, larger signal spread.

[15] Generally, the primary energy is correlated to the shower size, i.e., to the number of all particles [61]. The scintillation panels, however, are most sensitive to the electromagnetic part of the shower. As this part is the leading component it provides the largest contribution to the total shower size.

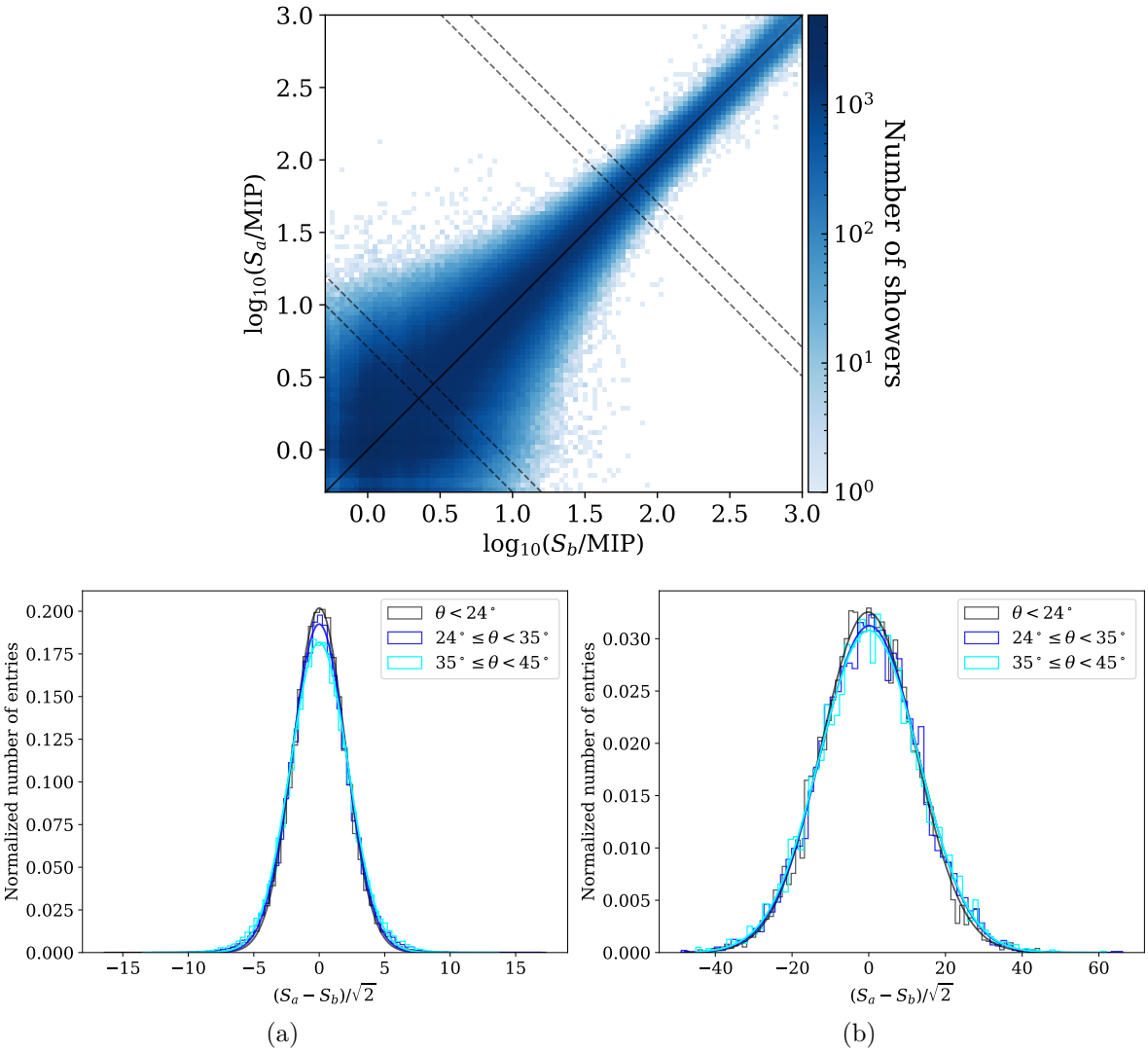

Figure 4.12.: Upper part: Distribution of signals in neighboring scintillators a, b for an equal proton/iron composition. Shown are all signals below the assumed saturation threshold of 1000 MIP. The solid black line indicates the one-to-one correlation. The two example bins shown in the lower plots are illustrated by the dashed black lines. Lower part: Example distributions of the difference between signals in neighboring scintillators, for a bin center of 3.9 MIP (a) and 89.5 MIP (b) and three different zenith bins. While the signal value increases by almost an order of magnitude, the signal spread increases by roughly a factor 5. Therefore, the detectors towards the center of the shower with larger signals contribute more strongly to the LDF. The Gaussian fit to the distribution is indicated with solid lines.

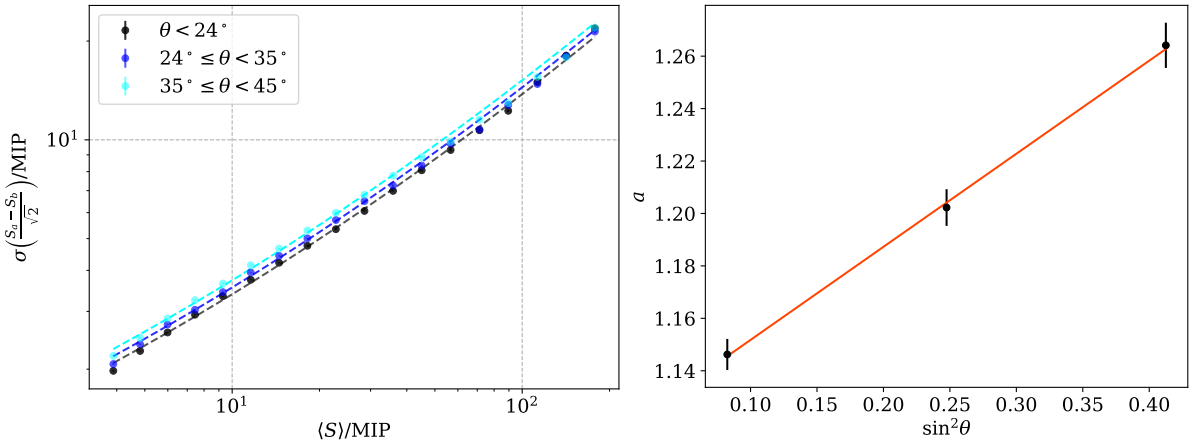

Figure 4.13.: Left: Signal spread parametrization for three different zenith bins. Right: Parametrization of the signal spread parameter a with $\sin^2\theta$. The linear fit to the parameter values for the 3 zenith bins is indicated as red line.

netic shower component the part close to the shower core is most crucial for the reconstruction. The signal spread parametrization is performed via

$$\begin{aligned} \sigma_S &= aS^{b\log_{10} S+c}, \\ a &= 0.36\sin^2\theta + 1.12, \\ b, c &= 0.07, 0.4. \end{aligned} \tag{4.10}$$

For the three analized zenith bins a linear parametrization of a with $\sin^2\theta$ is applied (see Fig. 4.13 (right)). Generally, considering only fluctuations based on the stochastic nature of the shower development, an accurate description of the signal fluctuations with a Poisson model is expected. However, likely due to further dependencies on the primary zenith angle as well as the array geometry, deviations from a pure Poisson distribution occur. In this context, the deviations from the pure Poisson behavior might be caused by the particle spread, as the energy deposit in the scintillator detectors changes with the incident particle direction.

When applying this method, certain restrictions have to be kept in mind. Based on the relative position of neighboring scintillator panels with regard to the geometry of a particular shower event, an overestimation of the signal fluctuations mainly for small lateral distances can occur [145]. This effect is caused by the fact that the assumption of a negligible distance between two adjacent panels is least valid if the two panels build one line with the shower axis. Additionally, the derived single detector fluctuations are driven by intrinsic shower fluctuations, since intrinsic detector fluctuations are not part of the detector response simulations. Thus, once availabe, this study should be performed with experimental data in order to include all influencing effects as well as to remove systematic effects introduced by a particular simulation model. Then, additionally, the mean of the distributions can be incorporated to account for possible biases due to differences in the electronic response.
In addition, in order to further account for possible corrections based on the lateral distance, an according parametrization can be applied in a future study. Moreover, a weighting with a cosmic-ray flux model can be applied as a first step towards a better understanding of the signal fluctuations expected for a real measurement.

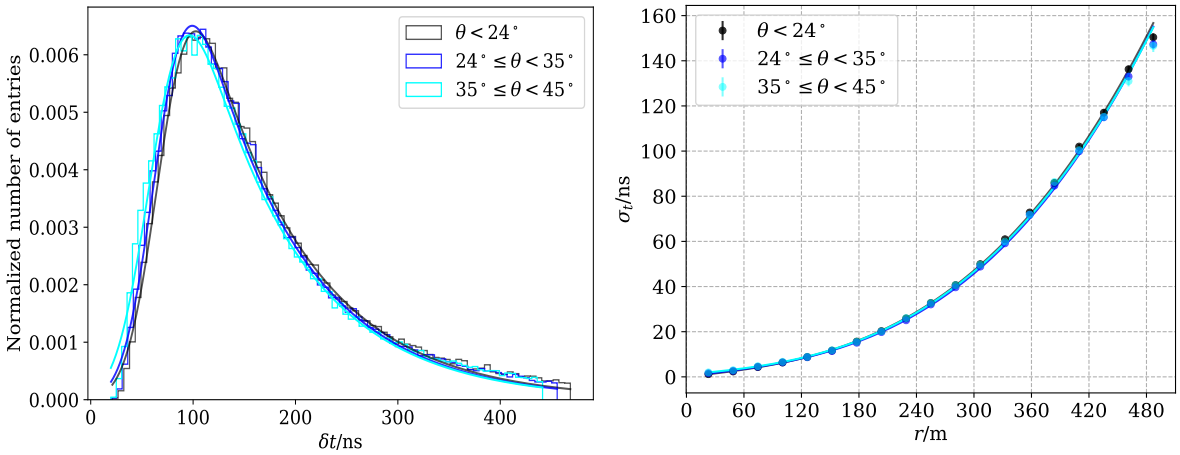

Figure 4.14.: Left: Example time delay distribution for an average lateral distance of $\sim 400\,\mathrm{m}$. The fits via exponentially modified Gaussian are indicated with solid lines. Right: Time spread as function of lateral distance for 3 different zenith bins.

Time spread

Similarly as for the signal strength also the distribution of pulse times is spread due to intrinsic shower as well as detector fluctuations. The width of the shower front is expected to increase with increasing distance to the shower axis mostly due to longer trajectories and large scattering angles of the particles, resulting in larger time delays and fluctuations [62]. In addition, in average, shower particles at large lateral distances are less relativistic, which increases the front thickness [61].
In contrast, close to the shower axis the shower front describes a very thin ($\mathcal{O}(ns)$ with respect to the plane front assumption) disc containing a high density of highly energetic particles. Consequently, the region close to the shower axis is of utmost importance for the determination of the angle of incidence of the primary particle.
Since the structure of the shower front is connected to the longitudinal development via the height of the first interaction, it contains important information about the primary mass [61]. Additionally, the time spread is an important input parameter for the determination of the primary direction through air shower reconstruction (see section 5.3). Hence, in order to derive a proper parametrization of the time spread, the radial dependence of time delays was studied for different ranges of the primary zenith angle.
For this purpose, showers are selected based on a similar multiplicity cut as for the signal spread parametrization, i.e. with a requirement of 20 triggered detectors. In contrast to the signal distribution, the time distribution does not feature a logarithmic behaviour. Hence, the lower cut on the lateral distance for the signal selection is lowered to 10 m. Moreover, only signals with $\Delta t \leq 2\,\mu\mathrm{s}$ are considered. Therefore a contamination due to very delayed particles within the comparatively small considered lateral distances is minimized.
The time delays for all selected showers are binned in lateral distance. Each bin can be described by an exponentially modified Gaussian distribution (see Fig. 4.14 (left)):

$$
\begin{aligned}
f_{\Delta t} &= \frac{a}{2} e^{\frac{a}{2}(2\mu + a\sigma^2 - 2\Delta t)} \mathrm{erfc}\left(\frac{\mu + \mathrm{a}\sigma^2 - \mathrm{t}}{\sigma\sqrt{2}}\right), \\
\mu_{\Delta t} &= \mu^2 + \frac{1}{a}, \; \sigma_{\Delta t} = \sigma^2 + \frac{1}{a^2}.
\end{aligned}
\tag{4.11}
$$

The standard deviation $\sigma_{\Delta t}$ of each distribution is taken as approximation of the time spread and is shown as function of lateral distance in Fig. 4.14 (right). The trend of a slight decrease in steepness with primary zenith angle can be observed. For increasing inclination, the shower maximum is reached higher in the atmosphere and the electromagnetic shower component is attenuated, resulting in a less steep shower front.

For each primary zenith bin, $\sigma_{\Delta t}$ is modeled with a 3rd degree polynomial. The parameters of the polynomial are further parametrized with $\sin^2\theta$.

It has to be noted that this approach does not account for a possible signal dependence of the time fluctuations. An according parametrization can be folded into a future study. Moreover, similar to the signal spread parametrization, the simulations used in this analysis can be weighted with a model describing the measured cosmic-ray flux. Additionally, similar to the signal spread parametrization, a comparison of time delays measured in neighboring scintillator panels can be utilized as alternative approach to study time fluctuations.

Chapter 5.

Reconstruction of air shower parameters

The reconstruction of shower parameters is based on the parametrizations for the measured signal and time distributions (see section 4.3.1). In the reconstruction analysis the observables of interest are the incident direction, given by the primary zenith and azimuth angles, the position of the shower core at the observation level and the primary energy and mass, which are correlated, among others, to the shower size and age, respectively. Generally, these parameters are reconstructed in an iterative procedure and are therefore not determined independently.

The software used for the reconstruction, the *RockBottom* project [147], provides a possibility to perform a hybrid reconstruction to fully benefit from all different detection channels. For the scintillation detectors, a full analysis chain was already developed for the IceTop enhancement array [5] and is incorporated in the *RockBottom* software. This analysis chain can similarly be applied for a larger scintillator array and is therefore used as a basis for the Gen2 surface array reconstructions.
In the following sections, the general reconstruction procedure as well as its optimization for the scintillator array of IceCube-Gen2 array are discussed. All presented reconstruction analyses use the full set of scintillator array response simulations produced for the studies of the zenith angle dependence of the detection efficiency and for the characterization of the spatial and temporal distributions shown in section 4.3. Hence, for both, proton and iron primaries, 100 individual showers[1] per zenith and energy bin are used, with a bin width of 0.1 in $\sin^2\theta$ and $\log_{10} E$, respectively. An overview over the simulation set can be found in Tab. A.3. The zenith range used for a particular analysis is stated in the according sections.

5.1. Reconstruction procedure

Starting point of the reconstruction procedure is the simulated detector response of the IceCube-Gen2 surface array for a particular air shower event. Negative log-likelihood minimizations are used in order to find proper parametrizations of the signal and time distributions. In principal, the likelihood functions can be used instead. However, due to increased numerical stability generally the logarithmic form is preferred.
An important input for the likelihood functions is the spread around the expectation values for

[1] Each individual shower is re-sampled 5 times within a radius of 1500 m from the center of the IceCube-Gen2 surface array.

signal and time (see section 4.3.3) and the trigger probability for the scintillation detectors. The reconstruction algorithm itself is a 3 dimensional procedure, reconstructing air shower events iteratively in 3 steps based on initial seeds derived from basic characteristics of a particular shower event.

Initial parameters

The initial parameters provide seeds for the likelihood function in the iterative minimization procedure. In order to increase the probability of the likelihood fit to converge, the seed values should be derived properly. Hence, basic shower characteristics are utilized for analytical calculations of the initial parameters.

Core position

By iteration over all measured signals S_i for a particular event, the weighted average (center of gravity (COG) for all S_i) is used as initial guess of the shower core location:

$$\vec{x}_{\mathrm{COG}} = \frac{\sum_i S_i \vec{x}_i}{\sum_i S_i} \,. \tag{5.1}$$

A weighting with the signal strength gives a higher importance to the detectors with large signals, which are distributed closely around the shower axis. It has to be noted that, in principle, the accuracy of this approach relies on the sampling of the air shower footprint, which can lead to inaccurate results for shower cores located outside of the array.

Primary direction

In order to find a first guess for the direction of the primary particle, $\vec{n}$, the shower front is approximated with a plane. The arrival direction can then be estimated by minimizing the χ^2 function for a shower front moving along the shower axis with the speed of light c:

$$\chi^2_{n_x,n_y,t_0} = \sum_i \frac{1}{\sigma_i^2} \left(t_i - t_0 + \frac{1}{c} \begin{pmatrix} n_x \\ n_y \end{pmatrix} \begin{pmatrix} x_i \\ y_i \end{pmatrix} \right)^2 , \tag{5.2}$$

with the signal times t_i, the core arrival time t_0, the neglection of the z-coordinate, i.e. assuming equal elevations of all detectors and a constant time spread $\sigma_i = \sigma = 5\,\mathrm{ns}$. This results in the three linear equations

$$\vec{\nabla} \chi^2_{n_x,n_y,t_0} = \vec{0} \,. \tag{5.3}$$

for n_x, n_y and t_0 that can be solved analytically by applying Cramer's rule[2].
If this procedure fails, a simple direction seed of $(0, 0)$ for zenith and azimuth angles is returned, since with this method, in some cases, a particular distribution of arrival times does not lead to a physical solution. However, this does not necessarily imply that the according event can not be successfully reconstructed in the iterative minimization procedure.
Generally, a simple plane assumption for the shower front is a reasonable approach considering

[2] Gives an explicit solution for the case of an arbitrary amount of linear equations with the same amount of unknowns [148].

the fact that the curvature in the region decisive for the direction reconstruction, namely the region close to the shower axis, is rather small. However, in particular for large showers with many particles at larger lateral distances the shower front curvature should be included in the reconstruction procedure. Hence, the parametrized front curvature as well as the front thickness are included into the main reconstruction algorithm.

Energy estimator

The initial guess on the cosmic ray energy estimator, which is a signal at a reference distance, can be deduced simply from the multiplicity of triggered detectors (detectors with a signal $\geq 0.5\,\mathrm{MIP}$). As the reference signal can vary over multiple orders of magnitude mostly based on the shower size, the according initial guess is increased over multiplicity ranges. These initial parameters as well as the information about all detectors of the array are then passed to the iterative minimization procedure.

Log-likelihood minimization

For the construction of the likelihood functions, the according underlying distributions have to be incorporated. In case of the signal distribution, this leads to different likelihood functions for different ranges of signal strengths. The main trigger region between 2-1000 MIP can be described by a Gaussian distribution. However, below roughly 2 MIP, where in principle single particles are counted, the likelihood function is based on a Gamma distribution. On the other hand, above 1000 MIP the scintillation detectors are assumed to reach saturation. This likelihood function for saturated detectors is modeled via an error function.
From a mathematical perspective the combination of the according likelihood functions describes the probability to observe a certain signal value for a given signal expectation value.

As discussed in section 4.3.1 the silent detectors are a crucial part of the LDF fit. To properly quantify the influence of these detectors, the hit probability is parametrized, i.e. the probability of a detector to be triggered above the trigger threshold of 0.5 MIP.
For this purpose the full set of reconstructions is analyzed, i.e., all successfully reconstructed showers. The criteria for a successful reconstruction are:

1. At least 5 hit detectors in order to provide enough sampling points to determine all reconstruction parameters.
2. Proper values for the parameters of the reconstructed LDF function, namely $\log_{10}(S_{\mathrm{ref}}/\,\mathrm{MIP}) \geq -2.5$ and $0.8 \leq \beta \leq 4.0$ in the case of the DLP function.

Since the parameter space of the LDF is highly dependent on the exact function used in the reconstruction procedure, the according ranges of parameter values have to be chosen individually for a particular LDF. For the DLP function these parameter cuts mostly affect events with low primary energy (see Fig. 5.1). The exact cut values are, for the most part, chosen empirically based on the according distributions of the reconstructed parameters. However, based on the functional form of the DLP function an additional mathematical constraint on the slope parameter β arises by requiring a monotonic decreasing behavior.

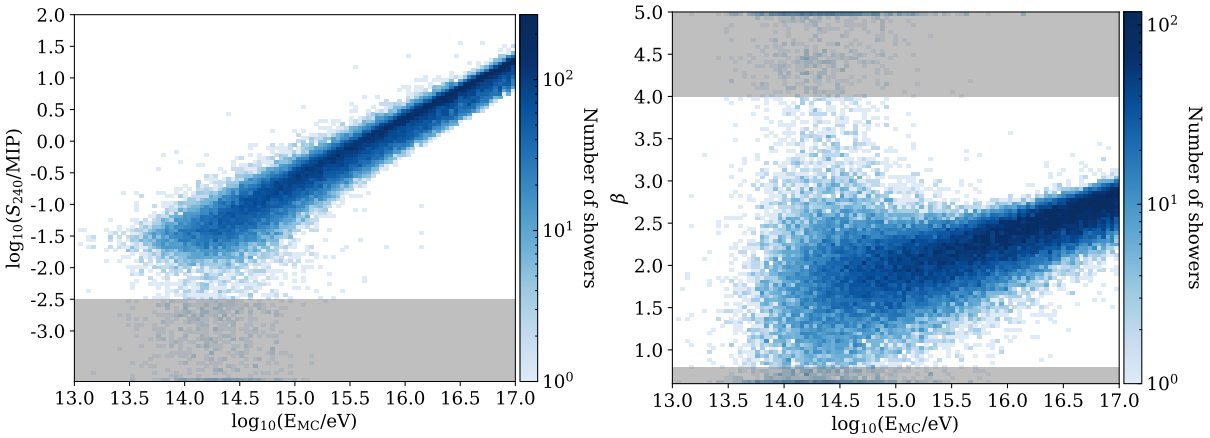

Figure 5.1.: Distributions of the energy estimator (S_{240} as energy proxy is derived in section 5.2) (left) and the slope parameter (right) for all reconstructed proton showers. The gray bands indicate the quality cuts on both parameters which represent one of the requirements for a successful reconstruction. For both parameters the cuts mostly effect events with low energy.

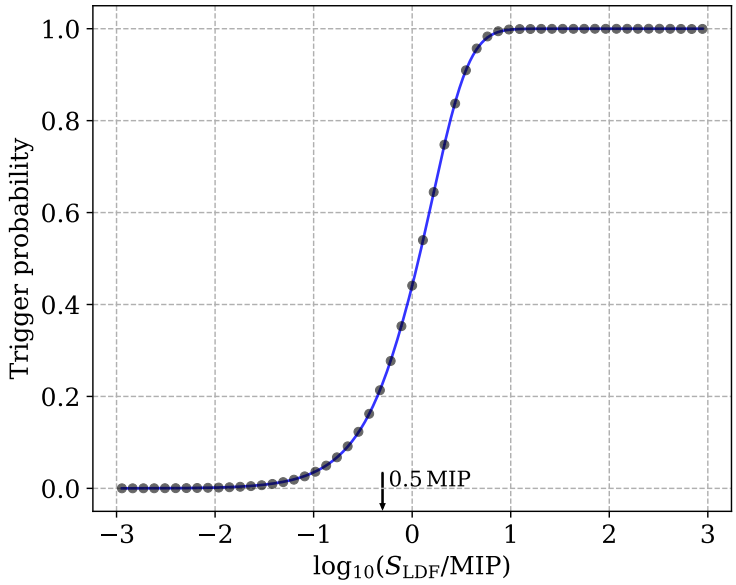

Figure 5.2.: Probability of a scintillation detector to be triggered for a given trigger threshold of 0.5 MIP (marked with a black arrow) as a function of a signal expected from the LDF fit (S_{LDF}). For the parametrization an equal proton/iron composition is used. Moreover, only showers up to 45° zenith angle and with true core position up to 100 m to the edge of the Gen2 surface array (see Fig. 4.3 (left)) are included.

For a given event, the reconstructed fit to the signal distribution gives the expected signal value as function of lateral distance. Further, signal expectations above and below the trigger threshold can be differentiated for each triggered and silent detector. This process can be applied for every selected reconstruction and binned in signal expectation value. The resulting probability curve is illustrated in Fig. 5.2, showing the fraction of triggered to all detectors as function of the logarithm of the signal expectation value. It should be noted that the value of the assumed assumed trigger threshold of 0.5 MIP is not at roughly 50% probability. However, this behavior needs further investigation. Moreover, a different LDF would likely cause a change in the trigger probability and should be part of future studies.

An appropriate model function for the trigger probability is given by a combination of a generalized logistic function and a modified error function:

$$P_{\text{hit}} = \frac{1}{\left(1 + qe^{-a \log_{10} S_{\text{LDF}}}\right)^{\frac{1}{\nu}}} \left[1 - a \left(1 + \operatorname{erf} \frac{b - \log_{10} S_{\text{LDF}}}{c_1}\right) \left(1 + \tanh \frac{b - \log_{10} S_{\text{LDF}}}{c_2}\right)\right] \quad (5.4)$$

For a proper treatment of the silent detectors, the resulting no-hit probability $P_{\text{nohit}} = 1 - P_{\text{hit}}$ is implemented in the log-likelihood function.
Once implemented, however, the parametrization of the hit probability will change for the next reconstruction run, since the approach is based on reconstructed values. By re-doing the parametrization multiple times, the probability curve can be stabilized. A proper parametrization of P_{hit} therefore is an iterative procedure and is part of the reconstruction optimization.

Finally, the log-likelihood functions for triggered, saturated and silent detectors $\ln \mathcal{L}_{tr}$, $\ln \mathcal{L}_{sa}$ and $\ln \mathcal{L}_{si}$, respectively, are combined to the overall signal log-likelihood function $\ln \mathcal{L}_S$ [5]:

$$\begin{aligned}
\ln \mathcal{L}_{tr} &= \begin{cases} -\sum_i \left[\frac{1}{2}\left(\frac{S_i - S_{\text{LDF}_\text{i}}}{\sigma_i}\right)^2 + \ln\left(\sqrt{2\pi}\sigma_i\right)\right] & \text{if } \mathrm{S}_i \geq 2\,\text{MIP}, \\ -\sum_i \left[S_{\text{LDF}_\text{i}} - S_i \ln\left(S_{\text{LDF}_\text{i}}\right) + \ln \Gamma(S_i + 1)\right] & \text{if } \mathrm{S}_i < 2\,\text{MIP}, \end{cases} \\
\ln \mathcal{L}_{sa} &= \sum_i \ln\left[\frac{1}{2} \operatorname{erfc}\left(\frac{S_{\max} - S_{\text{LDF}_\text{i}}}{\sqrt{2}\sigma_i}\right)\right], \\
\ln \mathcal{L}_{si} &= \sum_i \ln(1 - P_{\text{hit}}), \\
\ln \mathcal{L}_{\mathcal{S}} &= \ln \mathcal{L}_{tr} + \ln \mathcal{L}_{sa} + \ln \mathcal{L}_{si}\,.
\end{aligned} \quad (5.5)$$

S_i and S_{LDF_i} denote the measured signal in each detector and the according signal expectation value, respectively. The signal spread σ_i is given by the parametrization derived in section 4.3.3 and is calculated based on the signal expectation value.

In the log-likelihood function for the time fit a Gaussian distribution is assumed:

$$\begin{aligned}
\ln \mathcal{L}_t &= -\sum_i \sqrt{S_i} \left(\frac{(\Delta t_{i,\text{local}})^2}{2} + \ln \sqrt{2\pi}\sigma_{t_i}\right), \\
\Delta t_{i,\text{local}} &= \frac{t_i - t_{i,\text{front}}}{\sigma_{t_i}}\,,
\end{aligned} \quad (5.6)$$

where t_i denotes the measured time in each triggered detector with respect to the plane front assumption, $t_{i,\text{front}}$ is the time expectation value given by the model for the front curvature. Similar to the signal likelihood, the likelihood function for the time fit describes the distribution of the measured times around the expectation value. The width of the distribution is given by the time spread σ_{t_i}.
Additionally, a weighting $\sqrt{S_i}$ with the signal strength is applied, leading to a general improvement in angular resolution for large showers where many low energy particles appear at large lateral distances. Consequently, the shower front fit is driven by the region close to the shower axis, where the largest signals are expected.

In total, the signal and time model functions feature a set of 8 different parameters, $\vec{q}_S$ and $\vec{q}_t$, respectively, that are varied in order to minimize the negative log-likelihood. The LDF

$S_{\mathrm{LDF}} = S_{\mathrm{LDF}}(\vec{x}, \vec{q}_S) = S_{\mathrm{LDF}}(\vec{x}, \vec{x}_{\mathrm{core}}, S_{\mathrm{ref}}, \beta)$ is a function of the coordinates of the shower core at the ground $\vec{x}_{\mathrm{core}}$, the shower size S_{ref} and the shower shape, characterized by the slope parameter β. Additionally, since the direction is used in the calculation of the lateral distance, the LDF also depends on the zenith and azimuth angles. The parameters of the shower front function $t_{\mathrm{front}} = t_{\mathrm{front}}(\vec{x}, \vec{q}_t) = t_{\mathrm{front}}(\vec{x}, t_0, \theta, \phi, a)$ are the zenith and azimuth angles θ and ϕ, respectively, the shower core arrival time t_0 and a, which controls the parabolic shape of the function.
However, in the iterative minimization not all parameters are varied at once. The minimization procedure is comprised of 3 steps:

1. LDF fit with S_{ref}, β and $\vec{x}_{\mathrm{core}}$ as free parameters.
2. Combined fit of LDF and shower front function with S_{ref}, β, θ, ϕ, t_0 and a as free parameters. The core position $\vec{x}_{\mathrm{core}}$ is taken from the previous step.
3. LDF fit with S_{ref}, β and $\vec{x}_{\mathrm{core}}$ as free parameters.

In the second step a simultaneous fit of the signal and time distributions is performed by combination of the according log-likelihood functions. Each step features different settings for step size and boundaries of the different parameters, which can be tuned in order to increase reconstruction performance as well as the fit stability. For the minimization itself the MINUIT algorithm [149] with the SIMPLEX method is used.

In addition to the parameter settings specified in the reconstruction procedure, further cuts are applied to improve the reconstruction performance. The LDF fit for all showers is performed within a region of 10-1500 m in lateral distance. On the one hand, the DLP LDF is not defined at the core position. On the other hand, a cut on large lateral distances is justified by the fairly large shower fluctuations as well as the large influence of the silent detectors dominating far from the shower axis. It should be noted that the exact value of the upper cut on the lateral distance depends on the size of the observed showers and therefore on the primary energy and to some extent on the primary zenith angle. Thus, for a different simulation set, e.g., with extended energy range up to EeV, this cut should be adjusted accordingly.
The fit range for the time curvature does not feature a lower cut on the lateral distance. However, additionally, for the time fit only signals with a maximum time delay of 4 μs with respect to the shower plane are considered. Hence, very delayed hits which do not follow the general shape of the curvature are neglected.

5.2. Energy estimation

An accurate reconstruction of the primary energy is of particular importance for the measurement of the cosmic-ray energy spectrum. A significant uncertainty on the reconstruction of the primary energy arises already from the hadronic interaction model used in the simulations. Thus, it is crucial to reduce additional contributions to this uncertainty originating from the analysis, which would further limit the reliability of the energy reconstruction. Because of extrapolation uncertainties, the hadronic interaction models are least valid for high energies. Due to the focus on high energy events, this is in particular important for IceCube-Gen2. Since in a measurement no a-priori information about the primary mass is available, an additional bias is introduced by differences in nucleus-nucleus interactions in the atmosphere for light and heavy cosmic rays [61]. Also the response of the detector array can be mass dependent, which can further increase this mass bias. Hence, aside from an accurate determination of the primary energy a reduction of the systematic mass bias is desirable.

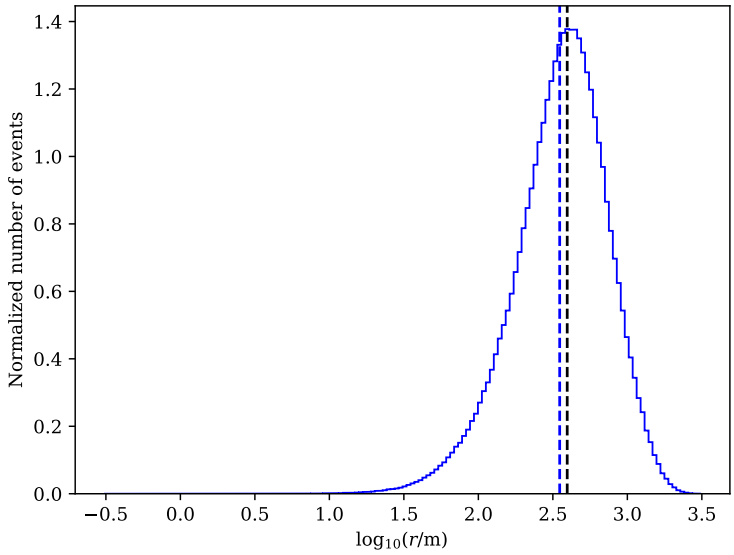

Figure 5.3.: Lateral distance distribution of triggered detectors (excluding saturated detectors) for events with at least 20 hits. The blue line corresponds to the average lateral distance of ∼354 m. For the analysis this value is rounded to 350 m. The black line represents the position of the bin with the most entries, i.e. denotes the most probable lateral distance of 402 m.

As first proposed by Hillas [150], the signal strength at a certain lateral distance is connected to the shower size and therefore the primary energy. This signal strength is often referred to as reference signal S_{ref}, describing the signal at a particular reference distance R_{ref}. Hence, for an accurate energy reconstruction, a proper choice of R_{ref} is highly relevant. In principal, different approaches for the derivation of an optimal reference distance have been developed throughout different experiments [151, 152]. For a preliminary study on the energy reconstruction with the IceCube-Gen2 scintillator array, two different approaches have been investigated and compared within the scope of this thesis.

Analytical approach

The first method was originally used for the IceTop analysis [151], but also applied for the scintillator array of the IceTop enhancement [5]. The main idea is based on the minimization of the covariance between the energy estimator S_{ref} and β in order to minimize the dependence on the LDF slope. For the DLP function the according reference distance at which this covariance vanishes can be calculated analytically when applying certain simplifications. The starting point for the derivation denotes the DLP function in logarithmic form, which accordingly describes the logarithm of the signal strength (see [151] for more details on the calculations):

$$\log_{10}(S_i) = \log_{10}(S_{\text{ref}}) - \beta \log_{10}\left(\frac{r_i}{R_{\text{ref}}}\right) - \kappa \log_{10}^2\left(\frac{r_i}{R_{\text{ref}}}\right). \tag{5.7}$$

Since the signal likelihood contains a term for the silent detectors and, additionally, in the second reconstruction step a combined fit of signal and time distributions is performed, the LDF fit has to be simplified in order to find an analytically solvable expression. For this purpose the influence of the hit probability and the time likelihood on the LDF fit are neglected. Now, by considering the fact that the additional parameter κ of the DLP function is constant throughout the reconstruction process, the complex signal likelihood fit is reduced for a given direction and

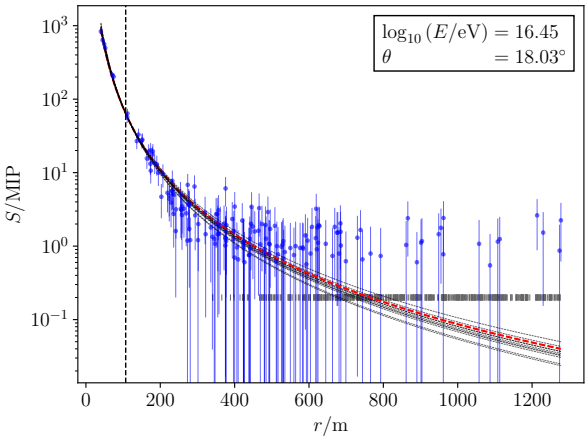

Figure 5.4.: Example fit to a proton initiated event with roughly 28 PeV primary energy and a zenith angle of $\approx 18°$. The red dashed line describes the initial LDF fit. Black dashed lines correspond to repeated fits by variation of β.

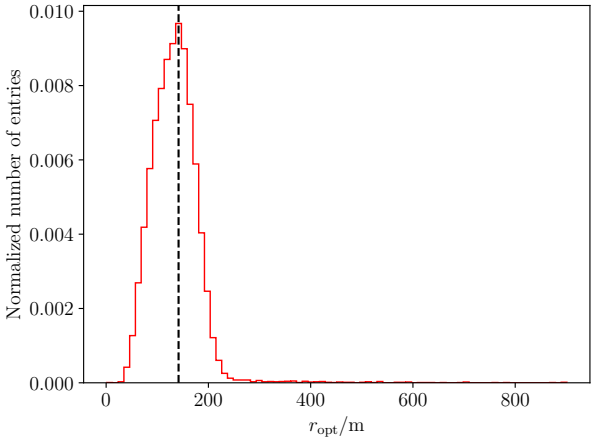

Figure 5.5.: Optimal distance distribution from the fit iteration on a single-event basis. The dashed black line corresponds to the lateral distance of ∼140 m at the peak value.

core position to a simple χ^2 fit to a straight line:

$$\log_{10}(S_i) + \text{const.} = \log_{10}(\mathrm{S_{ref}}) - \beta \log_{10}\left(\frac{\mathrm{r_i}}{\mathrm{R_{ref}}}\right). \tag{5.8}$$

From this expression the covariance between S_{ref} and β can directly be deduced. However, since the signal uncertainties are given by the signal spread, which in turn is a function of the signal strength, a further simplification with $\sigma_S = \text{const.}$ is applied. The covariance then is given by

$$\mathrm{cov}(\beta, \mathrm{S_{ref}}) = \frac{\sum_{\mathrm{i}} \log_{10}\left(\mathrm{r_i}/\mathrm{R_{ref}}\right)}{\frac{1}{\sigma_{\mathrm{S}}^2}\left[\left(\sum_{\mathrm{i}} \log_{10}\left(\mathrm{r_i}/\mathrm{R_{ref}}\right)\right)^2 - \sum_{\mathrm{i}} \log_{10}^2\left(\mathrm{r_i}/\mathrm{R_{ref}}\right)\right]}, \tag{5.9}$$

which can be minimized by simply requiring the numerator to vanish. This translates to

$$\sum_i \log_{10}\left(r_i/R_{\mathrm{ref}}\right) = 0 \Leftrightarrow \log_{10}\left(R_{\mathrm{ref}}\right) = \frac{1}{N}\sum_i \log_{10}\left(r_i\right) = \langle \log_{10}\left(r\right)\rangle. \tag{5.10}$$

Hence, the optimal distance at which to measure the reference signal is given by the average value of lateral distances. For this purpose, the full simulation library[3] of proton and iron showers with up to 45° in zenith angle is analyzed and all events with a minimum multiplicity of 20 detectors are taken into account. The requirement roughly lifts the energy threshold for the event selection to the region of full efficiency for the discussed scintillator array. Hence, only air showers with energies above the full efficiency region are used to determine the reference distance. The distribution of lateral distances of triggered detectors (excluding saturated detectors) for all analyzed showers is shown in Fig. 5.3. The mean value of this distribution corresponds to roughly 350 m.

[3] A different simulations library can lead to a shift of the obtained optimal distance, depending on the number of showers for certain energies. A weighting with a flux model would likely lead to a smaller values, since a smaller weight is applied to more high energy, hence, larger showers.

Numerical approach

The alternative approach is based on an analysis developed for the Pierre Auger Observatory [152]. Despite the goal of this analysis being somewhat similar to the first method, the exact approach is in fact very different. Similar to the previous method, the full set of simulated proton and iron showers with zenith angles up to 45° is used where, again, each event with at least 20 triggered detectors is included. For every selected shower the full signal likelihood fit is applied for an initial LDF fit. In order to minimize the systematic effect on the energy estimator introduced by the uncertainty in the slope parameter of the LDF, the LDF fit is repeated 10 times by random variation of β based on a Gaussian distribution around the β value derived in the initial fit (see Fig. 5.4). The systematic uncertainty in S_{ref} is minimized in the intersection of the different fits, indicating the most stable point of the LDF with regard to an uncertainty in β. In this way an optimal distance can be determined on an event-by-event basis. The distribution of all derived optimal distances is shown in Fig. 5.5. The peak value of roughly 140 m is chosen as overall reference distance[4]. This distance roughly corresponds to the distance between the outer scintillator pairs in each station.

Comparison

Indeed, both tested approaches yield quite different results for the reference distance. Therefore, a direct comparison between both derived values via the reconstruction performance is essential. As mentioned, an ideal energy estimator should provide good statistical precision for the primary energy while featuring a minimal mass dependency.
For the latter, the correlation of the energy estimator and the true energy was analyzed for both reference distances and for both proton and iron primaries (see Fig. 5.6). In general, the smaller reference distance leads to a fairly smooth linear behavior between energy estimator and true energy. However, the mass dependency, represented by the residuals between proton and iron shown in Fig. 5.6, is larger in the whole energy region[5] for all considered zenith angles. In particular, for zenith angles of $30° - 45°$ a reference distance of 350 m for the energy estimator shows a smooth linear trend while providing a very small mass bias. Hence, in the context of mass dependency, 350 m represents an optimal distance[6]. It has to be mentioned, however, that this distance results in a crossing in terms of mass dependence already at energies in the few PeV region for zenith angles up to 30°, which will likely be problematic for studies of energies beyond 100 PeV.
The energy reconstruction precision for both radii is compared in Fig. 5.7 (details on the derivation of the energy resolution can be found in the next section). For energies below roughly 10 PeV, the lower reference distance of 140 m yields significantly better accuracies, translating to a relative energy resolution for vertical showers of $\sim 26\%$ compared to $\sim 39\%$ for 350 m. This is expected as the optimal distance itself decreases for smaller showers, hence, lower primary energies. For higher energies and vertical showers, the energy resolution approaches values below 0.1 in $\log_{10} E$ for both distances. At energies around 100 PeV, a relative resolution of $\sim 9\%$ and $\sim 10\%$ can be reached for a reference radius of 140 m and 350 m, respectively. Due to the

[4] Similar to the analytical approach, a weighting with a cosmic-ray flux model can result in a different optimal distance and can be investigated in future studies.

[5] A comparison of the according energy bias can be found in Fig. B.2

[6] In general, in order to achieve a minimal mass bias, the reference distance can be chosen empirically by scanning many different reference distances directly via reconstruction and minimizing the mass dependency, i.e. by minimizing the difference between proton and iron primaries shown in Fig. 5.7. However, the application of this approach was not possible within the scope of this thesis and can therefore be part of future studies.

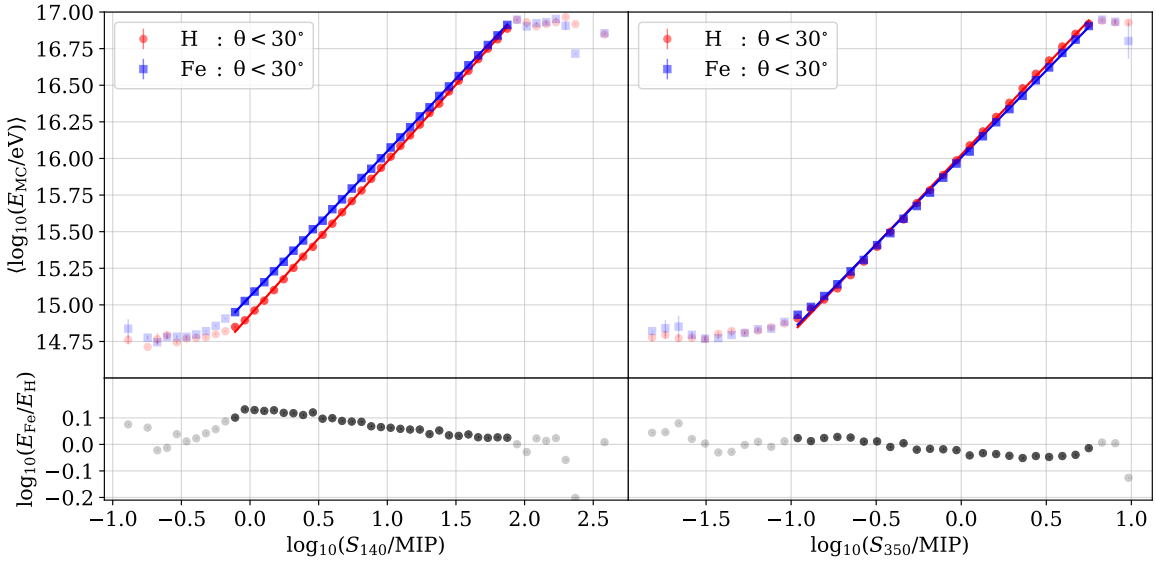

(a)

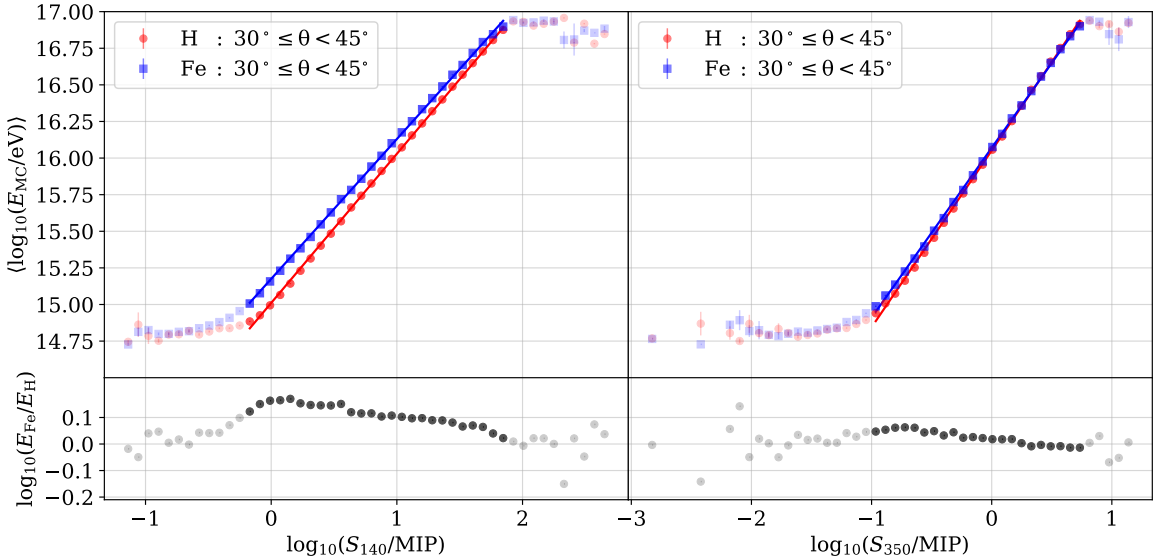

(b)

Figure 5.6.: Relation between true energy and energy estimator for $R_{\mathrm{ref}} = 140\,\mathrm{m}$ (left) and $R_{\mathrm{ref}} = 350\,\mathrm{m}$ (right) for both proton and iron primaries and zenith angles up to 30° (a) and between 30° – 45° (b). Bins containing only a few events due to the spread of the energy estimator as well as bins with truncated distributions due to the binning procedure are shown with lower opacity. The according differences between both primaries are shown in the lower panels of each plot.

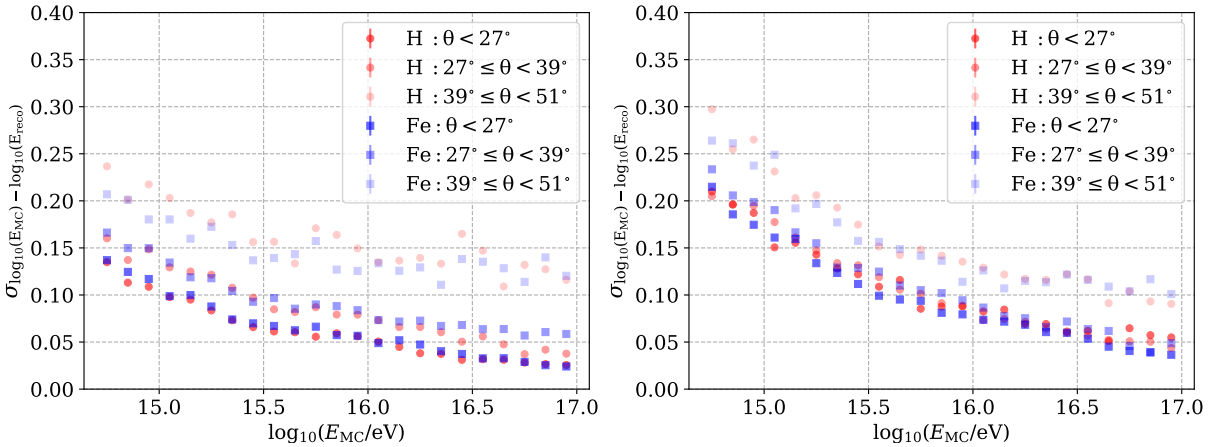

Figure 5.7.: Energy resolution for proton and iron primaries and different zenith ranges for a reference distance of 140 m (left) and 350 m (right).

zenith dependence of the optimal distance, the larger reference distance provides an improved energy reconstruction for more inclined showers above 40° primary zenith angle and for energies above 10 PeV. Nevertheless, when considering only the statistical accuracy in primary energy, a reference distance of 140 m could be chosen. Hence, in general, a stronger focus on reconstruction accuracy or mass dependence, yields optimal distances towards smaller or larger values, respectively.

Thus, based on the direct comparison of both derived distances an optimal choice depends on the focus of a particular analysis. In principle, a precise energy reconstruction is beneficial for any cosmic ray analysis. On the other hand, a mass dependence can introduce biases in composition studies and leads to a wrong reconstruction of the energy spectrum, if the mass composition changes with the energy in an unknown way.
However, taking into account the optimization of the parametrization of the signal distribution (see section 4.3.1), in particular the choice of proper LDF parameters via χ^2 calculation, a reference distance as large as 350 m seems problematic. In the parameter optimization shown in Fig. 4.9 a distance above $\sim$ 300 m already corresponds the region of increase in the χ^2 distribution. However, an optimal distance should be chosen within the region of best agreement between model and simulated data, hence, with small χ^2 values. For this reason, a reference distance of 240 m is chosen[7] as intermediate value within the fairly large gap in between both derived distances. This value roughly denotes the edge of the flat part in the χ^2 distribution. In fact, for zenith angles up to 30° and energies $\gtrsim$ 10 PeV a reference distance of 240 m provides an even smaller mass bias than 350 m. Hence, for the quantification of the reconstruction performance of the Gen2 scintillator array a reference distance of 240 m is used.

5.3. Reconstruction performance

The reconstruction of primary characteristics is based on the models for signal and time distributions. Since fit stability and accuracy are mainly determined by the amount of sampling points and therefore the multiplicity, the reconstruction accuracy is generally expected to increase with increasing energy. An example of the reconstructed distributions as well as the reconstructed fits for an event with high multiplicity is illustrated in Fig. 5.8. The small difference between

[7]The according mass bias comparison is shown in Fig. B.2

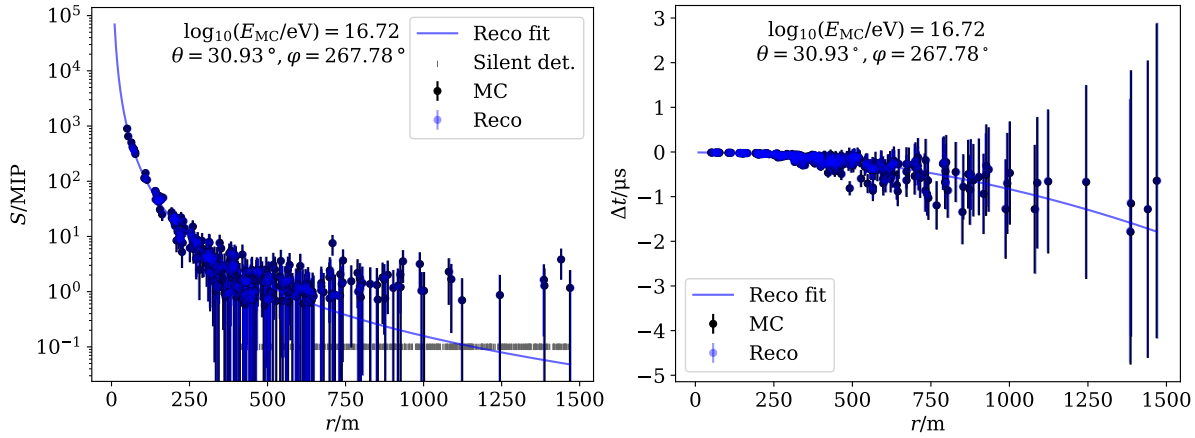

Figure 5.8.: Example event of an air shower reconstruction for a simulated proton shower with roughly 52 PeV true primary energy and $\approx 31°$ and $\approx 268°$ primary zenith and azimuth angle, respectively. The signal as well as time distributions are shown on the left and right, respectively. Black points show the MC data with corresponding uncertainties (based on the spread parametrizations derived in section 4.3.1, calculated via signal values) indicated by the error bars. The reconstructed distribution and the reconstructed fit are illustrated in blue.

true and reconstructed distribution indicates a high reconstruction quality for this particular event. Since the LDF fit incorporates silent detectors, it undershoots the signals for large lateral distances, as it fits to the signal density rather than to the pure signal values. However, as discussed in section 4.3.1, this does not reduce the reconstruction resolution. In fact, the rather small signals in the tail of the distribution are further suppressed in the likelihood fit by the parametrization of the signal fluctuations. A similar suppression is incorporated in the time spread, causing the time likelihood fit to be driven mainly by the region close to the shower axis, which in general is most sensitive to the primary direction.

For the analysis of reconstructed events, only showers with true core position up to 100 m to the array border (including the IceTop enhancement area) are included in order to study the performance of the full Gen2 scintillator array. Additionally, only showers with up to $\approx 51°$ primary zenith angle are considered. It has to be noted, however, that the reconstruction procedure is specifically optimized for more vertical showers up to 45°. Furthermore, for every event a successful reconstruction is required.

For the quantification of the reconstruction performance, the accuracy of the reconstructed parameters for proton and iron as upper and lower limit for hadron initiated air showers is investigated. An investigation of the reconstruction performance for γ initiated showers should be part of future studies.

Reconstruction of geometrical parameters

The reconstruction parameters describing the geometry of a particular shower are the primary direction and the coordinates of the shower core at the observation level. The core position is an important input parameter for the radio reconstruction [3] and affects both LDF and shower front fit, hence, all reconstruction observables. The reconstruction accuracy of the core position can in principal be quantified by simply considering the difference between reconstructed and true core position in the xy-plane. However, taking into account the reconstructed core position as input

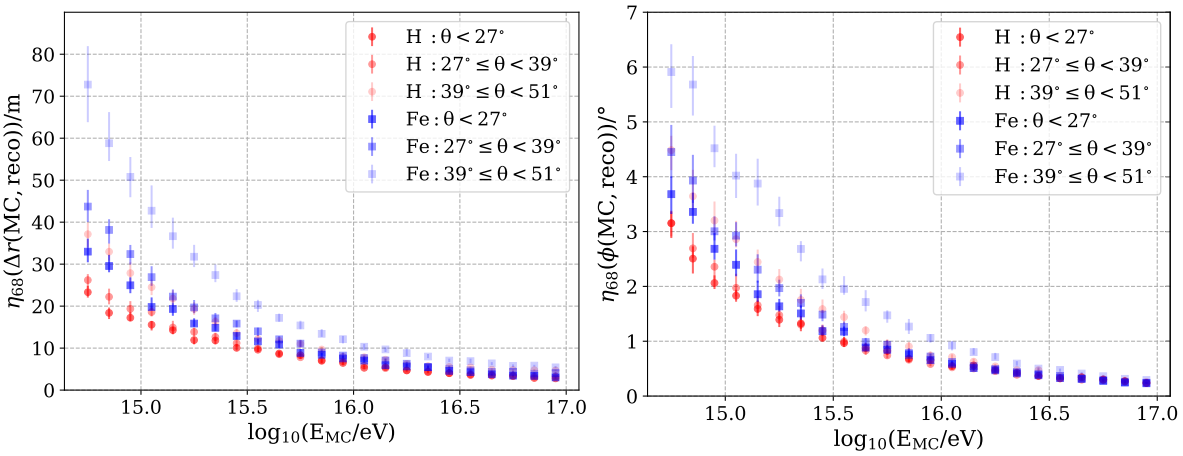

Figure 5.9.: Reconstruction resolutions for the core position (left) and primary direction (right) for both proton and iron primaries for three different zenith bins. The error bars indicate the 95 % confidence interval for each bin calculated via bootstrap method.

parameter for the future hybrid reconstruction with the radio array, an alternative approach is used. Since for inclined showers a slight change in the shower axis leads to a difference in the core position proportional to $\sec\theta$, instead, the perpendicular distance $\Delta r(\mathrm{MC}, \mathrm{reco})$ to the MC shower axis is calculated for each shower. The derived distances are binned in true energy and the 68th percentile of the distribution in each bins denotes the according resolution. The core position resolution for proton and iron primaries as function of primary energy between 500 TeV and 100 PeV is shown in Fig. 5.9 (left). The energy bins are chosen with a width of 0.1 in $\log_{10} E$.

For energies below the PeV region the core position accuracy can get as poor as $\gtrsim$70 m for inclined iron showers between $39° - 51°$ zenith angle, which roughly corresponds to the distance of scintillator pairs within each station. However, for more vertical showers the accuracy is significantly higher, reaching $\gtrsim$20 m resolution for the best case scenario, namely vertical proton showers. As heavier primaries on average interact earlier in the atmosphere compared to proton primaries with same energy, the shower maximum is reached at a larger altitude. In particular for lower energies this results in a significantly lower multiplicity, hence, a reduced reconstruction resolution.

Approaching energies up to 100 PeV, the resolution generally improves to accuracies of below 10 m for both primaries and all here considered zenith ranges. It has to be noted that, at such high core position accuracies, the dimension of the scintillation panel itself becomes a relevant factor for the resolution. In order to quantify the accuracy of the angular reconstruction, the space angle $\phi(\mathrm{MC}, \mathrm{reco})$ (angle between true and reconstructed primary direction) is binned as function of primary energy. Similar to the core position the resolution is then given by the 68th percentile of the according distribution in each bin (see Fig. 5.9 (right)). As expected, the reconstruction resolution improves with increasing primary energy, leading to sub-degree accuracies above a few 10 PeV. For lower energies, accuracies of a few degrees can be achieved. For large zenith angles, absorption effects for the electromagnetic shower component increase, leading to a smaller multiplicity. In combination with the fact that the projection of the shower plane on the ground increases with $\sec\theta$, this results in a less distinct and generally flatter signal and time distribution. Such flat distributions are described less precisely by the according shower front function. In particular for the large Gen2 surface array, an improvement might be achieved by incorporating, e.g., a dedicated function describing the shower front created by muon dominated signals.

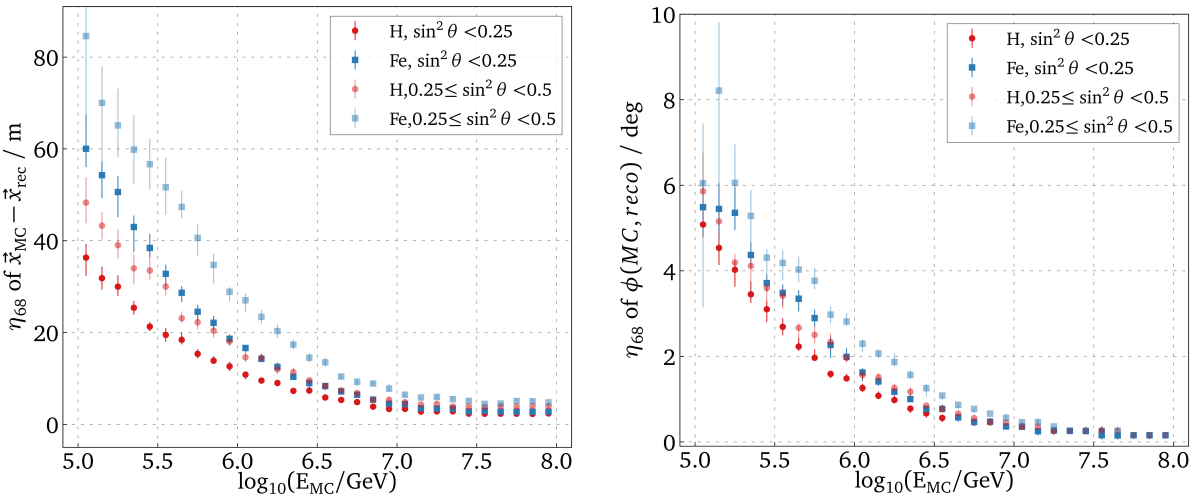

Figure 5.10.: Reconstruction resolution of the IceTop enhancement scintillator array for the core position (left) and the primary direction (right) for both proton and iron primaries for two different zenith bins. Taken from [5].

Comparison to the IceTop enhancement

Since in the baseline design the IceCube-Gen2 surface stations are identical to the IceTop enhancement stations, the reconstruction performance can be directly compared. The main difference between both arrays lies in the more sparse distribution of surface stations for Gen2. Accordingly, in particular for lower energies, the IceTop enhancement array is expected to provide a better reconstruction performance.
In fact, the reconstruction resolutions for core position[8] and direction exhibit comparable values throughout the full efficiency region. However, since, due to the more densely spaced stations, the reconstruction threshold of the enhancement array is lower than for the Gen2 surface array, the high reconstruction accuracy is reached already for lower energies (see Fig. 5.10).
Overall, the IceCube-Gen2 surface array provides a smooth overlap in reconstruction performance to the IceTop enhancement array with comparable reconstruction resolutions for energies above the multiple PeV range, while at the same time increasing the effective area by a factor of 8.

Comparison to other experiments

The LHAASO experiment can study cosmic rays for energies up to a few EeV [153]. In the region of $10 - 100\,\mathrm{PeV}$ Cherenkov detection is used to infer the primary characteristics. In this energy region angular resolutions of 0.6° and core position resolutions of roughly 3 m can be reached [153]. These values are derived via simulation of proton and iron primaries of $10 - 300\,\mathrm{PeV}$ energy and zenith angles of 25° and 45° (the telescopes point at 35° in zenith), weighted with a spectral index of -2.7 [153]. For energies below ∼PeV, however, LHAASO already reaches sub-degree angular resolutions[9] with its scintillator array [154]. However, the 115 scintillation detectors are spaced much more densely with distances of 15 m [154]. The low-energy extension

[8]The core position resolution for the IceTop enhancement is derived based on the difference $(\vec{x}_{\mathrm{MC}} - \vec{x}_{\mathrm{rec}})$ between true and reconstructed core position in the xy-plane.
[9]For simulations of five different primary masses and zenith angles up to 60° generated with respect to the Hillas Model [154]

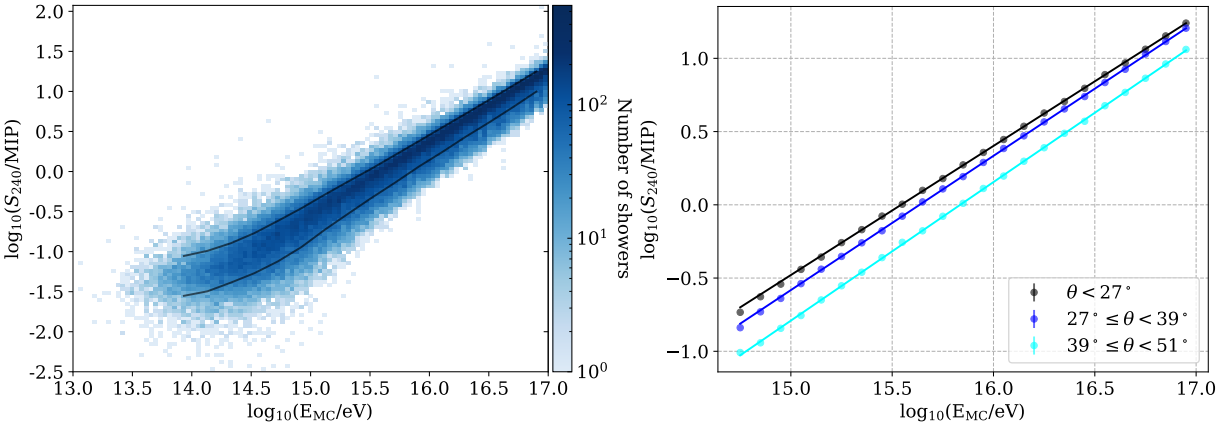

Figure 5.11.: Left: Energy estimator distribution as function of true energy for proton and iron primaries with up to 51° zenith angle. The black lines indicate the 2σ band, roughly illustrating the increasing energy accuracy toward higher energies. Right: Energy estimation distribution for proton and iron primaries binned as function of true energy for three different zenith bins. The linear fits denote the calibration curve required for the energy reconstruction. The error bars are very small and indicate the error of the mean.

of the Telescope Array, TALE, can measure cosmic rays in the PeV to EeV region via fluorescence and Cherenkov emission [74]. Simulated air showers of four different primary masses and zenith angles of $31° - 55°$ in the $\sim 20 - 200$ PeV region, weighted with a spectral index of -2.92, yield angular resolutions in the sub-degree level [74]. The Auger Muons and Infill for the Ground Array (AMIGA) with its stations of water-Cherenkov tanks (distributed over a hexagonal grid with a detector spacing of 750 m) and associated buried scintillation detectors, can reach angular resolutions in the sub-degree level in the case of 6 or more triggered stations and for energies of $3 \cdot 10^{17}$ eV and zenith angles up to 55° [155]. In the according analysis 53 of the total of 61 stations were included.

Hence, specifically for the high energy region, the scintillator array of IceCube-Gen2 reaches comparable accuracies in the reconstruction of the geometrical parameters with respect to experiments operating in the same energy regions. Towards lower energies the reconstruction resolution is limited by the detector spacing.

Reconstruction of the primary energy

For a preliminary quantification of the energy resolution of the Gen2 scintillator array, the energy estimator distribution was studied for different ranges of the primary zenith angle. The according distribution for proton and iron primaries and zenith angles up to 51° is shown in Fig. 5.11 (left). Since in a real measurement no a-priori information about the primary mass is available, the combined distribution for proton and iron primaries was used in order to determine the energy calibration curves (see Fig. 5.11 (right)). For the derivation of the calibration curves the energy estimator distribution is binned in primary energy. A linear fit describing the relation between energy estimator and true energy can then be used to infer the according reconstructed energy. Since the distributions of the difference between true and reconstructed energies are normally distributed, each bin can be approximated with a Gaussian model. The energy resolution in each bin is then given by the width of the according Gaussian (see Fig. 5.12 (left)).

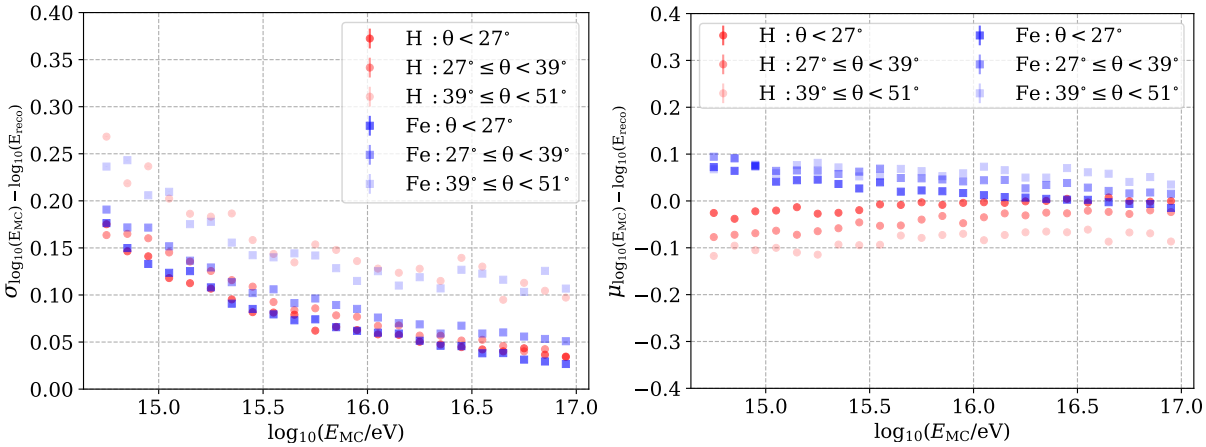

Figure 5.12.: Energy resolution (left) and bias (right) for proton and iron primaries for three different zenith bins, assuming $R_{\mathrm{ref}} = 240\,\mathrm{m}$.

For vertical showers the primary energy can be reconstructed with a precision of below 0.05 in $\log_{10} E$, which roughly translates to $< 10\%$ accuracy at 100 PeV. For lower energies, the precision decreases to $\sim 15\%$ and $\sim 30\%$ at 10 PeV and 1 PeV, respectively. For more inclined showers, the statistical accuracy declines rapidly. In principal, due to a difference in the height of the first interaction, the shower size at the ground and therefore the reconstructed energy should differ for different primary masses but same energy, depending on the observation level. This results in an over-/underestimation of the primary energy for different mass groups. In order to quantify the energy bias depending on mass, zenith angle and energy, the systematic shift represented by the mean of the Gaussian model for each energy bin is investigated (see Fig. 5.12 (right)). As expected, for lower energies the energy reconstruction features an opposing systematic shift for proton and iron primaries. For increasing energies the mass bias generally reduces, as the difference in multiplicity between proton and iron induced showers declines. Since an equal proton/iron composition is used, the absolute bias is roughly similar for both primaries. At the lowest shown energies, however, the absolute bias for proton differs compared to iron depending on the zenith angle since the relative difference in multiplicity is larger.
It has to be noted, however, that the energy bias and therefore the systematic uncertainty in energy reconstruction can be as large as the resolution itself. Additionally, since the reconstructed energy is obtained via MC data, the energy reconstruction is further biased by the particular hadronic interaction model used in the simulations.

Reconstruction Efficiency

The reconstruction efficiency describes the application range and stability of the reconstruction and is therefore an important quantity with respect to studies of the cosmic-ray energy spectrum. The exact definition of the efficiency, however, is different compared to the trigger efficiency. In the context of shower reconstruction, the ratio of successful reconstructions to all selected events within the same region measures the efficiency. The requirements of a successful reconstruction were already discussed within this chapter. For the efficiency derivation all showers with true core position up to 100 m inside of the Gen2 surface array are included. The resulting efficiency curve as function of true energy is shown in Fig. 5.13. The reconstruction efficiency for rather vertical showers up to 27° in zenith exhibits quite low threshold values of ∼400-500 TeV, depending on the primary mass. Above these threshold values all showers can be reconstructed with almost 100%

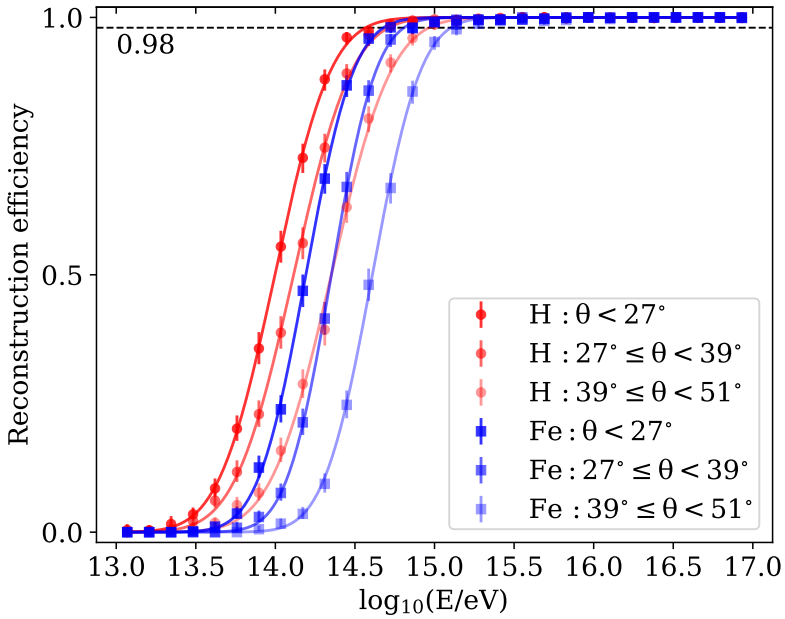

Figure 5.13.: Reconstruction efficiency for proton and iron primaries for three different zenith bins.

efficiency. Similar to the trigger efficiency, the threshold increases with increasing inclination, reaching values of around 900 TeV for iron primaries with up to 39° zenith angle. At around 1.3 PeV all showers up to 51° can be reconstructed with full efficiency. These thresholds indeed fulfill the requirements for the planned scintillator array of IceCube-Gen2, as discussed in more detail in the next section.

5.4. Discussion on science capabilities

For the classification of the different science goals of the Gen2 surface array only aspects that are related to the performance of the scintillator array will be discussed. An overview of the complete science case can be found in [2].
In general, the different cases are ordered in four main topics:

- Veto capabilities
- Study of hadronic interactions
- Analysis of the cosmic-ray spectrum
- Calibration capabilities

Regarding the **veto science case**, an important quantity is the trigger efficiency. As shown, the IceCube-Gen2 scintillator array can achieve trigger thresholds of ∼500 TeV for vertical proton showers and below 1 PeV for more inclined showers up to 51° for all primary masses, leading to a threshold comparable to the IceTop array [156]. Since, however, the exposure for the Gen2 surface array will be much larger, the geometrical acceptance for coincidence events is generally extended to a larger zenith range. Moreover, due to the elevation of the scintillation detectors on the poles, the detection threshold should not increase over time because snow accumulation is avoided. This is a great advantage compared to the IceTop array.
Additionally, the veto capabilities will be further enhanced by the radio component of the IceCube-Gen2 surface stations, since in contrast to the scintillation panels the radio antennas are particularly effective for very inclined showers. Thus, the radio antennas could partially take over the surface veto for inclined showers at around 100 PeV [156].
It is important to mention that, in order to fully quantify the veto capabilities, more detailed studies have to be performed, e.g., on the rate of very deeply interacting showers that are not detected at the surface array, but can trigger the in-ice array as well as on random coincidence events at the surface.

The true uniqueness of IceCube and IceCube-Gen2 comes from the combination of a surface and in-ice array. A main advantage of this detector arrangement lies in the possibility to measure air-shower events at the surface with coincident high energy muons measured deep in the ice. In this way, important questions regarding different **hadronic interaction models** can be investigated. On the one hand, a discrepancy between predicted and measured muon number persists at energies above roughly 10 PeV [157]. On the other hand, more precise measurements of prompt muons[10] can be carried out. In particular for high energies, the charm production depends strongly on the specific hadronic interaction model [158, 63]. In general, a measurement of the prompt muon flux is already possible with the existing IceCube detector. Though, due to its fairly small aperture the statistics for such measurements are very limited. This situation changes, however, when moving to IceCube-Gen2, due to the huge gain in aperture of a factor of $\gtrsim 30$ [103]. Of particular interest in prompt muon studies is the transition region of conventional muons, i.e. mostly from pions and kaons, to prompt muons. This transition is expected at energies around $0.5 - 1$ PeV [159]. Since the nucleons in heavier primaries carry on average smaller energies than for proton primaries of same energy and the muon energy is strongly connected to the nucleon energy [159], proton primaries produce more high energy muons. For this reason, in order to study the transition of conventional to prompt muons, a detection threshold of about 500 TeV for proton primaries is desirable [2]. The scintillator array of the baseline design of the IceCube-Gen2 surface array fulfills this requirement for primary zenith angles of up to 45° [2].

[10] Primarily produced by charm decays

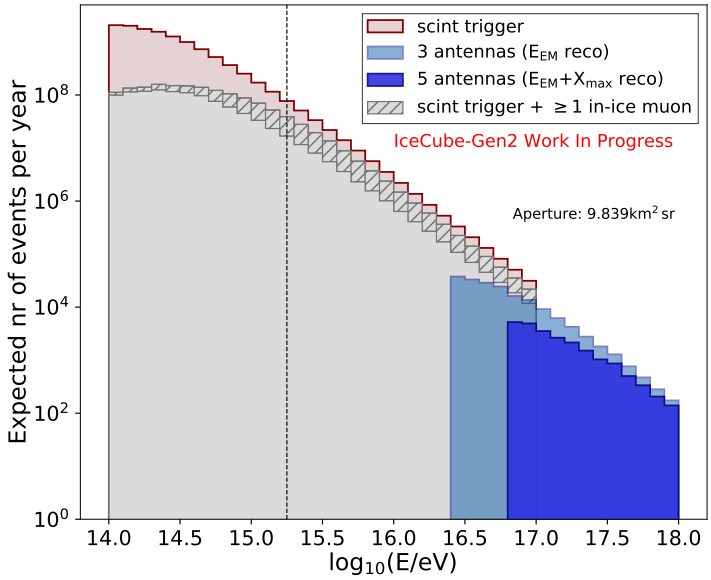

Figure 5.14.: Expected events per year for an H4a flux assumption and an exposure calculated for zenith angles up to 51° and a containment area of up to 100 m to the IceCube-Gen2 surface array border (see Fig. 4.3 (left)). The colored histograms indicate the event rates for different detection scenarios. A pure trigger requirement (five scintillators $\geq$ 0.5 MIP) of the IceCube-Gen2 scintillator array is shown in red. The dashed black line roughly indicates the full-efficiency threshold for the scintillator array for showers up to 51°. The expected event rates for a combination of the scintillator trigger with at least one coincident in-ice muon that could be reconstructed are illustrated in gray. The hatched and filled histogram indicate an upper and lower limit on the number of expected coincident events, respectively (for more details see [3]). The expected event rates under the assumption that a shower-energy reconstruction and in addition an X_{max} reconstruction via radio detection is possible are shown with light and dark blue histograms, respectively. Plot taken from [3].

In combination with the IceCube-Gen2 surface array, studies of the muon energy spectrum can be carried out via surface and in-ice measurements. In principle, the Gen2 scintillator panels are not efficient in muon detection as they are not buried in an absorption medium. However, to some extent the surface array can be considered a muon detector simply by its sheer size. This is based on the fact that the electron/muon ratio decreases with increasing lateral distance. Additionally, for showers falling onto the Gen2 area, the IceTop tanks as more efficient muon detectors are arranged at fairly suitable distances from the shower axis. Since the snow accumulation of the tanks continues such muon studies would potentially get enhanced even further over the years.

For **cosmic-ray analysis** in general, the reconstruction performance of the surface array is crucial. With a positional resolution of a few meters as well as angular accuracies in the sub-degree level, the scintillator array alone can provide high accuracy reconstructions of the direction of an incoming cosmic ray for energies of a few 10 PeV. Especially in the context of hybrid measurements such high accuracies represent valuable input for the radio reconstruction [3]. Specifically, such a precise direction reconstruction can be relevant for cosmic ray anisotropy studies. Additionally, hybrid detection can be utilized in order to study composition dependent anisotropies. A preliminary estimation on the energy reconstruction performance yields accuracies of $\lesssim$0.1 in $\log_{10} E$ for up to 51° zenith angle approaching energies of 100 PeV. For more vertical showers at $\sim$ 100 PeV the energy accuracy reaches below 0.05 $\log_{10} E$. A combined reconstruction with the radio measurements can yield an improvement due to the possibility of a good determination of

the electromagnetic component. Furthermore, the access to $X_{\max}$ via radio detection together with muon measurements at the surface and with the in-ice array promises great mass discrimination potential [160].
Overall, combined with the fairly low reconstruction thresholds at around 1.3 PeV for all primaries and zenith angles up to 51°, the cosmic ray spectrum can be analyzed comprehensively. The Gen2 surface array will be sensitive specifically in the region where the Galactic to extragalactic transition in the cosmic ray energy spectrum is expected. A precise knowledge of the mass composition is crucial for a better understanding of the origin of this transition. Further, for both the region of lower and higher cosmic ray energies an overlap to other experiments will be given [3], allowing for complementary measurements.

Since IceCube-Gen2 features a much larger acceptance for coincident air-shower measurements, the combination of surface and in-ice signals can be used as **calibration tool** for the in-ice detectors. For this purpose a precise air-shower detection with the surface array is desirable [2].

The expected event rates for the IceCube-Gen2 surface array for different detection requirements are illustrated in Fig. 5.14. The IceCube-Gen2 surface array will detect roughly $10^2 - 10^4$ events per year for energies around 100 PeV. A large part of these events will feature at least one in-ice muon that can be reconstructed as well as a possible reconstruction of the shower energy and $X_{\max}$ via radio measurements.

Chapter 6.

Potential of primary mass determination

As discussed in chapter 2, the determination of the primary mass is one of the most crucial tasks for the interpretation of cosmic-ray air-shower measurements. Due to the different interaction cross-sections of heavier nuclei in the atmosphere compared to protons, the height of the first interaction differs in average for different mass groups but similar primary energy. The resulting difference in shower development is convoluted in the lateral distribution observed with a ground-based air-shower detector array.
Currently the most promising methods towards cosmic-ray mass separation rely on the separation of different shower components via hybrid measurements [160, 161]. In particular the electron/muon ratio at adequate lateral distances constitutes a powerful tool for mass separation since heavier primaries manifest a larger muon content. Although the IceTop enhancement and IceCube-Gen2 surface arrays do not feature dedicated muon detectors for a separation of electromagnetic and muonic shower components, a separation of the muonic component can, to some extent, be achieved by utilizing, e.g., the signal differences in scintillation detectors and ice-Cherenkov tanks at a certain lateral distance [5]. This is caused by the fact that, mainly based on the detector geometry, the IceTop tanks are more sensitive to muons compared to the scintillator panels. Nevertheless, the major contribution of the tank signals comes from photons [151]. Taking into account that the relative muon density increases with increasing distance from the shower axis, the response at a certain distance should be analyzed in order to increase the muonic contribution to the tank signals. An according simulation study for the IceTop enhancement array has been performed [3]. With the IceCube-Gen2 surface array similar studies can be carried out, as discussed in section 5.4. Moreover, the radio antennas can constitute an important role in primary mass determination by enabling a measurement of X_{max}.

6.1. Mass discrimination via LDF characteristics

One rather simple method, is the usage of a mass sensitive parameter from the LDF. Since the slope of the lateral distribution is related to the shower age and therefore contains information about the shower development, its potential towards cosmic-ray mass separation is investigated within this section.
In this analysis only reconstructed showers with true core position up to 100 m to the array border are included (see Fig. 4.3 (left)). In the reconstruction the DLP function is used to describe the signal distribution. The distributions of the slope parameter β are shown in Fig. 6.1.

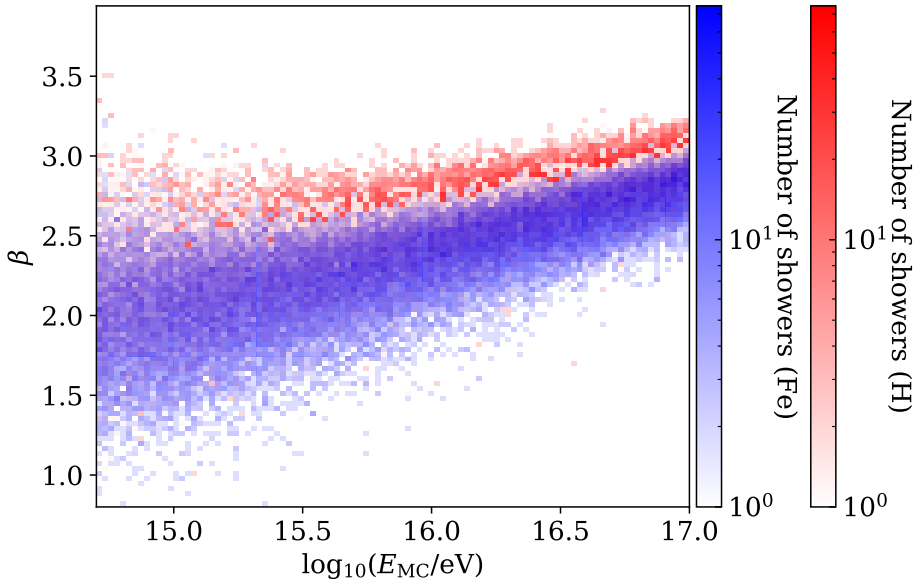

Figure 6.1.: Distribution of the LDF slope parameter for proton and iron primaries with zenith angles up to 45°

Clearly visible is the energy dependence of the slope parameter. This is likely caused by the fact that the deeper shower maximum for increasing primary energy leads to a steeper signal distribution. Additionally, β features a more distinct mass separation for high energies. In order to better visualize the difference, the according histograms for zenith angles up to 45° and primary energies of $10^{16.0} - 10^{16.2}$ eV and $10^{16.8} - 10^{17.0}$ eV are shown in Fig. 6.2. The separation power for each case is quantified via the figure of merit (FOM):

$$\mathrm{FOM} = \frac{|\mu_\mathrm{H} - \mu_\mathrm{Fe}|}{\sqrt{\sigma_\mathrm{H}^2 + \sigma_\mathrm{Fe}^2}}. \tag{6.1}$$

The mean and standard deviation of the according samples of proton and iron initiated showers are represented by μ_H, μ_Fe and σ_H, σ_Fe, respectively. A clear separation between proton and iron primaries is visible for high energies approaching 100 PeV, corresponding to a FOM of 0.87. When taking into account intermediate primaries, however, a larger separation is desirable. Nevertheless, the LDF slope constitutes a valuable input parameter for hybrid analysis.

6.2. Combined analysis with in-ice muons

For an approximate quantification of the mass separation power with a combined analysis with coincident in-ice information, a second mass sensitive parameter is folded in. Although lighter primaries, on average, feature muons with a larger relative fraction of the primary energy, the number of ≥TeV muons for high energy events is expected to increase with cosmic ray mass due to the larger hadronic part in showers of heavier primaries. The surface detector does not feature dedicated muon detectors, however, the unique detector arrangement of IceCube/IceCube-Gen2 can be utilized. Hence, as a preliminary study, additional information about the number of high energy muons coincidentally detected with the in-ice array of IceCube-Gen2 is taken into account. For this purpose, the high-energy ($\geq$ 273 GeV) muons at the surface are extracted and further propagated through the in-ice volume, taking into account energy loss during the

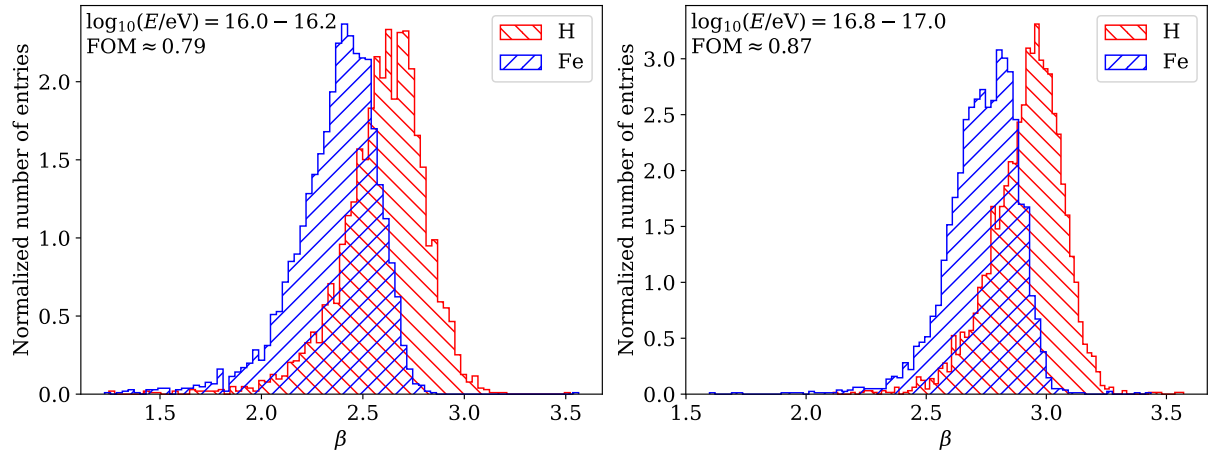

Figure 6.2.: Distribution of the LDF slope parameter for proton and iron primaries for zenith angles up to 45° and different energy regions.

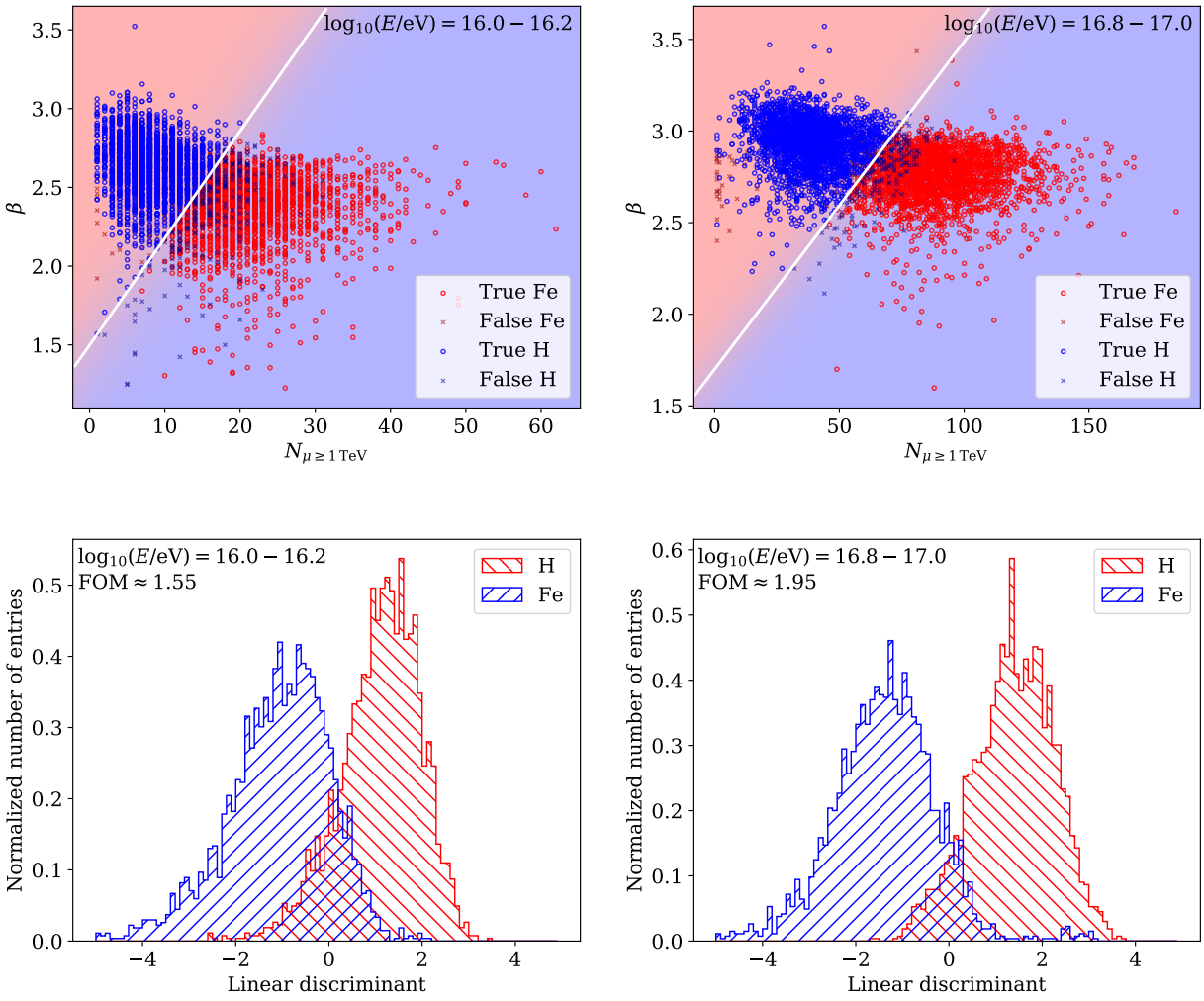

Figure 6.3.: Upper plots: Distributions of the slope parameter and the number of high energy muons for zenith angles up to 45° and different energy regions. Lower plots: Distributions of the resulting discriminant values.

propagation [162]. Further, a simple geometrical requirement of the muon trajectory to intersect the volume defined by the in-ice strings, padded by 60 m, is applied. Finally, all muons with an energy above 1 TeV at the level of the in-ice volume are selected and counted on an event-by-event basis.

In order to combine both, slope parameter and number of high energy muons observed in coincidence with the in-ice array, a linear discriminant analysis (LDA) is performed. This analysis makes use of a classifier, constructed via both input parameters, in order to maximize the separation between different classes, i.e., in this case, proton and iron primaries (for more details see [163]). Additionally, for k classes only $k-1$ classifiers are required [164]. Hence, the two input parameters are combined to a one dimensional classifier, which allows for a quantification of the separation power via FOM. The LDA is performed via the scikit-learn python package[1]. It has to be noted, however, that the LDA assumes a Gaussian distribution for both parameters [163] which can be seen rather as approximation to the actual parameter distribution. For high energies this approximation is reasonable since only small deviations from Gaussian behavior are observed. At energies below roughly 10 PeV, however, the Poisson-like distribution of high energy muons can not be approximated by a Gaussian. Hence, for lower energies a more refined method should be applied in future studies. The details of such high energy in-ice muon distributions are currently under investigation [165].

For the analysis similar shower selection criteria as in the previous section are applied. The distributions of both parameters as well as for the according discriminant is shown in Fig. 6.3. The according FOM values of 1.55 and 1.95 for zenith angles up to 45° for $10^{16.0} - 10^{16.2}$ eV and $10^{16.8} - 10^{17.0}$ eV, respectively, indicate a significant improvement in primary mass discrimination via combined analysis of surface and in-ice information. Especially for energies approaching 100 PeV the full widths of the proton and iron distributions are separated. Although the considered scenario constitutes an idealistic upper limit on the mass separation power with these two parameters, since the muons are not required to be reconstructed by the in-ice array, these values are promising. This is in particular true since further improvements by incorporation of additional parameters and enhanced analysis methods, e.g. neural network techniques [166], can be expected. Hence, with more advanced studies additionally intermediate mass groups might be efficiently separated.

6.3. Prospects

With respect to the different detection channels, namely particle detection via scintillation and ice-Cherenkov detectors and radio detection at the surface as well as the unique opportunity of coincident measurements with the in-ice detector, the IceCube-Gen2 detector features a large potential towards primary mass discrimination. In contrast to the IceTop enhancement array, the statistics for events with combined surface and in-ice information is significantly larger, due to the $\sim$ 30 times larger aperture. This is especially important for the discrimination of photon and hadron induced air showers necessary for the PeV gamma search [2], since photon showers feature the smallest muon content [5]. A quantification of the separation power regarding photons and hadrons should be addressed in future studies.
The mass separation could be improved by inclusion of further detection channels. In this context, the signal ratio of the scintillators and the IceTop tanks at certain lateral distances (an according study was already carried out for the IceTop enhancement array [5]) as well as

[1] More details can be found in `https://scikit-learn.org/stable/supervised_learning.html`

X_{max} measurements via radio detection at energies above 100 PeV constitute valuable input. The combination of radio and muon information has already proven to provide superior mass discrimination performance for other experiments, in particular for inclined showers [160]. An overview over the expected event rates for measurements with combined scintillator and in-ice, and radio information in shown in Fig. 5.14. Overall, the combination of the different detection channels of IceCube-Gen2 offers an enormous potential for mass dependent studies of the cosmic-ray energy spectrum in the energy region where the transition of Galactic to extra-galactic cosmic rays is expected. In addition, combined measurements of air showers at the surface and coincident high-energy muons in the ice allows for studies of hadronic interaction models.

Chapter 7.

Summary

The baseline design of the IceCube-Gen2 surface array will feature one surface station on top of each in-ice string. Accordingly, the stations are spaced roughly 240 m apart from each other, each station containing 8 scintillation detectors and 3 radio antennas for hybrid cosmic-ray air shower measurements. Additionally, 8 in-fill stations between the IceCube-Gen2 surface array and the IceTop enhancement array will provide a smooth coverage, allowing for a detection threshold around 0.5 PeV for vertical proton showers for an area roughly 8 times larger than the current surface area.

In general, the IceCube-Gen2 surface stations are based on the experience gained during the development of the IceTop enhancement stations as well as the successful operation of a prototype station at the South Pole [2], which was deployed in January 2020 [97]. The combination of scintillation panels providing a low detection threshold and high quality reconstruction for rather vertical air-showers up to 40°, and radio antennas, offering a significant improvement in energy and mass determination at energies above 100 PeV [2], enables detailed measurements of the cosmic-ray energy spectrum in the energy region where the transition from Galactic to extragalactic sources is expected. This will allow for measurements complementary on both, the low and high energy sides [3] to experiments like LHAASO [167] and the Pierre Auger Observatory [25], respectively.

In particular, the unique combination of a hybrid surface array with the in-ice detector can improve mass determination [160]. This is a great advantage for practically any cosmic ray science, including the discrimination of different models for hadronic interactions as well as studies of the transition region of conventional to prompt muons [2]. For both cases the muon content at the surface (GeV muons), as currently measured with IceTop at large lateral distances [168], and in the ice ($\sim$ TeV muons) can be utilized. Since, however, the aperture of the IceCube-Gen2 optical/IceCube-Gen2 surface array combination is more than 30 times larger than for IceCube/IceTop, the acceptance for such coincident measurements increases accordingly [116]. Further, the surface array will constitute an efficient veto array for the search of astrophysical neutrinos with the in-ice array. In this context, the discrimination of both vertical and inclined down-going neutrino events originating from atmospheric background will benefit from the complementary capabilities of the scintillation detectors and radio antennas. The exact veto efficiency of both, however, has to be subject of future studies [2].

An overview over the different science cases for air shower measurements with IceCube and IceCube-Gen2 along with the according energy region is shown in Fig. 7.1. Within the scope of this thesis a simulation study of the baseline design of the IceCube-Gen2 scintillator array as well as of possible improvements of the station design has been performed. It was shown that, with

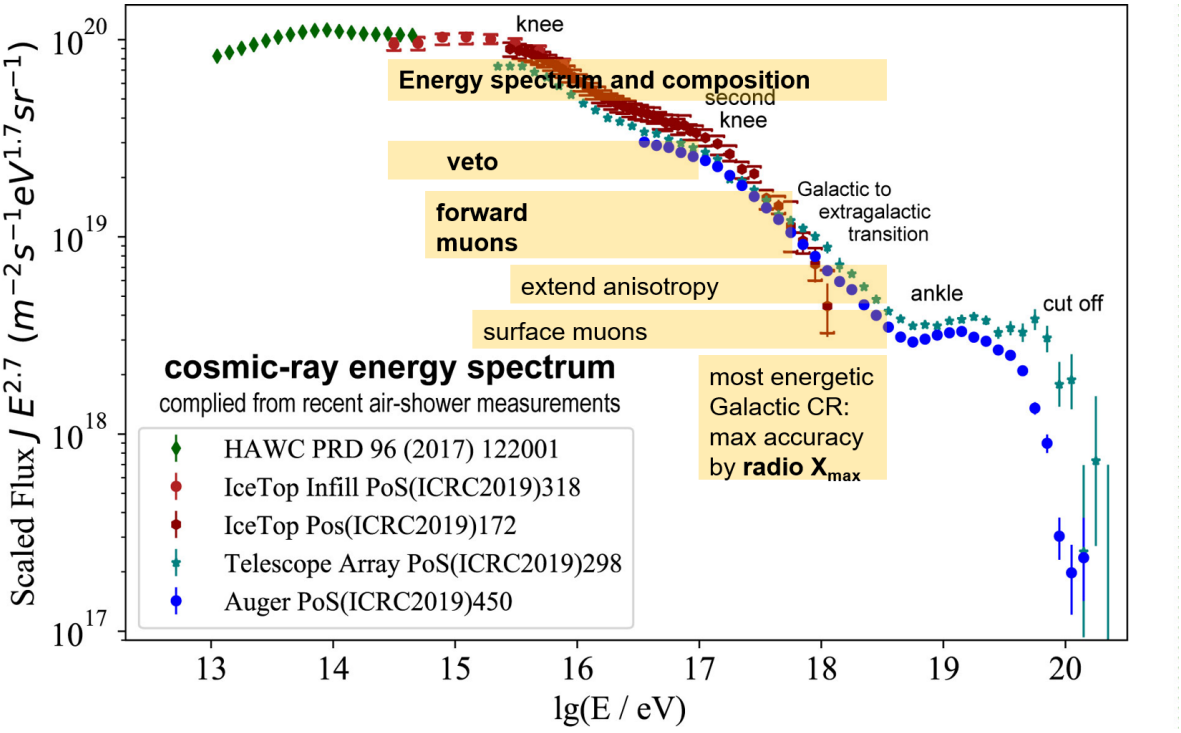

Figure 7.1.: Cosmic-ray energy spectrum with measured by different experiments. The yellow bars indicate the energy range of the different science capabilities of IceCube and IceCube-Gen2 for air shower measurements. Plot taken from [116].

respect to the baseline design, an increased detector spacing between the two scintillator panels of one pair as well as between two pairs of scintillators within one station does not significantly influence the detection threshold. Hence, considering deployment efforts, only the baseline design of the IceCube-Gen2 scintillator array was further investigated. It was shown that the scintillation detectors of the baseline design provide a threshold in the 0.5 PeV region for rather vertical showers and therefore meet the requirements specifically for studies of the transition from conventional to prompt muons measured in the ice. Additionally, the low detection threshold will be beneficial for the veto capabilities of the array. Moreover, the evolution of the detection threshold with the primary zenith angle was investigated, indicating thresholds for up to 63° in zenith which are comparable to the current IceTop array [169].

In order to quantify the capabilities regarding cosmic ray science, the reconstruction performance of the Gen2 scintillator array was examined. The reconstruction procedure, which was developed for the scintillator array of the IceTop enhancement [5], was optimized by studying the spatial and temporal distributions observed by the larger Gen2 scintillator array. The LDF used in the reconstruction procedure, the DLP function, in combination with a simple parabolic function for the time front fit was found to provide a good reconstruction quality. For the angular resolution, values of a few degrees can be obtained for energies in the PeV region. Approaching 100 PeV energies, the accuracy improves to sub-degree level for both proton and iron and zenith angles up to 51°. Additionally, the core position is reconstructed with an accuracy of below 10 m in the region around 100 PeV for showers up to 51° zenith angle. Hence, despite the larger station spacing compared to the IceTop enhancement, the IceCube-Gen2 scintillator array provides a good reconstruction of the shower geometry. This is in particular beneficial in the context of hybrid reconstruction, as the shower geometry reconstructed with the scintillator array will constitute an input parameter for the radio reconstruction [3].

Within the scope of a preliminary study of the energy reconstruction a suitable energy estimator was chosen. In this context, a reference distance of 240 m has been found to provide a compromise between reconstruction accuracy and mass bias. For energies around 100 PeV, the primary energy can be reconstructed with an accuracy of below 10% for vertical proton and iron showers. The resolution in this energy region will be further enhanced by radio measurements.

As a first quantification of the mass separation power, an exemplary study based on the combination of surface and in-ice information was performed. It was shown that a combined analysis of air shower measurements with the Gen2 scintillator array and (idealistic) information about the high-energy muon content detected with the in-ice array leads to a figure of merit (FOM) of ≈ 1.95 for energies approaching 100 PeV and zenith angles up to 45°, which shows indeed the large capability of the array for cosmic ray mass discrimination. More advanced methods as well as incorporation of additional mass sensitive parameters from the different detection channels will allow for improved studies of the mass dependent cosmic-ray energy spectrum in the Galactic to extragalactic transition region. Hence, the IceCube-Gen2 surface array with its hybrid instrumentation for cosmic-ray air shower detection in combination with the in-ice array will provide not only a significant increase in statistics, but also high quality measurements of the primary mass. For energies around the second knee and zenith angles up to 51°, roughly $10^2 - 10^4$ events per year are expected to be detected with the IceCube-Gen2 surface array. For a significant fraction of these events, a reconstruction of the electromagnetic component and X_{max} via radio detection as well as a reconstruction of the high-energy muon content in the ice are possible.

In order to improve the performance in the context of air shower reconstruction further parametrizations of the characteristics of spatial and temporal distributions observed with the IceCube-Gen2 scintillator array can be tested in future studies. In this context, a weighting with the cosmic-ray flux, e.g., via the GSF model, can be applied. Additionally, once available, cross checks with real data should be applied to verify the simulation results. As a second step, the measured distributions should be used to obtain the according parametrizations.
Further, more elaborate studies on different LDFs can be applied, e.g. by investigation and incorporation of the zenith dependence of LDF parameters. This can also lead to a changed trigger probability, which in turn has a large impact on the reconstruction performance. Moreover, a crucial next step is a study of the hybrid reconstruction performance with scintillation detectors and radio antennas. In particular for high energies such hybrid reconstructions can increase the energy accuracy. By additionally considering in-ice information in a combined reconstruction analysis also the primary mass sensitivity can be enhanced.

Appendix A.

First appendix

CORSIKA steering card

The first step in the simulation chain are cosmic-ray air shower is simulations. The formation and propagation of the air shower is simulated with CORSIKA (version number 7.7401). The CORSIKA simulations used for this thesis were compiled with FLUKA (2011.2x.7) and SIBYLL 2.3d for hadronic interactions in the low- and high-energy region, respectively.

Table A.1.: Example steering card (more information can be found in [122]) of the CORSIKA simulations used in this thesis.

RUNNR	0	Run number of the simulation
EVTNR	1	Event number of the first shower
NSHOW	1	Number of showers to be generated in a run
ERANGE	0.010551437390495131E+6 0.010551437390495131E+6	Lower and upper limit of the primary particle energy range (in GeV)
ESLOPE	-1.0	Exponent of the differential primary energy spectrum
PRMPAR	14	Type of the primary particle
THETAP	8.8680 8.8680	Primary zenith angle (in °)
PHIP	206.8405 206.8405	Primary azimuth angle (in °)
ECUTS	0.02 0.01 4.0E-04 4.00E-04	Low energy cut-off (in GeV) for hadrons, muons, electrons and photons
ELMFLG	T T	Flags for the electromagnetic interactions
OBSLEV	284000.0	Observation level above sea level
ECTMAP	1.e11	γ factor cut for the print out
SIBYLL	T 0	Use SIBYLL for high energies
SIBSIG	T	Use SIBYLL cross-sections
FIXHEI	0. 0	Fixed height of first interaction
HADFLG	0 1 0 1 0 2	Flags of the high-energy hadronic interaction model
STEPFC	1.0	Step length factor for multiple scattering
MUMULT	T	Muon multiple scattering angle
MUADDI	T	Additional information for muons
MAXPRT	1	Maximum number of printed events
MAGNET	16.75 -51.96	Components of Earth's magnetic field (in μT) to the north and downwards
LONGI	T 10. T T	Longitudinal development
RADNKG	2.E5	Outer radius for NKG distribution
ATMOD	33	Model of the atmosphere

Table A.2.: Number of scintillator array response simulations for each primary energy and zenith bin. Each of the 100 individual showers in every 0.1 bin in $\sin^2\theta$ and $\log_{10} E$ bin are re-sampled 3 times, with core position up to 1 km outside of the IceCube-Gen2 surface array.

$\sin^2\theta$ / $\log_{10}(E/\mathrm{eV})$	$13.0-14.0$	$14.0-15.0$	$15.0-16.0$	$16.0-16.5$
$0.0-0.1$	1000	1000	1000	500
$0.1-0.2$	1000	1000	1000	500
$0.2-0.3$	1000	1000	1000	500
$0.3-0.4$	1000	1000	1000	500
$0.4-0.5$	1000	1000	1000	500

Scintillator array response simulation

Within this thesis two sets of scintillator array response simulations are used. Both sets are produced via GEANT4 (version 10.4.0), based on the particle input at the observation level obtained from CORSIKA simulations. The simulation set used for efficiency studies of different station layouts (section 4.2) is shown in Tab. A.2. Included are proton initiated air showers with zenith angles up to 45°. The scintillator array response is simulated for 100 individual showers in each energy and zenith bin.

The second simulation includes proton and iron initiated air showers with zenith angles up to 63° and is used for studies of the zenith dependence of the detection efficiency of the baseline design of the IceCube-Gen2 scintillator array (section 4.2) as well as for characterizations of the spatial and temporal distributions (section 4.3). Moreover, this simulation set is utilized for the reconstruction analysis shown in chapters 5 and 6. For zenith angles up to 51° the array response is simulated for primary energies up to $\log_{10}(E/\mathrm{eV}) = 17.0$. The zenith ranges used for specific analyses in this work, are stated in the according chapters.

It should be noted that, due to failed CORSIKA or array response simulations, the stated numbers for both simulation sets also include a small amount of failed simulations.

Table A.3.: Number of scintillator array response simulations for each primary energy and zenith bin. Each of the 100 individual showers in every 0.1 bin in $\sin^2\theta$ and $\log_{10} E$ are re-sampled 5 times within a radius of 1500 m from the center of the IceCube-Gen2 surface array.

	$\log_{10}(E/\mathrm{eV})$ (H primaries)				$\log_{10}(E/\mathrm{eV})$ (Fe primaries)			
$\sin^2\theta$	$13.0-14.0$	$14.0-15.0$	$15.0-16.0$	$16.0-17.0$	$13.0-14.0$	$14.0-15.0$	$15.0-16.0$	$16.0-17.0$
$0.0-0.1$	1000	1000	1000	1000	1000	1000	1000	1000
$0.1-0.2$	1000	1000	1000	1000	1000	1000	1000	1000
$0.2-0.3$	1000	1000	1000	1000	1000	1000	1000	1000
$0.3-0.4$	1000	1000	1000	1000	1000	1000	1000	1000
$0.4-0.5$	1000	1000	1000	1000	1000	1000	1000	1000
$0.5-0.6$	1000	1000	1000	1000	1000	1000	1000	1000
$0.6-0.7$	1000	1000	1000	500	1000	1000	1000	500
$0.7-0.8$	1000	1000	1000	500	1000	1000	1000	500

Appendix B.

Second appendix

Influence of infill stations on the detection efficiency

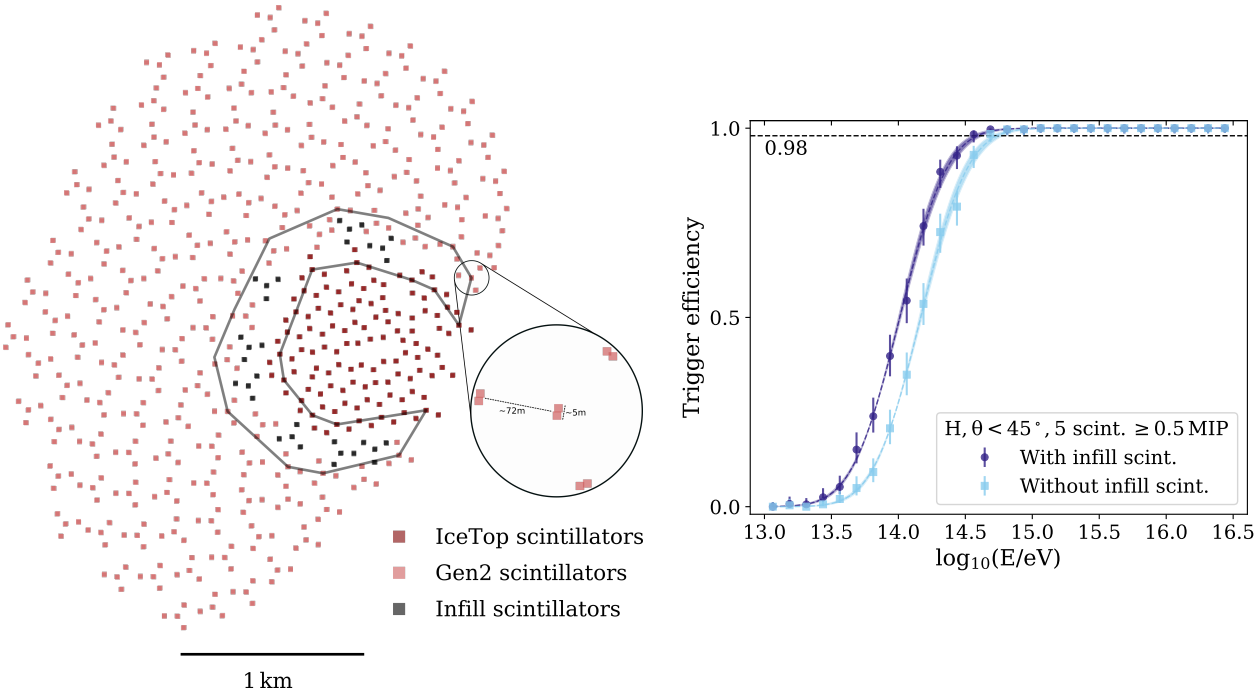

Figure B.1.: Left: Baseline design of the IceCube-Gen2 scintillator array with according shower core selection area (grey polygon) for a dedicated study of the maximum influence of additional infill stations between the IceTop enhancement and the IceCube-Gen2 surface array. Right: According trigger efficiency for the selected showers with and without additonal infill stations.

In order to provide a uniform surface coverage, additionally eight infill stations are placed within the gap between IceTop enhancement and the IceCube-Gen2 surface array. The maximum impact of these station is quantified via a study of the detection efficiency for air showers falling into the gap between both arrays. The area used for the shower core selection is illustrated in Fig. B.1 (left). The resulting detection efficiency with and without taking into account the additional infill stations in shown in Fig. B.1 (right).

Energy bias for different reference radii

In section 5.2, two different approaches for the determination of the optimal distance for an estimation of the primary energy via signal strength are discussed . The resulting energy bias for the choice of 140 m or 350 m as reference distance for the energy estimation is shown in Fig. B.2.

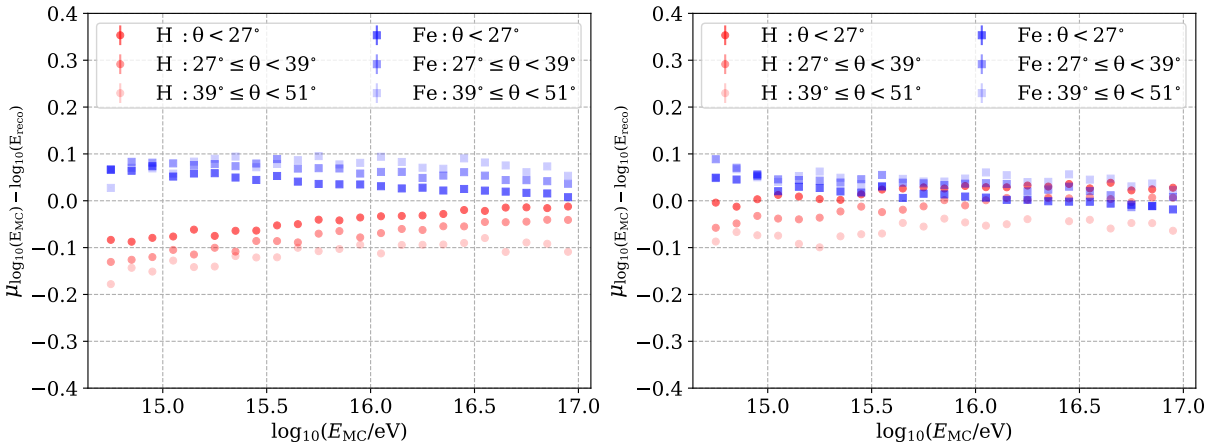

Figure B.2.: Energy bias for a reference radius of 140 m (left) and 350 m (right).

Mass dependence for different reference radii

A proper choice for a reference distance for the primary energy estimation was found to be 240 m. This distance provides a good compromise between a high energy resolution and a small dependence on the primary mass (as discussed in section 5.2). In Fig. B.3, the mass dependencies of the energy estimator for a reference distance of 240 m and 350 m, respectively, are compared for two different zenith ranges. While a reference distance of 350 m provides the smallest mass bias for more inclined air showers between $30\,° - 45\,°$, the distance of 240 m leads to better results for more vertical showers.

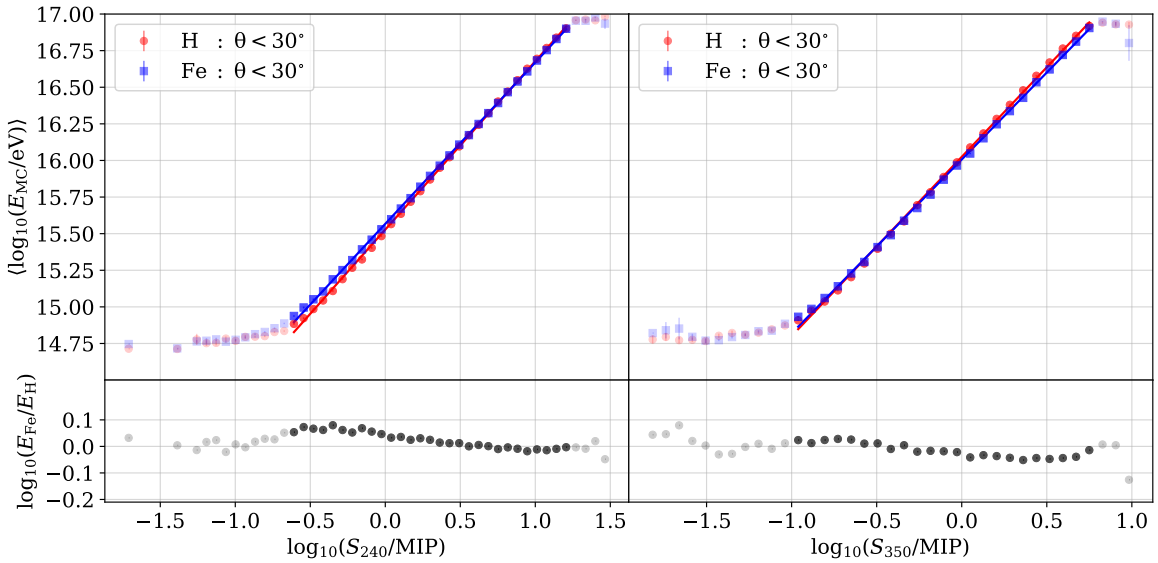

(a)

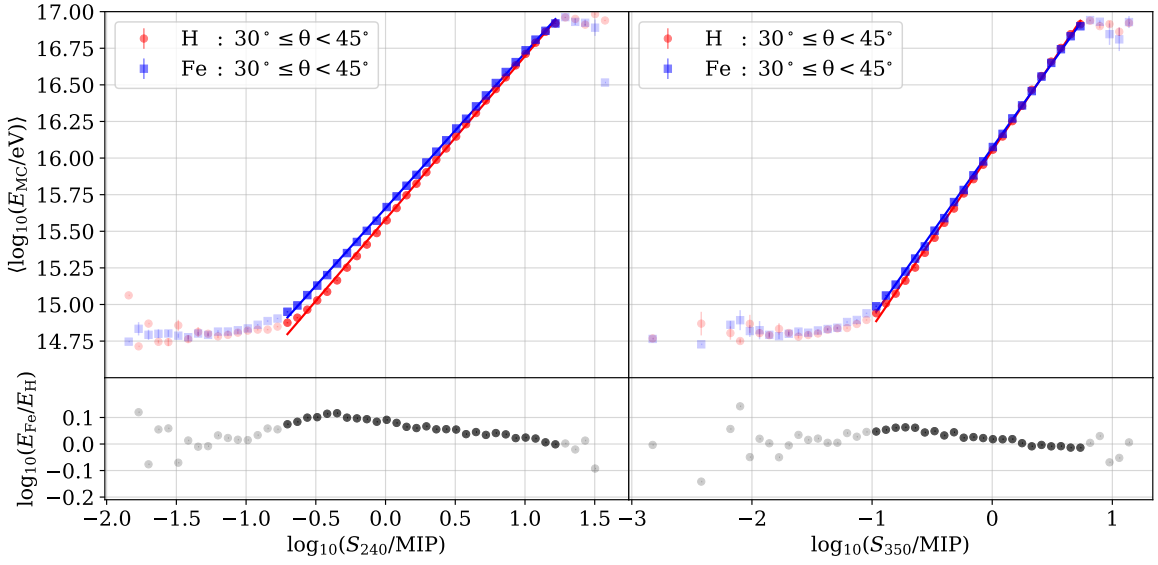

(b)

Figure B.3.: Relation between true energy and energy estimator for $R_{\mathrm{ref}} = 240\,\mathrm{m}$ (left) and $R_{\mathrm{ref}} = 350\,\mathrm{m}$ (right) for both proton and iron primaries and zenith angles up to 30° (a) and between $30^\circ - 45^\circ$ (b). Bins containing only a few events due to the spread of the energy estimator as well as bins with truncated distributions due to the binning procedure are shown with lower opacity. The according residuals given by the difference between both primaries are shown in the lower panels of each plot.

Bibliography

[1] H. Kolanoski and N. Wermes. *Teilchendetektoren - Grundlagen und Anwendungen*. 1st ed. Springer Spektrum, Berlin, Heidelberg, 2016. ISBN: 978-3-662-45349-0. DOI: 10.1007/978-3-662-45350-6.

[2] IceCube-Gen2 Collaboration. F. G. Schroeder. "The Surface Array planned for IceCube-Gen2". In: *PoS* ICRC2021 (2021), p. 407. DOI: 10.22323/1.395.0407.

[3] IceCube-Gen2 Collaboration. A. Coleman, A. Leszczyńska, and M. Weyrauch. "Simulation study for the future IceCube-Gen2 surface array". In: *PoS* ICRC2021 (2021), p. 411. DOI: 10.22323/1.395.0411. arXiv: 2108.04307 [astro-ph.HE].

[4] M. Renschler et al. "Detector developments for a hybrid particle and radio array for cosmic-ray air-shower detection". In: *Journal of Physics: Conference Series* 1181 (Feb. 2019), p. 012075. DOI: 10.1088/1742-6596/1181/1/012075.

[5] A. S. Leszczyńska. "Potential of the IceTop Enhancement with a Scintillation Detector Array". PhD thesis. Karlsruhe Institute of Technology (KIT), 2020.

[6] E. Fermi. "On the Origin of the Cosmic Radiation". In: *Phys. Rev.* 75 (8 Apr. 1949), pp. 1169–1174. DOI: 10.1103/PhysRev.75.1169. URL: https://link.aps.org/doi/10.1103/PhysRev.75.1169.

[7] A.R. Bell. "Cosmic ray acceleration". In: *Astroparticle Physics* 43 (2013). Seeing the High-Energy Universe with the Cherenkov Telescope Array - The Science Explored with the CTA, pp. 56–70. ISSN: 0927-6505. DOI: https://doi.org/10.1016/j.astropartphys.2012.05.022. URL: https://www.sciencedirect.com/science/article/pii/S0927650512001272.

[8] M. Bustamante et al. "High-energy cosmic-ray acceleration". In: (2010). DOI: 10.5170/CERN-2010-001.533.

[9] F. G. Schroeder. *News from Cosmic Ray Air Showers (ICRC 2019 – Cosmic Ray Indirect Rapport)*. 2019. arXiv: 1910.03721 [astro-ph.HE].

[10] S. Klepser. "Reconstruction of Extensive Air Showers and Measurement of the Cosmic Ray Energy Spectrum in the Range of 1–80PeV at the South Pole". PhD thesis. Humboldt-Universität zu Berlin, 2008.

[11] C. Ge et al. "Revealing a peculiar supernova remnant G106.3+2.7 as a petaelectronvolt proton accelerator with X-ray observations". In: *The Innovation* 2.2 (2021), p. 100118. ISSN: 2666-6758. DOI: https://doi.org/10.1016/j.xinn.2021.100118. URL: https://www.sciencedirect.com/science/article/pii/S2666675821000436.

[12] POLAR-2 Collaboration. N. De Angelis. "Development and science perspectives of the POLAR-2 instrument: a large scale GRB polarimeter". In: *PoS* ICRC2021 (2021), p. 580. DOI: 10.22323/1.395.0580.

[13] M. Bustamante et al. "Neutrino and cosmic-ray emission from multiple internal shocks in gamma-ray bursts". In: *Nature Communications* 6 (2015), p. 6783. DOI: 10.1038/ncomms7783.

[14] S. D. Wick, C. D. Dermer, and Armen Atoyan. "High-energy cosmic rays from gamma-ray bursts". In: *Astropart. Phys.* 21 (2004), pp. 125–148. DOI: 10.1016/j.astropartphys.2003.12.008. arXiv: astro-ph/0310667.

[15] B.A. Nizamov and M. S. Pshirkov. "Constraints on the AGN flares as sources of ultra-high energy cosmic rays from the Fermi-LAT observations". In: *Journal of Cosmology and Astroparticle Physics* 2020.03 (Mar. 2020), pp. 060–060. ISSN: 1475-7516. DOI: 10.1088/1475-7516/2020/03/060. URL: http://dx.doi.org/10.1088/1475-7516/2020/03/060.

[16] M. Brüggemann. "Determination of an arrival time cut for the separation of electrons and muons in extensive air showers". PhD thesis. Universität Siegen, 2006.

[17] D. Perkins. *Particle Astrophysics*. Second. Oxford University Press, 2009. ISBN: 978-0-19-954546-9.

[18] E. Orlando. "Gamma rays from interactions of cosmic-ray electrons". PhD thesis. Technical University of Munich, 2008.

[19] S. Y. Lee. *Accelerator Physics*. Ed. by S. Y. Lee. Second. World Scientific, 2004. ISBN: 978-981-256-200-5. DOI: 10.1142/5761.

[20] V. Verzi, D. Ivanov, and Y. Tsunesada. "Measurement of energy spectrum of ultra-high energy cosmic rays". In: *Progress of Theoretical and Experimental Physics* 2017.12 (Nov. 2017). 12A103. ISSN: 2050-3911. DOI: 10.1093/ptep/ptx082. eprint: https://academic.oup.com/ptep/article-pdf/2017/12/12A103/22075708/ptx082.pdf.

[21] H. Dembinski et al. *Data-driven model of the cosmic-ray flux and mass composition from 10 GeV to* 10^{11} *GeV*. 2017. arXiv: 1711.11432 [astro-ph.HE].

[22] V. Verzi. "Cosmic Rays: air showers from low to high energies- Rapporteur Report of the 34th International Cosmic Ray Conference (The Hague, The Netherlands)". In: *PoS* (2015).

[23] M. Tanabashi. et al. (Particle Data Group), Phys. Rev. D98, 030001 (2018). DOI: 10.1103/PhysRevD.98.030001.

[24] P.A. Zyla. et al. (Particle Data Group), Prog. Theor. Exp. Phys. 2020, 083C01 (2020). DOI: 10.1093/ptep/ptaa104.

[25] Pierre Auger Collaboration. A. Coleman. "Measurement of the cosmic ray flux near the second knee with the Pierre Auger Observatory". In: *PoS* ICRC2019 (2019), p. 225. DOI: 10.22323/1.358.0225.

[26] Pierre Auger Collaboration. A. Aab et al. "Measurement of the cosmic-ray energy spectrum above $2.5 \cdot 10^{18}$ eV using the PierreAuger Observatory". In: *Phys. Rev. D.* 102.6 (2020), p. 062005. DOI: 10.1103/PhysRevD.102.062005.

[27] Pierre Auger Collaboration. A. Aab et al. "Features of the Energy Spectrum of Cosmic Rays above 2.5×10^{18} eV Using the Pierre Auger Observatory". In: *Phys. Rev. Lett.* 125 (12 Sept. 2020), p. 121106. DOI: 10.1103/PhysRevLett.125.121106. URL: https://link.aps.org/doi/10.1103/PhysRevLett.125.121106.

[28] J. R. Hörandel. "Models of the knee in the energy spectrum of cosmic rays". In: *Astroparticle Physics* 21.3 (2004), pp. 241–265. ISSN: 0927-6505. DOI: https://doi.org/10.1016/j.astropartphys.2004.01.004.

[29] J. Candia and E. Roulet. "Rigidity dependent knee and cosmic ray induced high energy neutrino fluxes". In: *JCAP* 09 (2003), p. 005. DOI: 10.1088/1475-7516/2003/09/005. arXiv: astro-ph/0306632.

[30] B. Peters. "Primary cosmic radiation and extensive air showers". In: *Nuovo Cim* 22 (1961), pp. 800–819. URL: https://doi.org/10.1007/BF02783106.

[31] KASCADE Collaboration. T. Antoni et al. "KASCADE measurements of energy spectra for elemental groups of cosmic rays: Results and open problems". In: *Astropart. Phys.* 24.1 (2005), pp. 1–25. ISSN: 0927-6505. DOI: https://doi.org/10.1016/j.astropartphys.2005.04.001.

[32] A. Haungs. "Cosmic Rays from the Knee to the Ankle". In: *Physics Procedia* 61 (2015). 13th International Conference on Topics in Astroparticle and Underground Physics, TAUP 2013, pp. 425–434. ISSN: 1875-3892. DOI: https://doi.org/10.1016/j.phpro.2014.12.094.

[33] A. M. Hillas. "Can diffusive shock acceleration in supernova remnants account for high-energy galactic cosmic rays?" In: *Nuclear Particle Physics* 31.5 (2005).

[34] T. Gaisser, T. Stanev, and S. Tilav. "Cosmic ray energy spectrum from measurements of air showers". In: *Frontiers of Physics* 8.6 (2013), pp. 748–758. DOI: 10.1007/s11467-013-0319-7.

[35] M. S. Muzio, M. Unger, and Farrar G R. "Constraints on UHECR sources and their environments, from fitting UHECR spectrum and composition, and neutrinos and gammas." In: *PoS* ICRC2019 (2019), p. 364. DOI: 10.22323/1.358.0364.

[36] D. Biehl et al. "Gamma-Ray Bursts as Sources of Ultra-High Energy Cosmic Rays across the Ankle". In: *PoS* ICRC2019 (2019), p. 196. DOI: 10.22323/1.358.0196.

[37] S. Mollerach and E. Roulet. "Ultrahigh energy cosmic rays from a nearby extragalactic source in the diffusive regime". In: *Phys. Rev. D* 99 (10 May 2019), p. 103010. DOI: 10.1103/PhysRevD.99.103010. URL: https://link.aps.org/doi/10.1103/PhysRevD.99.103010.

[38] S. Mollerach and E. Roulet. "Extragalactic cosmic rays diffusing from two populations of sources". In: *Phys. Rev. D* 101 (10 May 2020), p. 103024. DOI: 10.1103/PhysRevD.101.103024. URL: https://link.aps.org/doi/10.1103/PhysRevD.101.103024.

[39] E. Parizot. "GZK horizon and magnetic fields". In: *Nucl. Phys. B Proc. Suppl.* 136 (2004). Ed. by C. Aramo, A. Insolia, and C. Tuve, pp. 169–178. DOI: 10.1016/j.nuclphysbps.2004.10.034. arXiv: astro-ph/0409191.

[40] A. Aab et al. "Evidence for a mixed mass composition at the 'ankle' in the cosmic-ray spectrum". In: *Physics Letters B* 762 (2016), pp. 288–295. ISSN: 0370-2693. DOI: https://doi.org/10.1016/j.physletb.2016.09.039. URL: https://www.sciencedirect.com/science/article/pii/S0370269316305433.

[41] M. Unger, G. R. Farrar, and Luis A. Anchordoqui. "Origin of the ankle in the ultrahigh energy cosmic ray spectrum, and of the extragalactic protons below it". In: *Physical Review D* 92.12 (Dec. 2015). ISSN: 1550-2368. DOI: 10.1103/physrevd.92.123001. URL: http://dx.doi.org/10.1103/PhysRevD.92.123001.

[42] M. Kachelrieß. "Transition from Galactic to Extragalactic Cosmic Rays". In: *EPJ Web Conf.* 210 (2019), p. 04003. DOI: 10.1051/epjconf/201921004003. URL: https://doi.org/10.1051/epjconf/201921004003.

[43] Pierre Auger Collaboration. P. Abreu et al. "Combined fit of the energy spectrum and mass composition across the ankle with the data measured at the Pierre Auger Observatory". In: *PoS* ICRC2021 (2021), p. 311. DOI: 10.22323/1.395.0311.

[44] G. Giacinti et al. "Cosmic ray anisotropy as signature for the transition from galactic to extragalactic cosmic rays". In: *Journal of Cosmology and Astroparticle Physics* 2012.07 (July 2012), pp. 031–031. DOI: 10.1088/1475-7516/2012/07/031.

[45] A. Bobrikova et al. "Predicting the UHE photon flux from GZK-interactions of hadronic cosmic rays using CRPropa 3". In: *PoS* ICRC2021 (2021), p. 449. DOI: 10.22323/1.395.0449.

[46] K. Greisen. "End to the Cosmic-Ray Spectrum?" In: *Phys. Rev.* 16 (1966), pp. 748–750.

[47] G. T. Zatsepin and V. A. Kuz'min. "Upper Limit of the Spectrum of Cosmic Rays". In: *J. Exp. Theor. Phys. Lett.* 4 (1966), p. 78.

[48] A. M. Taylor. "The Propagation of Ultra High Energy Cosmic Rays". PhD thesis. Linacre College, 2006.

[49] A. Bridgeman. "Determining the Mass Composition of Ultra-high Energy Cosmic Rays Using Air Shower Universality". PhD thesis. Karlsruhe Institute of Technology (KIT), 2018.

[50] Pierre Auger Collaboration. J. Abraham et al. "Measurement of the energy spectrum of cosmic rays above 1018 eV using the Pierre Auger Observatory". In: *Phys. Lett. B* 685.4 (2010), pp. 239–246. ISSN: 0370-2693. DOI: https://doi.org/10.1016/j.physletb.2010.02.013.

[51] J. Albrecht et al. *The Muon Puzzle in cosmic-ray induced air showers and its connection to the Large Hadron Collider*. 2021. arXiv: 2105.06148 [astro-ph.HE].

[52] IceCube, KASCADE-Grande, NEVOD-DECOR, PierreAuger, SUGAR, Telescope Array and Yakutsk EAS Array Collaborations. H. P. Dembinski et al. "Report on Tests and Measurements of Hadronic Interaction Properties with Air Showers". In: *EPJ Web Conf.* 210 (2019), p. 02004. DOI: 10.1051/epjconf/201921002004. URL: https://doi.org/10.1051/epjconf/201921002004.

[53] H. Menjo, O. Adriani, and E. Berti. "The results and future prospects of the LHCf experiment". In: *PoS* ICRC2019 (2020), p. 349. DOI: 10.22323/1.358.0349.

[54] HAWC Collaboration and IceCube Collaboration. A. U. Abeysekara et al. "All-sky Measurement of the Anisotropy of Cosmic Rays at 10 TeV and Mapping of the Local Interstellar Magnetic Field". In: *The Astrophysical Journal* 871.1 (Jan. 2019), p. 96. ISSN: 1538-4357. DOI: 10.3847/1538-4357/aaf5cc.

[55] F. G. Schroeder et al. *High-Energy Galactic Cosmic Rays (Astro2020 Science White Paper)*. 2019. arXiv: 1903.07713 [astro-ph.HE].

[56] Pierre Auger Collaboration. Abreu P. et al. "Constraints on the origin of cosmic rays above 10^{18} eV from large-scale anisotropy searches in data of the Pierre Auger Observatory". In: *The Astrophysical Journal* 762.1 (Dec. 2012), p. L13. ISSN: 2041-8213. DOI: 10.1088/2041-8205/762/1/l13. URL: http://dx.doi.org/10.1088/2041-8205/762/1/L13.

[57] Pierre Auger Collaboration. E. Roulet. "Large-scale anisotropies above 0.03 EeV measured by the Pierre Auger Observatory". In: *PoS* ICRC2019 (2019), p. 408. DOI: 10.22323/1.358.0408.

[58] LHAASO Collaboration. Z. Cao, F.A. Aharonian, and Q. An. "Ultrahigh-energy photons up to 1.4 petaelectronvolts from 12 -ray Galactic sources". In: *Nature* 594 (2021), pp. 33–36. DOI: 10.1038/s41586-021-03498-z.

[59] G. Schatz. "Understanding the atmosphere as a calorimeter for UHE cosmic rays". In: *eConf* C040802 (2004). Ed. by Joanne Hewett et al., p. L022.

[60] A. F. Nelles. "Radio emission of air showers - The perspective of LOFAR and AERA". PhD thesis. Radboud University Nijmegen, 2014.

[61] P. K. F. Grieder. *Extensive Air Showers*. Vol. 1. Springer-Verlag Berlin Heidelberg, 2010. ISBN: 978-3-540-76940-8. DOI: 10.1007/978-3-540-76941-5.

[62] T. Stanev. "Cosmic Rays and Extensive Air Showers". In: *Elastic and Diffractive Scattering*. Ed. by Mario Deile, David d'Enterria, and Albert De Roeck. 2010.

[63] J. Ridky et al. "Prompt muons in extended air showers". In: *30th International Cosmic Ray Conference*. June 2007. arXiv: 0706.2145 [astro-ph].

[64] F. G. Schroeder. "Radio detection of cosmic-ray air showers and high-energy neutrinos". In: *Progress in Particle and Nuclear Physics* 93 (2017), pp. 1–68. ISSN: 0146-6410. DOI: https://doi.org/10.1016/j.ppnp.2016.12.002.

[65] A. A. Lagutin, R. I. Raikin, and T. L. Serebryakova. "Air shower universality from 1014to 1022eV". In: *Journal of Physics: Conference Series* 409 (Feb. 2013), p. 012092. ISSN: 1742-6596. DOI: 10.1088/1742-6596/409/1/012092.

[66] J. Matthews. "A Heitler model of extensive air showers". In: *Astropart. Phys.* 22 (2005), pp. 387–397. DOI: 10.1016/j.astropartphys.2004.09.003.

[67] B.. Keilhauer et al. "Nitrogen fluorescence in air for observing extensive air showers". In: *EPJ Web of Conferences* 53 (2013). Ed. by K.-H. Kampert et al., p. 01010. ISSN: 2100-014X. DOI: 10.1051/epjconf/20135301010.

[68] F. Arqueros, J. R. Hörandel, and B. Keilhauer. "Air fluorescence relevant for cosmic-ray detection—Summary of the 5th fluorescence workshop, El Escorial 2007". In: *Nuclear Instruments and Methods in Physics Research Section A: Accelerators, Spectrometers, Detectors and Associated Equipment* 597.1 (2008). Proceedings of the 5th Fluorescence Workshop, pp. 1–22. ISSN: 0168-9002. DOI: https://doi.org/10.1016/j.nima.2008.08.056.

[69] V.V. Prosin et al. "Tunka-133: Results of 3 year operation". In: *Nuclear Instruments and Methods in Physics Research Section A: Accelerators, Spectrometers, Detectors and Associated Equipment* 756 (2014), pp. 94–101. ISSN: 0168-9002. DOI: https://doi.org/10.1016/j.nima.2013.09.018.

[70] O. Scholten, K. Werner, and F. Rusydi. "A macroscopic description of coherent geomagnetic radiation from cosmic-ray air showers". In: *Astroparticle Physics* 29.2 (2008), pp. 94–103. ISSN: 0927-6505. DOI: https://doi.org/10.1016/j.astropartphys.2007.11.012.

[71] Pierre Auger Collaboration. S. de Jong. "Detection of High Energy Cosmic Rays at the Auger Engineering Radio Array". In: Feb. 2017, p. 080. DOI: 10.22323/1.282.0080.

[72] P. Schellart et al. "Polarized radio emission from extensive air showers measured with LOFAR". In: *Journal of Cosmology and Astroparticle Physics* 2014.10 (Oct. 2014), pp. 014–014. ISSN: 1475-7516. DOI: 10.1088/1475-7516/2014/10/014.

[73] Telescope Array Collaboration. R. Abbasi et al. "Depth of Ultra High Energy Cosmic Ray Induced Air Shower Maxima Measured by the Telescope Array Black Rock and Long Ridge FADC Fluorescence Detectors and Surface Array in Hybrid Mode". In: *The Astrophysical Journal* 858.2 (May 2018), p. 76. ISSN: 1538-4357. DOI: 10.3847/1538-4357/aabad7. URL: http://dx.doi.org/10.3847/1538-4357/aabad7.

[74] Telescope Array Collaboration. R. Abbasi et al. "The Cosmic-Ray Composition between 2 PeV and 2 EeV Observed with the TALE Detector in Monocular Mode". In: *The Astrophysical Journal* 909.2 (Mar. 2021), p. 178. DOI: 10.3847/1538-4357/abdd30.

[75] V. A. Balagopal et al. "Search for PeVatrons at the Galactic Center using a radio air-shower array at the South Pole". In: *The European Physical Journal C* 78 (2018), p. 111. DOI: 10.1140/epjc/s10052-018-5537-2.

[76] J. Garbe et al. "The hysteresis of the Antarctic Ice Sheet". In: *Nature* 585 (2020), pp. 538–544. DOI: 10.1038/s41586-020-2727-5.

[77] P. Fretwell et al. "Bedmap2: improved ice bed, surface and thickness datasets for Antarctica". In: *The Cryosphere* 7.1 (2013), pp. 375–393. DOI: 10.5194/tc-7-375-2013. URL: https://tc.copernicus.org/articles/7/375/2013/.

[78] IceCube Collaboration. M. G. Aartsen et al. "Measurement of South Pole ice transparency with the IceCube LED calibration system". In: *Nuclear Instruments and Methods in Physics Research Section A: Accelerators, Spectrometers, Detectors and Associated Equipment* 711 (2013), pp. 73–89. ISSN: 0168-9002. DOI: https://doi.org/10.1016/j.nima.2013.01.054.

[79] IceCube-Gen2 Collaboration. M. G. Aartsen et al. *IceCube-Gen2: A Vision for the Future of Neutrino Astronomy in Antarctica*. 2014. arXiv: 1412.5106 [astro-ph.HE].

[80] IceCube Collaboration. J. Ahrens et al. *IceCube Preliminary Design Document*. 2001.

[81] Particle Data Group. J. Beringer et al. "Review of Particle Physics". In: *Phys. Rev. D* 86 (1 July 2012), p. 010001. DOI: 10.1103/PhysRevD.86.010001.

[82] IceCube Collaboration. M. G. Aartsen et al. "Energy reconstruction methods in the IceCube neutrino telescope". In: *Journal of Instrumentation* 9.03 (Mar. 2014), P03009–P03009. DOI: 10.1088/1748-0221/9/03/p03009.

[83] M. Ackermann et al. "Search for neutrino-induced cascades with AMANDA". In: *Astroparticle Physics* 22.2 (Nov. 2004), pp. 127–138. ISSN: 0927-6505. DOI: 10.1016/j.astropartphys.2004.06.003.

[84] AMANDA Collaboration. J. Ahrens et al. "Search for neutrino-induced cascades with the AMANDA detector". In: *Phys. Rev. D* 67 (1 Jan. 2003), p. 012003. DOI: 10.1103/PhysRevD.67.012003.

[85] E. Middell. "Search for neutrino-induced particle showers with IceCube-40". PhD thesis. Humboldt-Universität zu Berlin, 2015.

[86] IceCube Collaboration. T. Gaisser. "Seasonal variation of atmospheric neutrinos in IceCube". In: *33rd International Cosmic Ray Conference*. 2013.

[87] IceCube-Gen2 Collaboration. D. J. Koskinen. "Atmospheric neutrino results from IceCube-DeepCore and plans for PINGU". In: *Journal of Physics: Conference Series* 888 (Sept. 2017), p. 012023. DOI: 10.1088/1742-6596/888/1/012023.

[88] IceCube Collaboration. T. Waldenmaier. "IceTop — Cosmic ray physics with IceCube". In: *Nuclear Instruments and Methods in Physics Research Section A: Accelerators, Spectrometers, Detectors and Associated Equipment* 588.1-2 (Apr. 2008), pp. 130–134. ISSN: 0168-9002. DOI: 10.1016/j.nima.2008.01.015.

[89] IceCube Collaboration. T. Stanev. "Status, performance, and first results of the IceTop array". In: *Nucl. Phys. B Proc. Suppl.* 196 (2009). Ed. by Jean-Noël Capdevielle, Ralph Engel, and Bryan Pattison, pp. 159–164. DOI: 10.1016/j.nuclphysbps.2009.09.028. arXiv: 0903.0576 [astro-ph.HE].

[90] IceCube Collaboration. R. Abbasi et al. "IceTop: The surface component of IceCube". In: *Nuclear Instruments and Methods in Physics Research Section A: Accelerators, Spectrometers, Detectors and Associated Equipment* 700 (2013), pp. 188–220. ISSN: 0168-9002. DOI: https://doi.org/10.1016/j.nima.2012.10.067.

[91] IceCube Collaboration. J. Gonzalez. *Measuring the Muon Content of Air Showers with IceTop*. 2015. arXiv: 1501.03415 [astro-ph.HE].

[92] K. Rawlins. "A Function to Describe Attenuation of Cosmic Ray Air Shower Particles in Snow". In: *PoS* ICRC2015 (2016), p. 628. DOI: 10.22323/1.236.0628.

[93] IceCube Collaboration. M. Kauer et al. "The Scintillator Upgrade of IceTop: Performance of the Prototype Array". In: *Proceedings of 36th International Cosmic Ray Conference — PoS(ICRC2019)*. Vol. 358. 2019, p. 309. DOI: 10.22323/1.358.0309.

[94] IceCube Collaboration. A. Leszczyńska and M. Plum. *Simulation and Reconstruction Study of a Future Surface Scintillator Array at the IceCube Neutrino Observatory*. 2019. arXiv: 1909.02258 [astro-ph.IM].

[95] IceCube Collaboration. A. Haungs. "A Scintillator and Radio Enhancement of the IceCube Surface Detector Array". In: *EPJ Web of Conferences* 210 (2019). Ed. by I. Lhenry-Yvon et al., p. 06009. ISSN: 2100-014X. DOI: 10.1051/epjconf/201921006009.

[96] IceCube-Gen2 Collaboration. F. G. Schroeder. "Physics Potential of a Radio Surface Array at the South Pole". In: *EPJ Web of Conferences* 216 (2019). Ed. by G. Riccobene et al., p. 01007. ISSN: 2100-014X. DOI: 10.1051/epjconf/201921601007.

[97] IceCube Collaboration. R. Abbasi et al. "First air-shower measurements with the prototype station of the IceCube surface enhancement". In: *PoS* ICRC2021 (2021), p. 314. DOI: 10.22323/1.395.0314.

[98] M. Renschler. "A Prototype Radio Detector for the IceCube Surface Enhancement". 51.03.04; LK 01. PhD thesis. Karlsruher Institut für Technologie (KIT), 2020. 169 pp. DOI: 10.5445/IR/1000104529.

[99] M. Oehler et al. *Characterization of SiPMs for coemic-ray air-shower detectors for the IceCube upgrade*. Vortrag gehalten auf DPG Frühjahrstagung der Sektion Materie und Kosmos, Würzburg, 19. - 23.03.2018. 51.03.04; LK 01. 2018.

[100] IceCube Collaboration. K. Samridha et al. "The IceTop Scintillator Upgrade". In: *PoS* ICRC2017 (2018), p. 401. DOI: 10.22323/1.301.0401.

[101] T. Karg et al. *Introducing TAXI: a Transportable Array for eXtremely large area Instrumentation studies*. 2014. arXiv: 1410.4685 [astro-ph.IM].

[102] P. P. M. Jansweijer, H. Z. Peek, and E. De Wolf. "White Rabbit: Sub-nanosecond timing over Ethernet". In: *Nucl. Instrum. Meth. A* 725 (2013). Ed. by G. Anton et al., pp. 187–190. DOI: 10.1016/j.nima.2012.12.096.

[103] IceCube-Gen2 Collaboration. M. G. Aartsen, R. Abbasi, and M. Ackermann. *IceCube-Gen2: The Window to the Extreme Universe*. 2020. arXiv: 2008.04323 [astro-ph.HE].

[104] IceCube-Gen2 Collaboration. M. G. Aartsen et al. *Neutrino astronomy with the next generation IceCube Neutrino Observatory*. 2019. arXiv: 1911.02561 [astro-ph.HE].

[105] IceCube Collaboration. S. Baur. "Dark matter searches with the IceCube Upgrade". In: *PoS* ICRC2019 (2020), p. 506. DOI: 10.22323/1.358.0506. arXiv: 1908.08236 [astro-ph.HE].

[106] IceCube Collaboration. W. Y. Ma. "Physics Potential of the IceCube Upgrade". In: *J. Phys.: Conf. Ser.* 1468 012169 (2020). URL: https://doi.org/10.1088/1742-6596/1468/1/012169.

[107] S. Mondal. *Physics of Neutrino Oscillation*. 2015. arXiv: 1511.06752 [physics.gen-ph].

[108] IceCube Collaboration. T. Stuttard. "Neutrino oscillations and PMNS unitarity with IceCube/DeepCore and the IceCube Upgrade". In: *PoS* NuFact2019 (2020), p. 099. DOI: 10.22323/1.369.0099.

[109] Y.-F. Li. "Overview of the Jiangmen Underground Neutrino Observatory (JUNO)". In: *International Journal of Modern Physics: Conference Series* 31 (2014), p. 1460300. DOI: 10.1142/S2010194514603007. eprint: https://doi.org/10.1142/S2010194514603007.

[110] JUNO Collaboration. F. An et al. "Neutrino physics with JUNO". In: *Journal of Physics G: Nuclear and Particle Physics* 43.3 (Feb. 2016), p. 030401. DOI: 10.1088/0954-3899/43/3/030401.

[111] IceCube Collaboration. D. Heinen et al. "An Acoustic Calibration System for the IceCube Upgrade". In: (July 2019). DOI: https://doi.org/10.22323/1.358.1030. arXiv: 1909.02047 [astro-ph.IM].

[112] C. Tönnis IceCube Collaboration. W. Kang and C. Rott. "The camera system for the IceCube Upgrade". In: (July 2019). DOI: https://doi.org/10.22323/1.358.0928.

[113] IceCube Collaboration. D. Chirkin. "Evidence of optical anisotropy of the South Pole ice". In: *33rd International Cosmic Ray Conference*. 2013.

[114] IceCube-Gen2 Collaboration. R. Abbasi et al. "Sensitivity studies for the IceCube-Gen2 radio array". In: *PoS* ICRC2021 (2021), p. 1183. DOI: 10.22323/1.395.1183.

[115] IceCube Collaboration. A. Achterberg et al. "First year performance of the IceCube neutrino telescope". In: *Astroparticle Physics* 26.3 (2006), pp. 155–173. ISSN: 0927-6505. DOI: https://doi.org/10.1016/j.astropartphys.2006.06.007.

[116] IceCube Collaboration. R. Abbasi et al. "Cosmic-Ray Studies with the Surface Instrumentation of IceCube". In: *Proceedings of 37th International Cosmic Ray Conference — PoS(ICRC2021)*. Vol. 395. 2021, p. 336. DOI: 10.22323/1.395.0336.

[117] E. de Lera Acedo et al. "Evolution of SKALA (SKALA-2), the log-periodic array antenna for the SKA-low instrument". In: *2015 International Conference on Electromagnetics in Advanced Applications (ICEAA)*. 2015, pp. 839–843. DOI: 10.1109/ICEAA.2015.7297231.

[118] IceCube Collaboration. R. Abbasi et al. "Development of a scintillation and radio hybrid detector array at the South Pole". In: *Proceedings of 37th International Cosmic Ray Conference — PoS(ICRC2021)*. Vol. 395. 2021, p. 225. DOI: 10.22323/1.395.0225.

[119] IceCube Collaboration. M G Aartsen et al. "All-sky Search for Time-integrated Neutrino Emission from Astrophysical Sources with 7 yr of IceCube Data". In: *The Astrophysical Journal* 835.2 (Jan. 2017), p. 151. DOI: 10.3847/1538-4357/835/2/151.

[120] D. Heck et al. *CORSIKA: A Monte Carlo code to simulate extensive air showers*. Tech. rep. 51.02.03; LK 01; Wissenschaftliche Berichte, FZKA-6019 (Februar 98). 1998. DOI: 10.5445/IR/270043064.

[121] P. Doll et al. "The Karlsruhe Cosmic Ray Project KASCADE". In: *Nucl. Phys. B (Proc.Suppl.)* 14A (Aug. 1990), p. 336.

[122] D. Heck and T. Pierog. *Extensive Air Shower Simulationwith CORSIKA:A User's Guide (Version 7.7410)*. Tech. rep. Karlsruhe Institute of Technology (KIT), Institute for Astroparticlephysics, 2021.

[123] T. T. Böhlen et al. "The FLUKA Code: Developments and Challenges for High Energy and Medical Applications". In: *Nucl. Data Sheets* 120 (2014), pp. 211–214. DOI: 10.1016/j.nds.2014.07.049.

[124] F. Riehn et al. "Hadronic interaction model sibyll 2.3d and extensive air showers". In: *Phys. Rev. D* 102 (6 Sept. 2020), p. 063002. DOI: 10.1103/PhysRevD.102.063002.

[125] Book For Application Developers - Release 10.4. *Geant4 - A Simulation Toolkit*. Geant4 Collaboration. 2017. URL: https://geant4-userdoc.web.cern.ch/UsersGuides/ForApplicationDeveloper/BackupVersions/V10.4/fo/BookForAppliDev.pdf.

[126] Physics Reference Manual - Release 10.4. *Geant4 - A Simulation Toolkit*. Geant4 Collaboration. 2017. URL: https://geant4-userdoc.web.cern.ch/UsersGuides/ForApplicationDeveloper/BackupVersions/V10.4/fo/BookForAppliDev.pdf.

[127] J. B. Birks. "Scintillations from Organic Crystals: Specific Fluorescence and Relative Response to Different Radiations". In: *Proceedings of the Physical Society. Section A* 64.10 (Oct. 1951), pp. 874–877. DOI: 10.1088/0370-1298/64/10/303.

[128] A. Leszczyńska. *Private Conversation*.

[129] M. Oehler. *Private Conversation*.

[130] D. Renker and E. Lorenz. "Advances in solid state photon detectors". In: *Journal of Instrumentation* 4.04 (Apr. 2009), P04004–P04004. DOI: 10.1088/1748-0221/4/04/p04004.

[131] Y. Nakamura et al. "Characterization of SiPM Optical Crosstalk and Its Dependence on the Protection-Window Thickness". In: *Proceedings of the 5th International Workshop on New Photon-Detectors (PD18)* (Nov. 2019). DOI: 10.7566/jpscp.27.011003.

[132] T. Niggemann et al. "G4SiPM: A novel silicon photomultiplier simulation package for Geant4". In: *Nuclear Instruments and Methods in Physics Research Section A: Accelerators, Spectrometers, Detectors and Associated Equipment* 787 (2015). New Developments in Photodetection NDIP14, pp. 344–347. ISSN: 0168-9002. DOI: https://doi.org/10.1016/j.nima.2015.01.067.

[133] M. Oehler. *PhD thesis at KIT in progress*. 2021.

[134] S. Wallis. "Binomial Confidence Intervals and Contingency Tests: Mathematical Fundamentals and the Evaluation of Alternative Methods". In: *Journal of Quantitative Linguistics* 20.3 (2013), pp. 178–208. DOI: 10.1080/09296174.2013.799918.

[135] E. B. Wilson. "Probable Inference, the Law of Succession, and Statistical Inference". In: *Journal of the American Statistical Association* 22.158 (1927), pp. 209–212. DOI: 10.1080/01621459.1927.10502953.

[136] R. Engel. *Indirect Detection of Cosmic Rays. In: Grupen C., Buvat I. (eds) Handbook of Particle Detection and Imaging*. Springer, Berlin, Heidelberg, 2012. DOI: 10.1007/978-3-642-13271-1_24.

[137] J. Nishimura and K. Kamata. "The Lateral and Angular Distribution of Cascade Showers". In: *Progress of Theoretical Physics* 5.5 (Sept. 1950), pp. 899–901. ISSN: 0033-068X. DOI: 10.1143/ptp/5.5.899. eprint: https://academic.oup.com/ptp/article-pdf/5/5/899/5234282/5-5-899.pdf.

[138] K. Greisen. "The Extensive Air Showers". In: *Prog. Cosmic-ray Physics.* 3 (1956), pp. 19–37.

[139] A. Ivanov, M. I. pravdin, and A. Saburov. "Modeling a relation between shower age and lateral distribution parameters of extensive air showers of cosmic rays". In: *International Journal of Modern Physics D* 20 (May 2012). DOI: 10.1142/S0218271811019463.

[140] J. Linsley, L. Scarsi, and B. Rossi. "ENERGY SPECTRUM AND STRUCTURE OF LARGE AIR SHOWERS". In: *J. Phys. Soc. Japan* 17, Suppl. A-III (Jan. 1962). URL: https://www.osti.gov/biblio/4763991.

[141] H. Abramowicz, A. Abusleme, and A. Zhemchugov. "Measurement of shower development and its Molière radius with a four-plane LumiCal test set-up". In: *The European Physical Journal C* 78 (2018), p. 135. DOI: 10.1140/epjc/s10052-018-5611-9.

[142] J.-N. Capdevielle and F. Cohen. "The relation between the lateral profile of giant extensive air showers and the age parameter". In: *Journal of Physics G: Nuclear and Particle Physics* 31.5 (Apr. 2005), pp. 507–524. DOI: 10.1088/0954-3899/31/5/018.

[143] Pierre Auger Collaboration. M. Ave et al. "The accuracy of signal measurement with the water Cherenkov detectors of the Pierre Auger Observatory". In: *Nuclear Instruments and Methods in Physics Research Section A: Accelerators, Spectrometers, Detectors and Associated Equipment* 578.1 (2007), pp. 180–184. ISSN: 0168-9002. DOI: https://doi.org/10.1016/j.nima.2007.05.150.

[144] Pierre Auger Collaboration. Y. Tokonatsu. "Signal fluctuations in the Auger Surface Detector". In: *28th International Cosmic Ray Conference*. Sept. 2003. arXiv: astro-ph/0309491.

[145] F. Kislat. "Study of charge and time fluctuations of signals in the IceTop detector". MA thesis. Humboldt-Universität zu Berlin, 2007.

[146] P.A. Bromiley. *Products and Convolutions of Gaussian Probability Density Functions*. 2013. URL: https://citeseerx.ist.psu.edu/viewdoc/download?doi=10.1.1.583.3007&rep=rep1&type=pdf.

[147] IceCube Collaboration. J. Gonzalez. "Studying Cosmic Ray Composition with IceTop using Muon and Electromagnetic Lateral Distributions". In: *PoS* ICRC2015 (2016), p. 338. DOI: 10.22323/1.236.0338.

[148] A. A. Kosinski. "Cramer's Rule Is Due To Cramer". In: *Mathematics Magazine* 74.4 (2001), pp. 310–312. DOI: 10.1080/0025570X.2001.11953081. eprint: https://doi.org/10.1080/0025570X.2001.11953081.

[149] F. James. *Function Minimization and Error Analysis*. 1998. URL: http://cdsweb.cern.ch/record/2296388/files/minuit.pdf.

[150] A. M. Hillas et al. "Measurement of primary energy of air showers in the presence of fluctuations". In: *12th International Conference on Cosmic Rays* 3 (1971), p. 1001.

[151] F. Kislat. "Measurement of the energy spectrum of cosmic rays with the 26 station configuration of the IceTop detector". PhD thesis. Humboldt-Universität zu Berlin, Mathematisch-Naturwissenschaftliche Fakultät I, 2012. DOI: http://dx.doi.org/10.18452/16443.

[152] D. Newton, J. Knapp, and A.A. Watson. "The optimum distance at which to determine the size of a giant air shower". In: *Astroparticle Physics* 26.6 (2007), pp. 414–419. ISSN: 0927-6505. DOI: https://doi.org/10.1016/j.astropartphys.2006.08.003.

[153] LHAASO Collaboration. L. L. Ma. "Measurement of cosmic rays with LHAASO-WFCTA from 10 PeV to 100 PeV". In: *33rd International Cosmic Ray Conference*. 2013.

[154] Z. Wang, Y. Guo, H. Cai, et al. "Performance of a scintillation detector array operated with LHAASO-KM2A electronics". In: *Experimental Astronomy* 45 (2018), pp. 363–377. DOI: 10.1007/s10686-018-9588-z.

[155] Pierre Auger Collaboration. I. C. Maris. "The AMIGA infill detector of the pierre auger observatory: Performance and first data". In: *Proceedings of the 32nd International Cosmic Ray Conference, ICRC 2011* 1 (Jan. 2011), pp. 267–270. DOI: 10.7529/ICRC2011/V01/0711.

[156] IceCube-Gen2 Collaboration. A. Coleman, A. Leszczyńska, and M. Weyrauch. "Simulation study for the future IceCube-Gen2 surface array". In: *PoS* ICRC2021 (2021), p. 411. DOI: 10.22323/1.395.0411. arXiv: 2108.04307 [astro-ph.HE].

[157] L. Cazon. "Working Group Report on the Combined Analysis of Muon Density Measurements from Eight Air Shower Experiments". In: *PoS* ICRC2019 (2019), p. 214. DOI: 10.22323/1.358.0214.

[158] A. Fedynitch et al. "Hadronic interaction model sibyll 2.3c and inclusive lepton fluxes". In: *Phys. Rev. D* 100 (10 Nov. 2019), p. 103018. DOI: 10.1103/PhysRevD.100.103018.

[159] IceCube Collaboration. M G Aartsenn et al. "Characterization of the atmospheric muon flux in IceCube". In: *Astroparticle Physics* 78 (2016), pp. 1–27. ISSN: 0927-6505. DOI: https://doi.org/10.1016/j.astropartphys.2016.01.006.

[160] E. M. Holt, F. G. Schroeder, and A. Haungs. "Enhancing the cosmic-ray mass sensitivity of air-shower arrays by combining radio and muon detectors". In: *The European Physical Journal C* 79 (2019), p. 371. DOI: 10.1140/epjc/s10052-019-6859-4.

[161] D. Maurel. "Masscomposition of ultra-high energy cosmic rays based on air shower universality". PhD thesis. Karlsruhe Institute of Technology (KIT), 2013.

[162] J.-H. Koehne et al. "PROPOSAL: A tool for propagation of charged leptons". In: *Computer Physics Communications* 184.9 (2013), pp. 2070–2090. ISSN: 0010-4655. DOI: https://doi.org/10.1016/j.cpc.2013.04.001.

[163] A. J. Izenman. *Linear Discriminant Analysis. In: Modern Multivariate Statistical Techniques*. Springer, New York, 2013. DOI: 10.1007/978-0-387-78189-1_8.

[164] S. Balakrishnama and A. Ganapathiraju. "Linear discriminant analysis-a brief tutorial". In: *Institute for Signal and information Processing* 18.1998 (1998), pp. 1–8.

[165] H. Pfau. *Bachelor thesis at KIT in progress*. 2021.

[166] IceCube Collaboration. R. Abbasi et al. "Study of mass composition of cosmic rays with IceTop and IceCube". In: *Proceedings of 37th International Cosmic Ray Conference — PoS(ICRC2021)*. Vol. 395. 2021, p. 323. DOI: 10.22323/1.395.0323.

[167] LHAASO Collaboration. G. Di Sciascio. "The LHAASO experiment: From Gamma-Ray Astronomy to Cosmic Rays". In: *Nuclear and Particle Physics Proceedings* 279-281 (2016). Proceedings of the 9th Cosmic Ray International Seminar, pp. 166–173. ISSN: 2405-6014. DOI: https://doi.org/10.1016/j.nuclphysbps.2016.10.024.

[168] IceCube Collaboration. J. Gonzalez. "Muon Measurements with IceTop". In: *EPJ Web Conf.* 208 (2019), p. 03003. DOI: 10.1051/epjconf/201920803003.

[169] IceCube Collaboration. M G Aartsen et al. “Cosmic ray spectrum and composition from PeV to EeV using 3 years of data from IceTop and IceCube”. In: *Phys. Rev. D* 100 (8 Oct. 2019), p. 082002. DOI: 10.1103/PhysRevD.100.082002.

Acknowledgements

Firstly, I would like to thank Prof. Frank Schröder for the possibility to write this thesis and for reviewing it. The many suggestions and discussions were crucial for improving this work. Further, I want to express my gratitude to Prof. Ralph Engel for acting as second reviewer and for the helpful suggestions.
The greatest thank goes to Dr. Agnieszka Leszczyńska for the excellent advise during this entire year, and the countless helpful discussions and suggestions. Thank you for guiding me in working with the simulation framework and for all your expertise. In particular, I want to thank you for the comprehensive proofreading, which was an invaluable help to improve this thesis, and for your support in the stressful times.
I want to thank Dr. Andreas Haungs for his kind character, the warm welcome and for providing me with many useful suggestions.
Further, I want to thank Dr. Alan Coleman for all the helpful input in various analysis topics. Thank you to Dr. Doris Wochele, for the help in cases of computing issues and for your kind character. Great thanks goes to Marie Oehler, for her warm character and for her expertise and helpful suggestions.
I want to express my gratitude towards all my colleagues from the IceCube group at Campus North, thank you for the warm working atmosphere. Further, my gratitude goes to the Cosmic-Ray Working Group, the IceCube-Gen2 Surface Working Group as well as the IceCube- and IceCube-Gen2 Collaborations for the many fruitful discussions.
A special thanks goes to my fellow students Alexander Böhmländer, Eugen Raspopin and Tobias Schulz, for all the support and the discussions during the studies. Thank you Alexander, for all your help regarding LaTeX.
The warmest thanks goes to my family. Thank you so much for all the support and the encouragement, without which this work would not have been possibly. Thank you for always providing me with strength during difficult times.